Spring 5-14-2022

Characterization of Sea level Changes along the Louisiana/Florida Shelf Using High Frequency (HF) Radar Data and Sea level Measurements

uchenna nwankwo
University of Southern Mississippi

Recommended Citation

nwankwo, uchenna, "Characterization of Sea level Changes along the Louisiana/Florida Shelf Using High Frequency (HF) Radar Data and Sea level Measurements" (2022). *Dissertations*. 1987.
https://aquila.usm.edu/dissertations/1987

CHARACTERIZATION OF SEA LEVEL CHANGES ALONG THE LOUISIANA/FLORIDA SHELF USING HIGH FREQUENCY (HF) RADAR DATA AND SEA LEVEL MEASUREMENTS

by

Uchenna Chizaram Nwankwo

A Dissertation
Submitted to the Graduate School,
the College of Arts and Sciences
and the School of Ocean Science and Engineering
at The University of Southern Mississippi
in Partial Fulfillment of the Requirements
for the Degree of Doctor of Philosophy

Approved by:

Dr. Stephan D. Howden, Committee Chair
Dr. Dmitri A. Netchaev
Dr. Brian Dzwonkowski
Dr. David E. Wells
Dr. Gero Nootz

May 2022

Published by the Graduate School

THE UNIVERSITY OF
SOUTHERN
MISSISSIPPI®

ABSTRACT

In this dissertation, three sea level studies in the Mississippi Bight (MSB) have been conducted. The first is an investigation into why VDatum, the vertical datum transformation tool of NOAA, has large errors in the western side of the MSB. The second is an estimation of the subinertial (>2 day timescale) shape of sea level over the high frequency radar (HFR) coverage in the MSB and to what extent it is in geostrophic balance. The third study examines the relative contribution of different mechanims to the subinertial sea level in the HFR coverage area. For the first study, NOAA hypothesized that the errors were due to subsidence, but it was found that errors in range (~0.23 m) and in absolute tidal datums levels (0.15 to -0.41 m) were present and it was shown that imperfections in the tidal models and Topography of the Sea Surface could be responsible in these errors, respectively. The second study was aimed to provide mapped sea level estimates over the MSB, other than the gridded sea level estimates derived from coarse resolution satellite altimetry data. In the study, it was determined that the subinertial sea surface topography was predominately in geostrophic balance as Coriolis force was dominant in momentum balance except for few instances (0.01%) when Rossby number >0.1. The resulting subinertial sea level anomalies were validated using sea level observations from an offshore buoy and Setinel-3 along-track satellite altimeter data. The estimated root mean square difference of <0.04 m indicated a good agreement of the reconstructed sea level anomalies with independent observations. Analysis of the empirical orthogonal function showed that the first two modes explained majority of the variance in the sea level anomalies. In the third study, three mechanisms (wind-stress, Loop Current (LC) influence and freshwater discharge) were investigated to understand their contribution to the estimated patterns in the sea level gradient. Wind-stress was found to have the most influence in the patterns of the sea level gradient. While there was no indication of significant influence from freshwater discharge, it was revealed that the LC remotely influenced the patterns in sea level changes.

ACKNOWLEDGMENTS

The success of my doctoral program was possible because Dr. Stephan Howden showed an unwavering trust in me by accepting to supervise me despite my academic background. He gave me a stupendous guidance over the course of my program. I have an unreserved appreciation for Dr. Dmitri Netchaev. Dr. Netchaev and myself had countless meetings where we discussed concepts which were ambiguous to me. He always had ways of dissecting the ambiguous concepts to make them clear. His patience is top notch. I appreciate the contributions of my other committee members: Dr. Brian Dzwonkowski, Dr. David Wells and Dr. Gero Nootz. The inputs of the entire committee made me a better scientist.

I wish to greatly appreciate the invaluable sacrifices Ngozi made in the course of my program. She was extremely supportive and she exercised a boundless patience. Her love and care kept me motivated as I strived to make her proud. I also wish to thank my parents and siblings for their amazing support.

I appreciate the hard work of the CenGOOS group at USM towards keeping the HFR stations operational and their diligence in making the data available. I thank the services of Mike Runner and Scott Perrin of USGS for providing the various information about the coastal USGS gauges and the permit to perform GPS surveys at the gauges. Furthermore, I appreciate the contributions of Dr. Asper Vernon. His inquiries and feedback unraveled some ideas, which improved my research. A special acknowledgment is due to the former Director of the USM Hydrographic Science Research Center, the late RDML (ret.) Ken Barbor whose leadership made this work possible. I got fantastic support from numerous friends and colleagues and honorable mentions includes: Dr.

Laura Hode, Dr. Stephan O’Brien, Abednego Nkem, Dr. Michael Ezebuenyi and Dr. Ikechukwu Maduako. Furthermore, I thank Dr. Dan Codiga and Dr. Laurent Roblou who despite not knowing me, they assisted me when I reached out. I also wish to appreciate the Marine Technology Society and Society for Underwater Technology in the U.S. for the scholarships they awarded me.

This research was supported by funds from several sources. Funding NOAA10.13039/100000192USM was from Mapping Center of the USM Hydrographic Science Research Center NOAA’s Office of Ocean and Atmospheric Research and U.S. Department of Commerce.10.13039/100000192. It was provided by NOAA through a grant to the USM Mapping Center of the USM Hydrographic Science Research Center. This work was also supported by NOAA’s Office of Ocean and Atmospheric Research and U.S. Department of Commerce. Additional funding for this project was through award NA18NOS0120018 to the Gulf of Mexico Coastal Ocean Observing System from the Integrated Ocean Observing System Office of the National Oceanic and Atmospheric Administration.

DEDICATION

This work is dedicated to my family.

TABLE OF CONTENTS

LIST OF TABLES

LIST OF ILLUSTRATIONS

LIST OF ABBREVIATIONS

ADCIRC	ADvanced CIRCulation
ADCP	Acoustic Doppler Current Profiler
APR	Antenna Reference Point
AVHRR	Advanced Very High Resolution Radiometer
CenGOOS	Central Gulf of Mexico Ocean Observing System
COAWST	Coupled Ocean-Atmospher-Waves-Sediment Transport
DTL	Diurnal Tide Level
EOF	Empirical Orthogonal Function
ERS	Ellipsoidally Referenced Survey
FFT	Fast Fourier Transform
Fig	Figure
GCOOS	Gulf of Mexico Coastal Ocean Observing System
GDOP	Geometric Dilution of Precision
GDR	Geophysical Data Records
GNSS	Global Navigation Satellite System
GPS	Global Positioning System
Gt	Great diurnal range
HF	High Frequency

J2	Jason-2
LC	Loop Current
LCE	Loop Current Eddy
LMSL	Local Mean Sea Level
MCC	Maximum Cross Correlation
MHz	Mega Hertz
MHHW	Mean Higher High Water
MLLW	Mean Lower Low Water
MRRM	Modified-Range Ratio Method
MSL	Mean Sea Level
NAD83	North American Datum 1983
NAVD88	North America Vertical Datum 1988
NAVO	Naval Oceanographic Office
NDBC	National Data Buoy Center
nGOM	northern Gulf of Mexico
NOAA	National Oceanic and Atmospheric Administration
NWLON	National Water level Observation Network
RINEX	Reciever INdependent EXchange
RMSD	Root Mean Square Difference
R_o	Rossby number
ROMSmsb	Regional Ocean Modelling System for Mississippi Sound and Bight

ROWG	Radio Operators Working Group
RRD	Rossby Radius of Deformation
Sig0	Sigma Naught
SSHA	Sea Surface Height Anomaly
STDN	Station Datum
SWH	Significant Wave Height

CHAPTER I - INTRODUCTION

1.1 Problem Statement and Proposed Contributions

Problem Statement: At all relevant timescales sea level is a critical variable for ocean dynamics, maritime activities and coastal resilience. Sea level variability can be due to tides, eddies, wind, atmospheric pressure forcing and freshwater forcing, among other causes. In this dissertation, subinertial sea level changes were considered. Subinertial sea level changes refer to as sea level variabilities due to slow varying processes having period larger than two days.

Sea level datums (mean sea levels or ranges over equal observation intervals or over equal tidal stages, taken over particular time periods or epochs) are important reference levels for cadastral boundaries, ocean modeling and navigation. Separation values of these sea level datums from geodetic datums, made possible by Global Navigation Satellite System (GNSS) positioning of tide gauges, are crucial for absolute positioning of their locations particularly in the regions of land subsidence such as much of the northern Gulf of Mexico.

The complex coastal ocean and shelf circulations in the northern Gulf of Mexico (nGOM) that result from the combined actions of different forcing mechanisms such as wind, river inflow, tides, Loop Current, Loop Current Eddies and other mesoscale eddies contribute to sea level changes (Wang et al., 2003; Weisberg & He, 2003). Sea level changes on a wide range of timescales with prominent signals on half-daily, daily, seasonal and annual periods. Good spatial coverage and temporal resolution of sea level and circulation data are required to understand the impacts of the forcing mechanisms on sea level variation. However, sea level observing systems in the nGOM have limited spatiotemporal coverage.

1.2 Overview and Motivation

1.2.1 VDatum

Any measurements of sea level are referenced to a vertical datum. The simplest vertical datum is the zero of the sea level gauge (“Gauge Datum”, or “Station Datum”), though this is not a useful reference for comparing with sea level at other locations. From sufficient time series of sea level measurements, the value of other sea level datum, such as Mean Sea level (MSL) or Mean Lower Low Water (MLLW) can be determined with respect to Station Datum (STDN).

Sea level gauges can be disturbed, moving STDN in the vertical. For this reason, a set of tidal benchmarks on land are leveled to the gauge, from which a gauge’s STDN can be reset. Leveling between the benchmarks allows for checking if any benchmarks themselves have been disturbed in the vertical. However, if the benchmarks have all moved together in the vertical, due to phenomena such a subsidence or continental uplift, this may go undetected. However, if a sea level gauge, and/or benchmarks, are surveyed using GNSS point positioning to a geodetic datum, such as NAD83(2011), any change in vertical position of any of these components can be checked. The vertical distance from the geodetic datum to STDN, or any other water-level datum, is termed a separation value. If enough locations have measured separation values, or observations are augmented with tidal modeling, separation surfaces, also known as separation models, can be constructed. These separation models have a wide range of utility for purposes such as combining data collected with respect to different vertical datums (e.g., land elevations with respect to a measure of MSL and water depths with respect to MLLW).

National Oceanic and Atmospheric Administration (NOAA) has developed a Vertical Datum (VDatum) tool, with separation models for various vertical datums, including using a geoid separation model (GEOID 12B) that is used for NAVD88. Using VDatum, elevations can be seamlessly transformed between geodetic, tidal and orthometric reference frames (https://vdatum.noaa.gov/). This was the reason for the development of the VDatum model around the coastal regions of the United States of America (https://vdatum.noaa.gov/). The VDatum grid is location specific and developed differently for the various coastal regions (Yang, Myers, & White, 2010). The MSB is in both the eastern Louisiana and Mississippi VDatum grid and Gulf of Mexico (GOM) and Alabama Bays VDatum grid.

One issue facing the estimated sea level in the MSB is the performance of the vertical datum transformation model (VDatum) in the region. NOAA warned that the VDatum uncertainties are larger than the published uncertainty of ± 17 cm in some regions of eastern Louisiana and western Mississippi part of the nGOM (https://vdatum.noaa.gov/). The localization of these regions will be useful in the improvement of the VDatum model.

Proposed Contributions: By determining areas where VDatum uncertainties are not within the published uncertainty, adequate efforts can be made to fix the issues in the performance of the model and/or the Topography of Sea Surface (TSS) for specific regions. By making the estimated sea level absolute, it can be used to validate the outputs from the SWOT altimeter which will be launched in September 2021 (https://swot.jpl.nasa.gov/mission.htm) and for interpolating the satellite altimeter data in time. Additionally, estimates of the contributions of mesoscale processes to changes in sea level from this study if assimilated in ocean models can improve the spatiotemporal coverage of sea level data and the forcing mechanisms could be used to validate model parameters.

1.2.2 Dynamic Water-Level

The dynamics of the Mississippi Bight (MSB) are due to several physical mechanisms such as winds, river inflow, tides and eddies. The contributions of these mechanisms to the dynamics of the nGOM system are at different temporal and spatial scales (Cazenave et al., 2001; Sturges & Leben, 2002). Sea level is one of the oceanographic properties of the nGOM, which varies in response to these physical processes and the variation is at different temporal and spatial scales (Donoghue, 2011; Church & White, 2006; Cazenave et al., 2001).

Given the different temporal and spatial scales at which variations in sea level take place, there is need for an adequate sea level observation system. This dissertation aims to develop an enhanced sea level observing system in the northern Gulf of Mexico by estimating subinertial differential sea level from High Frequency Radar (HFR) surface current data in the Central Gulf of Mexico Ocean Observing System CODAR coverage area. Though there is an unknown spatial offset in the estimated sea level, the output are on regular grid, which is similar to the surface currents. The coverage area is not limited to the coastal region but extends to the shelf region. Temporal resolution of the estimated sea level can be similar to the temporal resolution of some of the sea level observations in the coastal region. This method of sea level estimation will be adopted in this study to estimate the variability in MSB sea level gradient. Additionally, the combined analyses of the surface current and resulting sea level gradient could reveal the contributions of the mechanisms to the variability in Mississippi Bight sea level gradient.

1.3 Study Area

Figure 1.1 gives a synoptic view of the research area in the Mississippi Bight. It is bordered to the west by the Louisiana coast, the north by Mississippi and Alabama coasts and the northeast and east by the Florida coast. A chain of barrier islands separates it from other water bodies such as Chandeleur Sound, Mississippi Sound and Mobile Bay. Furthermore, to the west is the Mississippi River bird foot delta. The region has an irregular continental shelves on the north and east are broader when compared to the continental shelf on the west. Continental slope on the eastern region is the gentlest when compared to the continental shelves of northern and western regions. The HFR stations locations are shown relative to the MSB and the HFR coverage region at 6 km × 6 km grid resolution spans from a bathymetry of as low as 30 m to depths greater than 1000 m. It also covers the western part of the DeSoto canyon, which implies that the some aspects of the mesoscale and sub-mesoscale processes that take place in the DeSoto canyon (Wang et al., 2003; Weisberg et al., 2005) might be captured in the HFR data. The figure also shows the various locations of the wind stations with respect to the HFR coverage region.

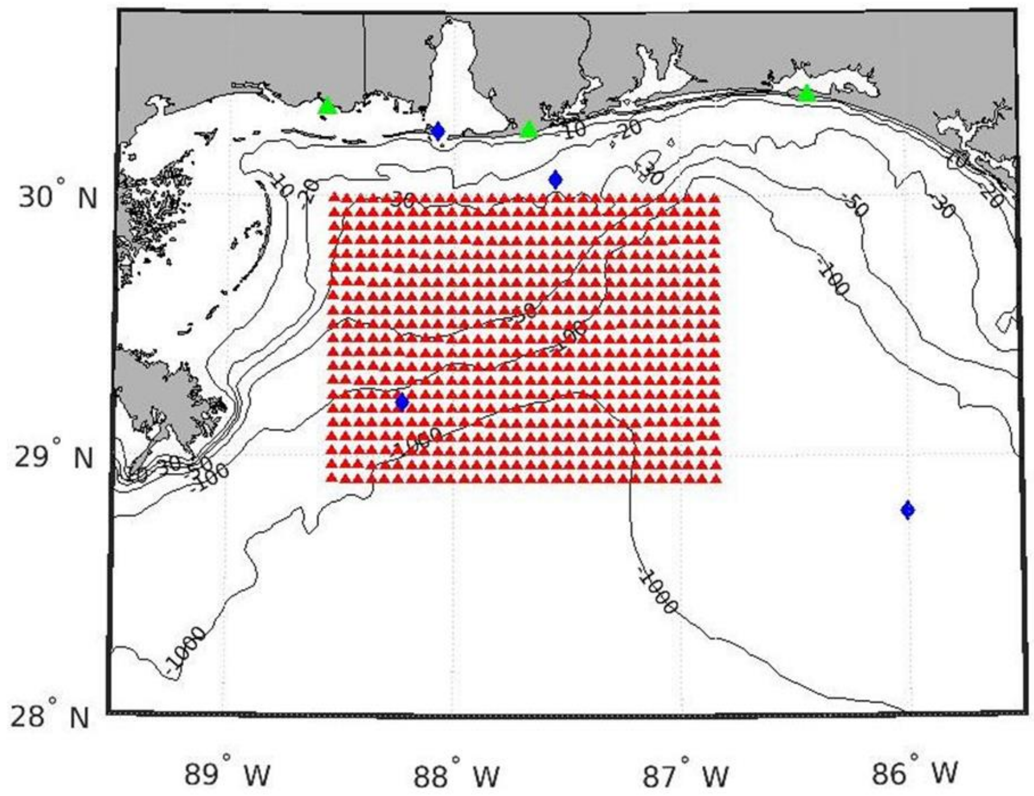

Figure 1.1 *The various wind stations (blue diamonds: starting from the northmost and moving in the clockwise direction dpia1, 42012, 42039 and 42040), the ~5 MHz HFR stations (green triangles) located at Singing River Island, Orange Beach and Henderson Beach State Park (from left to right) and surface current grid points (red triangles).*

1.4 Discussion of the Mechanisms of nGOM Circulation

In the south-east of the GOM, the LC (Fig. 1.2), being the continuation of the Yucatan current in the Yucatan strait, is the major circulation feature of the GOM. The LC becomes the Florida Current and exits the GOM through the Strait of Florida as the Gulf stream (Oey et al., 2005). The LC transports about 27 Sv (Sv = 10^6 m^3/s) of warm water (Yuley, 2013). Before LC intrusion commences, its position is to the south-east region of the GOM while during intrusion LC can extend northwards towards the nGOM (Jochens & Nowlin, 1998; Weisberg & He, 2003). The proximity of the LC to the shelf plays a role in the sea level gradient along the shelf as noted along the West Florida Shelf (Sturges & Evans, 1983; Li & Clarke 2005).

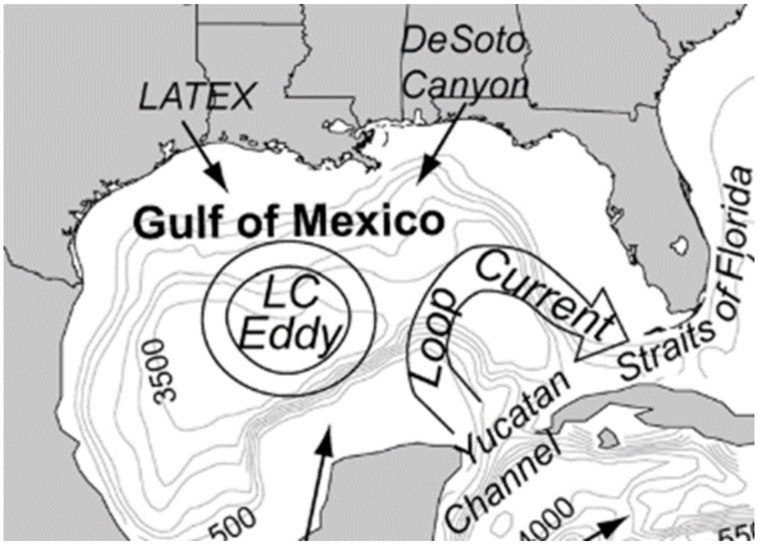

Figure 1.2 *The Gulf of Mexico, a sample of a Loop Current Eddy, a sample of the Loop Current, the DeSoto Canyon, the Yucatan Channel and Straits of Florida. (Source: Oey et al., 2005).*

Anticyclonic LCEs are generated by the baroclinic instability of the LC and further drive the complicated circulation in the GOM (Schmitz et al., 2005). They are warm core eddies, with elevated sea surfaces of about 0.6 m (Kim, 2010; Rudnick et al., 2014). As the LCEs separate from the LC, they have a tendency to drift west of the GOM and affect upper ocean circulation as they propagate (Nowlin et al., 2005). Northernmost propagation of the LCEs in the nGOM is in the region of the DeSoto canyon (Jochens & Nowlin, 1998; Weisberg & He, 2003). However, based on their size and shallow shelf bathymetry, they are constrained offshore of the shelf break (Wang et al., 2003; Weisberg et al., 2005). At the shelf break, LCE volume and angular momentum are reduced and small-scale cyclonic rings and jets are produced (Oey & Zhang 2004).

In addition to the LC and LCEs, mesoscale cyclonic eddies are found in the GOM. Cyclonic eddies contribute to the generation of the LCEs. They interact with the extended loop of the LC leading to the shedding of the LCEs (Rudnick et al., 2014) and can constrain the northwards extensions of the LC (Schmitz et al., 2005). The cyclonic eddies are smaller in size when compared to the LCEs, short-lived and can be barotropic as noted in (Rudnick et al., 2014). Due to their smaller sizes, they propagate further onshore when compared to the LCEs and create sea level gradients as water is pushed towards the shore (Finnegan, 2009).

Wind stress plays a significant role in circulation on the nGOM shelf as it is noted to be the primary forcing mechanism (He & Weisberg, 2003b; Morey et al., 2003a; Dzwonkowski & Park, 2010; Greer et al., 2018). Cases of steady wind can result in the formation of a surface Ekman layer, which is modified as the surface flow from outer shelf region (deep so that the flow does not feel the sea floor) enters the inner shelf region, thereby, complicating shelf circulation (Weisberg et al., 2005). The presence of the coastline enhances sea level set-up (onshore Ekman transport) and set down (offshore Ekman transport) depending on wind direction with respect to the coastline (Johnson, 2008; Weisberg & He 2003; Lentz & Fewings, 2012). This subsequently results in across-shelf sea level gradient and associated geostrophic currents where high sea level is to the right (in the northern hemisphere) of the current (Weisberg et al., 2005). This was corroborated by Nowlin et al., (2005) when they showed cold upwelled water on the west of Cape San Blas. Weisberg & He (2003) further stated that the interaction between wind stress, LC and buoyancy forcing led to upwelling along the west Florida shelf break and in the distribution of the upwelled properties on the shelf.

Buoyancy forcing also influences the dynamics of the nGOM. Buoyancy forcing in coastal regions is considered to be local and it is driven by surface heating, precipitation and river inflows (Weisberg & He, 2003). River inflows are sources of fresh water supply to the MSB and the major sources are: Mississippi river, Mobile Bay, Pearl River and Pascagoula River (Dzwonkowski & Park, 2010; Dzwonkowski et al., 2014; Greer et al., 2018).

Diurnal and semidiurnal tides are the predominant types of tides observed in the GOM. Reid & Whitaker (1981) noted that the local tidal potential generates quasi-resonant cyclonically rotating shelf waves, which comprise the M2 tide. Gouillon et al., (2010) supported this view and posited that the amphidromic point for M2 was north of Yucatan peninsula while S2 does not have amphidromic point. The nGOM experiences diurnal tide having a microtidal range of about 0.5 m and K1 as the dominant tidal constituent (Hayes, 1979). Additionally, there are inertial oscillations in the GOM and they have similar periods as the diurnal tide. It is challenging to separate the two processes. Unlike inertial oscillations, tides result in changes in sea level (Chavanne & Klein, 2010).

1.5 Related Studies

Sea level has been observed using various techniques. In the US, coastal sea level observing systems include the NOAA National Water level Observation Network (NWLON), the USGS set of coastal gauges, and some stations operated by the US Army Corps of Engineers. The issue with the sea level observations from these systems is that they have poor spatial resolutions and do not provide sea level information offshore of the coastal regions (https://tidesandcurrents.noaa.gov/). Additionally, if the gauges were not referenced to a geodetic reference frame vertical displacements in the regions surrounding the gauges might go unnoticed. Multipath signals from GNSS that are reflected off of the sea surface and received using a single GNSS antenna and receiver have been used to estimate sea level (Larson et al., 2013). While sea level observation using this technique ties the measurements directly to a geodetic reference frame, the technique is also limited to the coastal region. Offshore sea level can be measured using a GNSS installed on buoys (Nwankwo et al., 2017a,b) but they are similar to coastal gauge with regards to spatial resolution. Although satellite altimeters have made offshore water-level possible, along-track satellite data are rather at both poor temporal and spatial resolutions and are subject to more errors on the continental shelf. Gridded altimeter products provide sea level at regular but coarse spatial resolution (Chavanne & Klein 2010; Roesler, 2013).

Various techniques have been adopted in measuring water column or sea surface currents. Estimates of water column currents are determined using downward-looking (Liu et al., 2012), upward-looking (Dzwonkowski & Park, 2010) or ship-moored (Wang et al., 2003) Acoustic Doppler Current Profilers (ADCPs). The estimated water column currents could also be extrapolated to the surface to estimate surface currents (Dzwonkowski & Park, 2010). Several remote and in-situ methods have employed for surface current measurements. Both Kelly and Strub (1992) and Bowen et al., (2002) using Maximum Cross Correlation (MCC) techniques estimated surface currents from satellite radiometer images. One of the challenges of this remote technique is cloud cover. Cloud cover is not an issue when using drifters to determine surface current as they provide in-situ measurements. However, numerous drifters are required to sample an area. Surface current sampling using drifters is not regular and entrainment of drifters by large-scale features such as eddies could potentially transport them away from an area of interest. As a result, drifters do not have long lifespan (Ohlmann et al., 2001). Surface currents could also be estimated from along-track satellite altimeter data (Ohlmann et al., 2001). However, the technique results in the amplification of any high frequency noise present in the data.

The advent of HFR radar made surface velocity estimation easier and faster. The method is based on the principle of Bragg scattering; which involves Bragg waves reflecting the radar signals that are two times their wavelength. HFR has been used in the estimation of tidal and wind driven currents (Prandle, 2012), internal wave-driven surface currents (Shay, 2012) and larval transport (Bjorkstedt & Roughgarden, 2012). Roesler (2013) extracted geostrophic currents from the surface currents captured by HFR, fitted a stream function to the geostrophic current to estimate differential sea level which were used to validate altimeter coastal retrackers. Hence, HFR data is useful as it can be used to estimate ocean circulation as well as changes in sea level.

1.6 Hypothesis and Objectives

1.6.1 Hypothesis

- The model (ADCIRC) used to develop VDatum in the region did not accurately simulate the spatial variabilities of various mean tidal ranges.
- Geostrophic balance is the dominant balance for subinertial currents in MSB.
- Variability in MSB sea-level gradient in response to physical processes is reflected in the dominant empirical modes.

- Loop Current and Loop Current Eddy do not remotely influence sea level changes on the shelf of the MSB.

1.6.2 Objectives

- Establishment of tidal datums on USGS gages to the NAD83(2011) ellipsoid in the MSB and a comparison to VDatum outputs to determine in which areas the magnitudes of the residuals are not within the maximum uncertainty.
- Diagnosing all the terms in the momentum equations except the sea level gradient terms comparing them to the Coriolis term. This will help determine the significance of other terms in the momentum equation.
- Estimation of sea level anomalies based on Geostrophic balance approximation and based on significant terms in the momentum equation. These results are compared to satellite altimeter along-track.
- Computation of Empirical Orthogonal Function analysis on the sea level anomalies to determine the dominant modes in the changes.
- Investigation of the impact of the following physical processes to changes in MSB sea level: anticyclonic and cyclonic eddies, Loop Current and winds.

CHAPTER II - VALIDATION OF VDATUM IN SOUTHEASTERN LOUISIANA AND WESTERN COASTAL MISSISSIPPI

2.1 Introduction

This study, presents a novel technique for estimating the errors in the NOAA's vertical datum transformation tool (VDatum) in the northern Gulf of Mexico. It involved using sea level data that were not intended for geodesy or tidal applications. Tidal datums were established on three USGS coastal stations in the northern Gulf of Mexico and a coastal HydroLevel buoy and the tidal datums were linked to orthometric and ellipsoidal datums. For the USGS stations, this was accomplished using Global Positioning System (GPS) surveys and tidal datum transfers from NOAA NWLON gauges to the USGS stations (NOAA CO-OPS., 2003).

Datums to be used as reference frames for positioning on the earth are traditionally separated into horizontal and vertical. More modern geodetic datums, such as North American Datum 1983, National Adjustment 2011 (NAD83(2011)) can be used for both vertical and horizontal positioning. Vertical datums are broadly grouped as tidal, ellipsoidal and orthometric. In the United States (U.S.), tidal datums are mean elevations of different tide stages and ranges averaged over particular periods (epochs) of 19 years or shorter when land subsidence or uplift rates exceed a certain threshold (NOAA CO-OPS., 2000). The present 19-year epoch for tidal datums in the U.S. is 1983-2001. U.S. law requires Mean Lower Low Water (MLLW; NOAA CO-OPS., 2000, 2003) as the chart datum for depths in coastal waters. Geodetic datums are meant to be sized and oriented to best fit the earth's geoid, centered on the center of mass of the entire solid, liquid and gaseous earth, with semi-minor axis oriented to the conventional pole and a prime meridian initially coincident with the Greenwich meridian (e.g., Smith, 1987). A 3D-ellipsoid which best fits the global geoid is the Geodetic Reference System 1980 (GRS80) (Moritz 1988, vol. 62) and an associated datum is the NAD83 (Schwarz 1990). The center of this datum has been found to be about 1.5 m offset from the true center of mass where the center of the World Geodetic System 1984 (G1674) (WGS84(G1674)) (Malys et al., 2016) is located. Orthometric datums are meant to be surfaces of constant geopotential. The U.S. orthometric datum is the North American Vertical Datum 1988 (NAVD88) (Dilkoski et al., 1992). Separation surfaces of the datums are shown in Fig. 2.1.

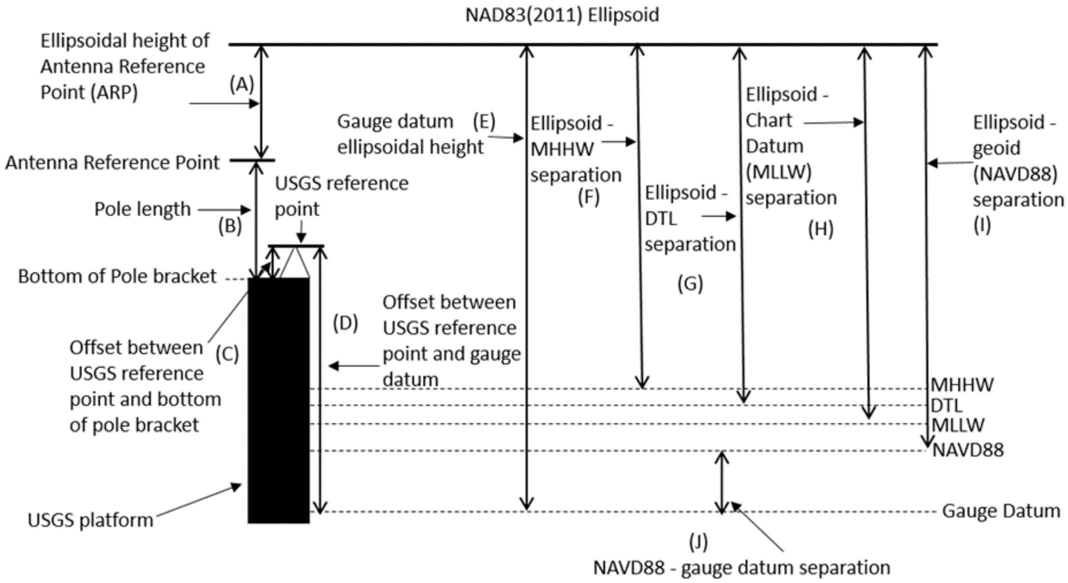

Figure 2.1 *Vertical schematic of datums, temporary GNSS antenna deployments and USGS sea level gages. USGS reference point at CSX RR is on the ladder attached to the platform, at both the Rigolets and Delacroix it is on an aluminium bracket on the platform. "C" is positive for reference point above pole plate bottom. Grafnav solutions were output with respect to the antenna reference point, which is at the bottom of the antenna.*

Datums adopted by different agencies for vertical measurements are often different, and hence an interfacing project such as shoreline delineation (demarcation between water and land environments) carried out individually by these agencies may not overlap adequately due to differences in their adopted datums (Parker 2002). The NOAA utilizes the NAD83(2011) datum for horizontal positioning. Bathymetric soundings collected by NOAA are with respect to the MLLW while, for overhead obstructions, Mean High Water (MHW; NOAA CO-OPS., 2003) is used (Hess et al. 2003; Parker 2002). The USGS uses NAVD88 (GEOID12B, epoch 2010.0) for topographic surveys as well as for sea level observations, though there are some legacy uses of earlier versions of NAVD88 (Parker et al. 2003) and National Geodetic Vertical Datum 1929 (NGVD29). For this paper NAVD88 will be used to refer to NAVD88 GEOID12B, epoch 2010.0 with other versions explicitly noted. The NAD83(2011) ellipsoidal height of NAVD88 is currently approximated by the GEOID12B model. Although the NAVD88 surface is not the same as the global geoid, in this report it will be referred to as the geoid.

The NOAA National Ocean Service (NOS) VDatum (Hess et al. 2003) is used to transform among 36 vertical datums categorized into ellipsoidal, orthometric and tidal datums (https://vdatum.noaa.gov/about.html). This vertical transformation tool can be used, for example to transform shoreline heights between different vertical datums which satisfies the need for data to be seamlessly converted between datums used by different agencies. Parker (2002) noted other ways that VDatum is useful including: development of the National Bathymetric Database from which Electronic Navigational Charts (ENC) can be developed, delineation of Marine boundaries and utilization of 3rd-party bathymetric data with high integrity irrespective of its reference datum. Furthermore, Strauss et al. (2012) used VDatum to determine Mean High Water (MHW) and estimated the population of the contiguous United States vulnerable to sea level rise and flooding.

VDatum allows for data collection using GNSS receivers, referenced to geodetic ellipsoid systems, such NAD83(2011), to be seamlessly transformed to tidal or orthometric datums. In hydrography, GNSS has provided the opportunity to measuring sounding to the ellipsoid and conduct hydrographic surveys without having to measure tides and account for vessel settlement and squat during surveys (Dodd and Mills 2012). Since VDatum provides the separation model between the ellipsoid and the tidal datums, the soundings from these so-called Ellipsoidally Referenced Surveys (ERS) are able to be reduced to chart datums (tidal datums).

VDatum has been regionally implemented across the U.S. The VDatum marine grid of interest for this project, covers eastern Louisiana and Mississippi coastal waters and several processes were undertaken towards its development. It was constructed using a regional tidal model, tidal datums from operational tide gauges, tidal datums published on benchmarks for previously working tides gauges, and GPS surveys of those benchmarks and/or tide gauges for geodetic NAD83 (2011) coordinates (Yang et al., 2010). ADvanced CIRCulation (ADCIRC; Westerink, Luettich and Muccino 1993) hydrodynamic model for the region was forced using nine tidal constituents at the boundary nodes and was integrated for 65 days. A tidal harmonic analysis was performed on the 6-minute interval sea levels from the final 55 days of the integration period. All of the tidal datums for the model, including Local Mean Sea Level (LMSL), are computed from a 19-year harmonic sea level prediction based on harmonic analysis of model output and are transformed to be relative to the LMSL rather than model zero. The tidal models set the tidal ranges over the domain and hence low and high water datums from the resting model sea surface (model zero). The resulting model tidal datums at the coastal sea level stations managed by NOAA were compared to Mean Sea Level (MSL) referenced tidal datums on the coastal sea level stations. Tidal Constituents and Residual Interpolation (TCARI, Parker et al. 2003)) was used to interpolate the range residuals at the sea level stations to the tidal datum fields. The resulting corrected tidal datum field was interpolated on to the VDatum marine grid. The conversions between the NAD83(2011) ellipsoid (hereinafter referred to as the ellipsoid) and tidal datums go through NAVD88, which requires the Topography of the Sea Surface (TSS) defined as NAVD88 - LMSL, where the relationship between the ellipsoid and NAVD88 is given as a geoid model (e.g., GEOID 03). Note that this TSS is not the same as the mean sea surface dynamic topography relative to the global geoid that results from mean geostrophically balanced currents (see Yang et al., 2010 for details).

Estimated TSS is interpolated and extrapolated on to the TSS grid. The gridded TSS, through the geoid models, gives ellipsoid separations throughout the grid. Two methods are used to estimate the TSS, a direct method at NWLON stations and an indirect method at NGS tidal benchmarks (Yang et al., 2010). In either method, subsidence can introduce errors in TSS. If a GPS survey of the benchmark or tide station is done at some point after tidal datums have been published, and subsidence has occurred in the intervening time, it will cause any published tidal datums to have their ellipsoid separation values to be in error as well as their vertical relationship to NAVD88.

VDatum uncertainties are computed for all the VDatum grids around the United States. Sources of these uncertainties result broadly from the gridded fields used in datum transformation and the observational data used to constrain model results (https://vdatum.noaa.gov/docs/est_uncertainties.html). VDatum uncertainty for eastern

Louisiana and Mississippi coastal marine grid (0.171 m) is the third highest in the U.S. The uncertainty was calculated as the square root of the sum of squares of the uncertainties in the various datum transformation components (https://vdatum.noaa.gov/docs/est_uncertainties.html ‘Table 3’). The hydrodynamic model and statistical interpolations used in developing the modelled tidal datum could contribute to this uncertainty. Uncertainty in the NAVD88-LMSL (TSS) (0.148 m) is largest among the other components and this was largely due to how the TSS was developed (see Yang et al., 2010 for details). Yang et al., (2010) stated that observation stations used to constrain model results were sparse especially in the Louisiana area and this would significantly affect both the TSS and modelled tidal datum uncertainties. For this region, NOAA has a warning on the VDatum page that states the following:

“Important: Transformation Uncertainties in the ‘Louisiana / Mississippi - Eastern Louisiana to Mississippi Sound’ Regional Model, have been found to range from 20 to 50 cm in particular locations from the Mississippi River Delta north to Lake Pontchartrain. These issues most likely can be attributed to subsidence, newly established datums, and changes to the understanding of NAVD88 based on new versions of the GEOID. The VDatum Team is currently looking at resolving these uncertainties” (https://vdatum.noaa.gov/welcome.html).

The rest of the paper is organized as follows. Section 2 describes the methods employed in data collection. It also details how different processing techniques were used in data processing. The outcomes of the data processing as well as analysis were presented in section 3. Findings were discussed in section 4 while conclusions drawn from the study were presented in section 5.

2.2 Methodology

USGS coastal sea level and HydroLevel buoy stations in the region used for this study are shown in Table 2.1 and Fig. 2.2. Stations were at the CSX railroad bridge over the East Pearl River (CSX RR), the Highway 90 bridge over the Rigolets pass between Lakes Bourne and Pontchartrain (Rigolets) and Crooked Bayou near Delacroix Louisiana (Delacroix). Table 2.2 shows the positions of CSX RR, Rigolets and Delacroix USGS gauges. An additional USGS gauge in Bogalusa, Louisiana, (Bogalusa) in the non-tidally influenced part of the Pearl River, was used to ensure that periods of flood stage for the river were not used for the tidal datum transfer for the USGS station near the mouth of the river. The HydroLevel buoy was deployed close to the Chandeleur East Island (Chandeleur East buoy).

Table 2.1 *Station numbers and locations of the USGS and NOAA sea level gages used.*

Agency	Station id	Location	Abbr. name
USGS	301141089320300	East Pearl River at CSX Railroad Near Claiborne, MS	CSX RR
USGS	02489500	Pearl River near Bogalusa, LA	Bogalusa
USGS	301001089442600	Rigolets at Hwy 90 near Slidell, LA	Rigolets
USGS	073745257	Crooked B. NW of L. Cuatro Caballo near Delacroix, LA	Delacroix
NOAA	8761305	Shell Beach, LA	SB
NOAA	8743437	Bay Waveland Yacht Club, MS	BW
NOAA	8760922	Pilots Station East	PSE
NOAA	8760721	Pilottown	PT

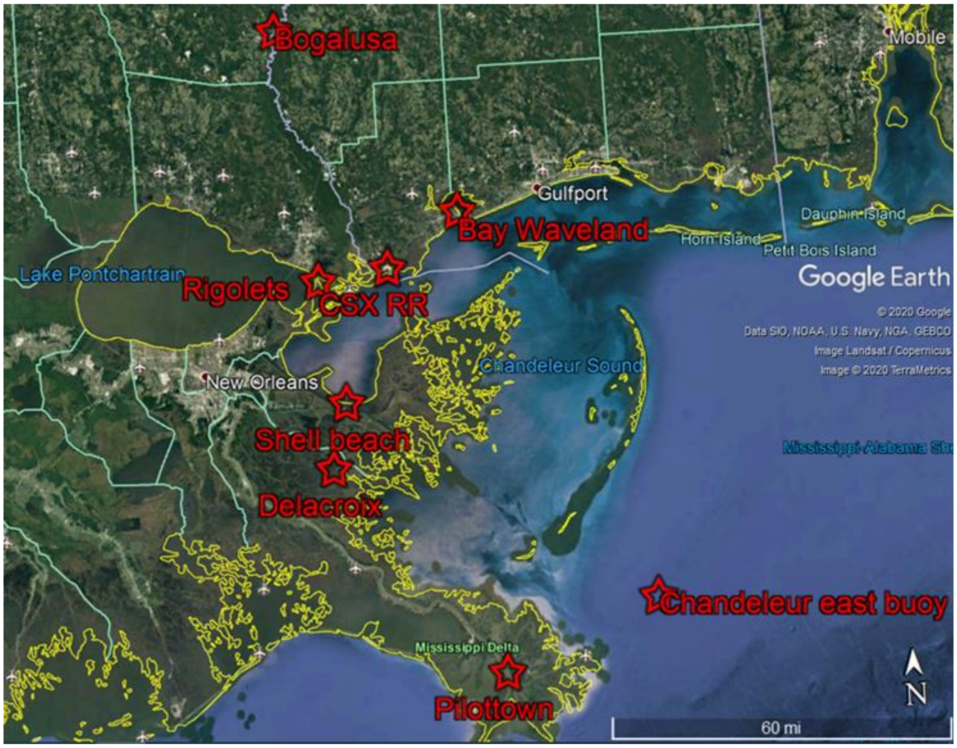

Figure 2.2 *Locations of the sea level stations.*

Table 2.2 *Gage zeros from survey reference marks, gage zero to NAVD88 GEOID 12B and potential subsidence at the various stations.*

	Latitude NAD83(2011)			Longitude NAD83(2011)			Reference mark elevation above gage datum (USGS)		NAVD88 elevation above gage datum (USGS)		Potential subsidence
Abbr. name	Deg	Min	Sec	Deg	Min	Sec	ft	m	ft	m	m
CSX RR	30	11	41	-89	32	03	12.46	3.80	GEOID 12B EPOCH 2010.000 (6/3/2015)		-0.08± 0.06
									0.34	0.10	
Rigolets	30	10	01	-89	44	26	15.00	4.57	GEOID 12B EPOCH 2010.000 (6/16/2012)		0.01± 0.06
									0.997	0.30	
Delacroix	29	42	29	-89	43	10	14.07	4.29	GEOID 12B EPOCH 2010.000 (6/1/2016)		-0.22± 0.04
									4.20	1.28	

The methods for determining the vertical separations between the ellipsoid and the tidal datums at the USGS sea level gauges and the HydroLevel buoy were similar in concept, though differed in detail. GPS observations at the USGS stations were used to obtain the vertical separation between the ellipsoid and the gauge zero using station positioning. In the case of the Chandeleur East buoy, the GPS observations were not static as the buoy moved about its watch circle due to the contributions of waves and currents. Using the kinematic data, the separations between the NAD83(2011) ellipsoid and the sea level were determined. At all the USGS stations and the Chandeleur East buoy, tidal datum transfers from NOAA NWLON primary gauges were conducted following NOAA CO-OPS (2003).

2.2.1 GPS Positioning

GPS surveys were carried out at the USGS stations. This involved the installation of Trimble Zephyr Geodetic model 2 antennas, a Trimble GPS NetRS receiver (only tracks GPS signals; Trimble NetRS User Guide) at the CSX RR and Rigolets stations and a Trimble GNSS NetR8 receiver (tracks GPS and GLONASS signals; Trimble NetR8 User Guide) at the Delacroix station (note GLONASS data were not used). The receivers were configured to log data at 1Hz. The two major concerns during the GPS survey were signal blockage and multipath as they are dependent on the receiver-satellite obstruction geometry hence, repeat as a satellite repeats along its track (Choi, 2007). In order to mitigate GPS signal blockage at the CSX RR station, the GNSS antenna was mounted on a pole that was tall enough to ensure that GPS signals were not shaded. Figure 2.3 shows that the antenna had a clear view to the sky as it was above the railroad. However, we assume that the GPS signals were shaded during passing vehicles and trains which will result in the receiver losing lock on some satellites that were tracked. This was confirmed in the irregular nature of missing data in the observation Receiver INdependent EXchange format (RINEX) (The Receiver Independent Exchange Format 2015) data at the CSX RR station. GNSS antenna at the Rigolets had the worst sky view. Though the antenna at the Rigolets was mounted on a pole (Fig. 2.4), signal blockage close to the zenith of the antenna was still a concern due to the highway 90 bridge was about 21.34 m above the pile-cap where the GNSS antenna pole was installed. Hence, the station’s GPS data were assumed to be most vulnerable to signal blockage. A regular pattern of missing data was observed in the observation RINEX file for some satellites at the Rigolets station and this was attributed to signal blockage due to the presence of the bridge structure. GPS signal blockage was not a concern at the Delacroix station as the station was not located on any platform that could potentially shade GPS signals (Fig. 2.5). Multipath influence at the USGS stations were mitigated using modified sidereal filtering (Choi, 2007).

Figure 2.3 *GPS setup at CSX RR station.*

Figure 2.4 *GPS setup at the Rigolets station*

Figure 2.5 *GNSS setup at Delacroix station*

Raw Trimble GPS data observed at the USGS stations were post-processed after data collection. Before post-processing, the Trimble GPS data were converted to RINEX from the Trimble format using a Trimble Business Center utility called Convert to Rinex software version 3.1.3.0 (https://www.trimble.com/support_trl.aspx?Nav=Collection-773&pt=Trimble%20RINEX#menu-right). GPS RINEX data was post-processed in static mode using Novatel Waypoint Software GrafNav version 8.70 (Waypoint Products Groups 2016) to obtain the antenna 3-D geodetic coordinates. The maximum period of raw files allowable in this mode is three days. As such, only the three consecutive days of data when there was daily full coverage were used in the case of CSX RR and Rigolets. GPS raw files from the Delacroix station was longer in period than those from CSX RR and Rigolets. Hence, two separate three-day data sets were post-processed and the arithmetic mean of the two was used. The base-stations used in processing the files were continuously Operating Reference Station (CORS) MSIN for the CSX RR and Rigolets stations and SBCH for the Delacroix station. Forward and backward processing directions were selected to enhance in integer ambiguity resolution. The end product of the GPS post-processing was an estimated antenna ellipsoidal height which was needed to estimate the ellipsoidal height of each USGS station's gauge datum.

2.2.2 Tidal Datum Transfer

Establishment of tidal datums by first reduction [i.e., by computing datums directly from 19 years of data over the accepted National Tidal Datum Epoch (NTDE), NOAA CO-OPS 2003] on a sea level station requires at least 19 years of uninterrupted sea level records observed at that station; 19 years encompasses the 18.6-year period of the regression of the lunar nodes. For shorter data records, tidal datum transfer techniques are used (NOAA CO-OPS 2003). For the diurnal tides in the northern Gulf of Mexico, the Modified-Range Ratio Method (MRRM) is used for tidal datum transfer. We focus our attention to the following tidal datums: MLLW, mean higher high water (MHHW), diurnal tide level (DTL), great diurnal range (Gt).

The tidal datum transfer methods are based on comparison of simultaneous sea level records at both the secondary and primary gauges, and the accepted datums at the primary gauge. For this study, the secondary stations are the USGS gauges and the HydroLevel buoy and the primary gauges are NOAA NWLON gauges. The choice of primary gauge was based on location and tidal characteristics relative to the secondary gauge and data availability (NOAA CO-OPS 2003). In our case, we chose the closest NOAA sea level station (closest along a water route) which fulfilled these requirements. Software was written (hereinafter referred to as USM software) in MATLAB® for datum transfers from the primary gauges to the secondary gauges. The first step in the software was to perform a tidal harmonic analysis of the secondary gauge sea level record using UTide (Codiga 2011). The first derivative of the tidal constituents (sinusoids at each of the tidal speeds with fitted amplitudes and phase) was computed by multiplying each constituent by the negative of its angular speed and subtracting a phase of p/2 from its arguments. The local extrema are initially estimated where the derivative is zero. At each of these local extrema, a cubic function was fitted to 2 h of sea level data on either side of each zero slope and the zero crossing of the first derivative within the 2-h record was taken as time of the extrema and the function evaluated at that time was taken as the value of the extrema. This follows the instructions by US Coast (1965) that when finding the high water or low water to take a smooth arch covering an hour or more about the extrema. These extrema are then matched with corresponding ones from the primary gauge, in a semi-automated process, and the type of extrema (e.g., a higher high water or lower low water) are noted to match those at the primary gauge. The analyst then reviews the matched extrema to correct for any mismatches. For example, in this micro-tidal environment, near neap-tides there may be more local extrema at either the primary or secondary gauges. Extrema mismatches between primary and secondary gauge sea level records were eliminated. The matching extrema from both gauges are then put into a spreadsheet, along with the accepted datums at the primary gauge, to perform the MRRM tidal datum transfer following NOAA COOPS (2003).

2.2.3 Utilizing USGS Coastal Sea level Gages

USGS sea level gauges used for stage measurement are installed and operated to standards outlined in Saur & Turnipseed (2010). The overall stage accuracy is required to be 0.01 foot (0.003 m) or 2% of the effective stage, whichever is greater, where effective stage is the sea level above gauge zero. The accuracy applies to the sum of all the error components. In comparison, NOAA requirements for sea level gauges in microtidal regimes, like the northern Gulf of Mexico, are 0.001 m resolution and 0.020 m accuracy per 6-minute observation relative to datum (NOAA, NOS 2020).

Datasets used for this project at the USGS stations are: sea levels relative to gauge zero, vertical offsets from gauge zero to a reference mark (provided by USGS), measured vertical offsets between the reference mark and GPS antenna installed for the project, the GPS data collected for the project and river discharge at Bogalusa. For the USGS gauges, the sea level data were at 15-min intervals and with respect to the gauge datum. Sea level data from the NOAA stations used in tidal datum transfers to the USGS stations were at 6-min intervals and with respect to the station datum.

2.2.3.1 USGS 301141089320300 EAST PEARL RIVER AT CSX RR

A field survey was conducted at the site on 5 March 2018. The pole on which the GNSS antenna was mounted was leveled to be vertical and fastened to a frame as shown in Figure 2.3 using hose clamps. The vertical offset between the antenna reference point (APR) and the USGS station's reference mark was estimated using a measuring tape along with an I-beam spirit level. The offset between the reference mark and the gauge datum as well as that between the gauge datum and NAVD88 were provided by USGS. A solar panel was fastened to the same frame supporting the GNSS antenna pole (Figure 2.3). The solar panel ensured that both the external batteries and the GPS receiver inbuilt batteries were fully charged throughout the survey period. The GPS receiver and external battery were secured in a protected case whereas the GPS receiver logged data. The site was revisited on 5 March 2018 for de-installation of the equipment. The offsets that were measured initially were re-measured before de-installing the GNSS antenna and solar panel.

For this station near the mouth of the East Pearl River, consideration was given to whether river stage would affect the results of the tidal datum transfer. Flood periods were based on statistics. The average of the annual-mean river discharge ranging from 1939 to 2017 for Bogalusa station (USGS), upstream of the CSX RR station in the non-tidally influenced portion of the river was calculated. River discharge periods at Bogalusa from October 1, 2016 to October 31, 2017, which corresponded to the same time frame of the CSX RR sea level data were downloaded. Discharge greater than the calculated average annual-mean river discharge were categorized as flooding periods, for the purposes of this study. In order to account for a lag in discharge between the Bogalusa and CSX RR stations, sea level data 1-day after the flooding period ended were not considered.

Tidal datum transfers were conducted at the CSX RR station from NOAA's tide station 8743437 at Bay Waveland, Mississippi (primary station) (https://tidesandcurrents.noaa.gov/stationhome.html?id=8747437), using the USM software. Tidal datum transfers were computed for three cases: (1) using the entire sea level data, (2) using sea level data when discharge at Bogalusa was below decadal mean discharge at Bogalusa and (3) using sea level data when discharge at Bogalusa was -1 sigma below of the decadal mean discharge at Bogalusa. Swanson (1974) quantified uncertainties in tidal datums transfers for different lengths of time series for the U.S. East Coast, Gulf coast and West Coast. The precision of the datum transfers were estimated by conducting datum transfers using monthly blocks of data. Mean and standard deviation of these monthly datum transfers were computed and compared to the results of the above three cases. This was done to confirm if the resulting residuals were within Swanson (1974) allowable uncertainties.

Tidal datum separations to NAD83(2011) were determined from the online NOAA VDatum tool. Although the VDatum grid does not encompass the CSX RR station, the grid does reach as close as 0.5 km from the site and those results were used. The VDatum results were compared with the datum transfer results, referenced to the ellipsoid from the GPS survey.

2.2.3.2 USGS 301001089442600 Rigolets

Field survey procedures carried out for the Rigolets station were similar to those at the CSX RR station. The field survey at the Rigolets station was executed on the same day as that of the CSX RR station. Equipment used at both stations were similar except that the GNSS antenna pole length used at the Rigolets station was shorter than that used at the CSX RR (Figure 2.4). USGS also provided offsets similar to those they provided for the CSX RR station.

Sea level data was downloaded from the station. The sea level time series ranged from 1 October 2016 to 31 October 2017. Unlike in the case of CSX RR, the sea level data did not require additional processing to account for flood periods because it was located away from the mouth of the Pearl River.

Tidal datums were transferred to the Rigolets station. Datum transfer procedures used was similar to that used in the tidal datum transfer at the CSX RR station in terms of: NWLON primary station (NOAA’s tide station 8743437 at Bay Waveland, Mississippi) MRRM datum transfer and USM software. Furthermore, there were similarities in the estimation of the precision in the datum transfer procedure and in the comparison to VDatum results.

2.2.3.3 USGS 073745257 Delacroix

Similar to the previous stations, a field survey operation was carried out at the Delacroix station (Fig. 2.5) 133 days after those of CSX RR and Rigolets. The field survey operation was similar to the previous two, but the GPS data was captured using a different receiver. GPS data collection spanned a longer period from July 12-18, 2018.

Tidal datum transfer procedures and analysis at the Delacroix station closely resembled that of the Rigolets station. Downloaded sea level period spanned from 2 January 2017 to 3 April 2017. SBCH NOAA tidal station was used as the primary station in the datum transfer operation. Tidal datums estimated using USM software were compared with those generated using an online datum calculator (https://access.co-ops.nos.noaa.gov/datumcalc/) to understand whether the differences fall within the uncertainty budget for the Gulf coast (Swanson 1974). The tidal datums were then compared with VDatum output.

2.2.4 Utilizing a Naval Oceanographic Office HydroLevel Buoy

2.2.4.1 Chandeleur East Buoy

The equipment used for this part of the study was a HydroLevel buoy from AXYS Technologies that uses a GPS receiver to measure sea level to the ellipsoid taking into account the rotational and translational tilts of the buoy (Bamford 2013). The Naval Oceanographic Office (NAVO) and Leidos partnered with USM on this project which allowed for the deployment of a HydroLevel buoy offshore to make GPS observation which was similar to the study by Cheng (2005). Leidos provided the time on their survey vessel to deploy and recover the buoy. Although NAVO provided the buoy and their personnel helped process the GPS data, the final outputs were sea levels referenced to the ellipsoid.

The buoy was vandalized twice, with someone cutting the buoy from its mooring. The first time Leidos was able to recover and redeploy it. However, after the second incident, the buoy was recovered and not redeployed. Although the intent was for at least a 30-day single sea level record, the result was two short sea level records; 4-days sea level record for the first deployment and 18-days sea level record for the second deployment.

GNSS buoys are useful in offshore sea level observation and tidal datum establishment. Storm surges from hurricanes have been estimated using GNSS buoy data

(Nwankwo et al. 2017a,b, 2020). Hocker and Wardwell (2010) using data from a GNSS buoy showed that adequate tidal datums could be estimated. Hence, using the available sea level data from Chandeleur East buoy, tidal datum transfers were conducted to further investigate VDatum in the northern Gulf of Mexico. NOAA tide station 8735180 Dauphin Island was used as the primary tide station for the tidal datum transfer. Similar to the USGS gauges, the MRRM was used for the datum transformation. The transferred datums were relative to the ellipsoid. These can then be directly compared to the VDatum NAD83(2011) to tidal datum separations.

2.3 Results

Table 2.3 has composite information about the three USGS stations (CSX RR, Rigolets and Delacroix). It includes the ellipsoidal heights of the GNSS antennas (A), measured offsets (B and C) and the offsets provided by USGS (D). It also shows the ellipsoidal heights of the gauge datum (E) and the tidal datums (estimated using USM software) (F, G, H and I). For each tidal datum for a given station, there is a corresponding estimate from VDatum. The ellipsoidal height of NAVD88 was estimated using two methods: (Ia) based on our field measurements and the Geoid 12B model and (Ib) based on the NAVD88 to gauge zero offset provided by USGS (all their elevations based on GEOID03 and GEOID09 were transformed to GEOID 12B for this study), and our gauge zero to ellipsoid vertical separation value.

Table 2.3 *Field measurements and the ellipsoidal heights of the tidal datums estimated using the ellipsoidal heights determined using the GNSS antenna, the field measurements and tidal datum outputs from USM in-house software ("USM") and the VDatum outputs of the corresponding tidal datums at the Rigolets, CSX RR and Delacroix USGS stations. NAVD88 ellipsoidal height was from: (Ia) NAVD88 ellipsoidal height estimated using orthometric information outputted from Grafnav Geoid 12B and (Ib) vertical separations of NAVD88 to gage zero, provided by USGS, and our gage zero to NAD83(2011) to gage zero.*

All values in m	Rigolets		CSX RR		Delacroix	
NAD83 (2011)	VDatum (m)	USM (m)	VDatum (m)	USM (m)	VDatum (m)	USM (m)
(A) Antenna ellipsoidal height		-20.40 ± 0.03		-19.33 ± 0.03		-18.76 ± 0.02
(B) Pole length		-1.88 ± 0.001		-3.73 ± 0.001		-3.73 ± 0.001
(C) Ref. point and pole plate offset		0.04 ± 0.001		-0.04 ± 0.001		0.05 ± 0.001
(D) Ref. point and gage datum offset		-4.57 ± 0.01		-3.80 ± 0.01		-4.29 ± 0.01
(E) Gauge datum ellipsoidal height		26.82 ± 0.04		-26.93 ± 0.03		-26.73 ± 0.03
(F) MHHW ellipsoidal height	-26.21 ± 0.17	-26.38 ± 0.05	-26.32 ± 0.17	-26.48 ± 0.04	-24.82 ± 0.17	-25.12 ± 0.06
(G) Dtl ellipsoidal height	-26.33 ± 0.17	-26.49 ± 0.05	-26.54 ± 0.17	-26.70 ± 0.04	-25.05 ± 0.17	-25.24 ± 0.06
(H) MLLW ellipsoidal height	-26.45 ± 0.17	26.60 ± 0.05	-26.76 ± 0.17	-26.91 ± 0.04	-25.28 ± 0.17	-25.36 ± 0.06
(Ia) NAVD88 ellipsoidal height	-26.53 ± 0.07	-26.53 ± 0.06	-26.74 ± 0.07	-26.75 ± 0.05	-25.23 ± 0.07	-25.23 ± 0.05
(Ib) NAVD88 ellipsoidal height	-26.53 ± 0.07	-26.52	-26.74 ± 0.07	-26.83	-25.23 ± 0.07	-25.45

As discussed in the previous section, the datum transfer for the CSX RR site included steps to ensure that the sea level used for tidal datum transfer was not influenced by river discharge. The calculated mean of the annual-mean discharge for Bogalusa station was 282.34 m3/s (dashed cyan plot in Fig. 2.6). Flood periods (table 2.4) were categorized as periods when the discharge at Bogalusa was greater than this mean value. A more stringent constraint was adopted for flood periods when the discharge at Bogalusa was greater than -1σ from annual-mean discharge (dashed green plot in Fig. 2.6). Red and black plots in Fig. 2.6 show the sea level at CSX RR during the respective flood periods considered while the blue plot show the non-flood periods which was used for the tidal datum transfer. As such, the result of the three different cases of tidal datum transfer at CSX RR are shown in table 2.5.

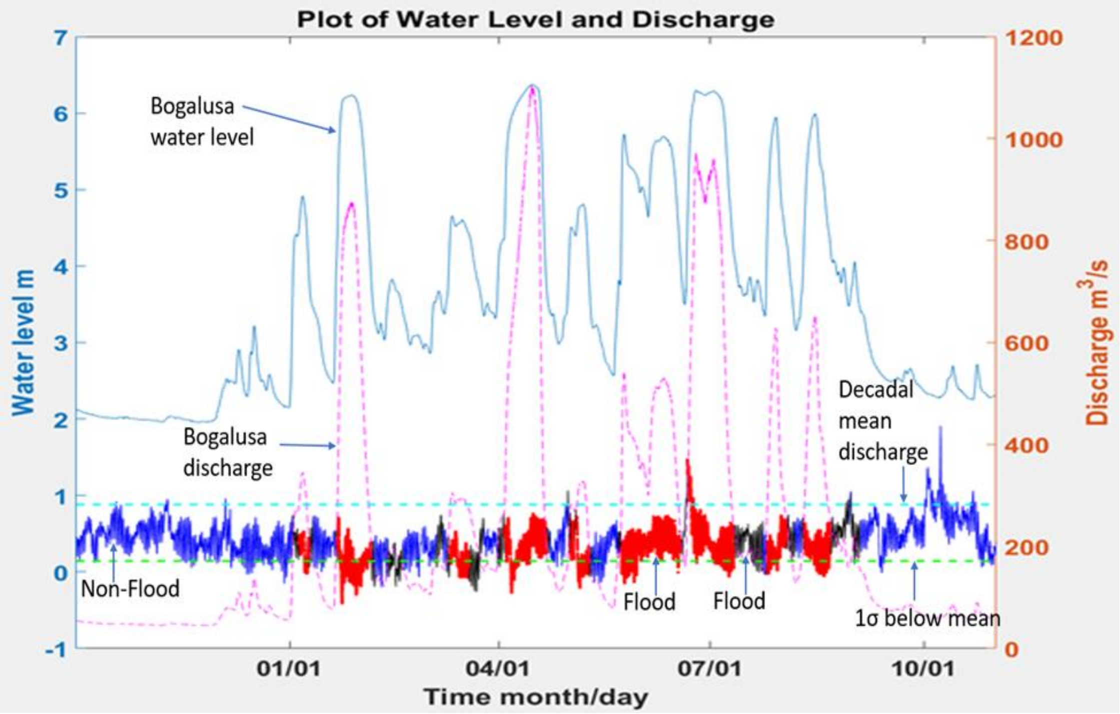

Figure 2.6 *Average annual mean discharge (from 1939 to 2017) and discharge (from October 1, 2016 to October 31, 2017) at Bogalusa and sea levels (from October 1, 2016 to October 31, 2017) at both Bogalusa and CSX Railroad.*

Table 2.4 *Flood periods at CSX Railroad station*

Flood Periods	
Start	Stop
1/5/2017 0:00	1/9/2017 7:30
1/21/2017 14:30	2/4/2017 23:00
3/11/2017 6:00	3/19/2017 3:00
4/3/2017 14:00	4/21/2017 12:00
5/2/2017 3:30	5/3/2017 9:30
5/4/2017 17:00	5/9/2017 18:30
5/23/2017 20:00	6/18/2017 9:30
6/21/2017 6:00	7/11/2017 6:30
7/25/2017 16:00	8/2/2017 22:30
8/10/2017 16:30	8/21/2017 18:00

Table 2.5 *Tidal datums considering cases 1, 2 and 3 at CSX RR station relative to station datum.*

Transferred Datum at CSX RR			
Datum	CSX all data (m)	CSX w/o flood (below decadal mean discharge at Bogalusa) (m)	CSX w/o flood (below @ -1 sigma of decadal mean discharge at Bogalusa) (m))
DTL	0.31±0.03	0.23 ± 0.03	0.24 ± 0.03
Gt	0.66±0.03	0.43 ± 0.03	0.42 ± 0.03
MLLW	-0.02±0.03	0.02 ± 0.03	0.02 ± 0.03
MHHW	0.64±0.03	0.45 ± 0.03	0.45 ± 0.03

The results of the uncertainty analyses and validity check of the USM tidal datum transfer software are shown in tables 2.6 and 2.7 respectively. This uncertainty analysis is more of a check on the precision of the tidal datum transfer, as we do not know the uncertainty of the USGS provided offset between the reference mark and the sea level gauge zero. Saur and Turnipseed (2020) however, indicated that this uncertainty should be part of the sea level uncertainty budget that is required to be below 0.003 m. Table 2.6 shows the mean and standard deviations of the tidal datums with respect to the gauge datum conducted using monthly sea level time series at CSX RR and the Rigolets. It also shows the estimated tidal datums using the entire sea level time series in the case of the Rigolets station and sea level time series data that had been mitigated for the influence of flooding conditions in the case of the CSX RR station. CSX RR standard deviations were higher when compared to those of the Rigolets. Based on table 2.6, it is obvious that the uncertainty in the USM software fall within Swanson (1974) uncertainty budget of 0.03 m using one-year time series for the Gulf coast. This was further confirmed as the results of the tidal datum transfer with respect to the gauge datum using the USM software and NOAA online tidal datum calculator (table 2.7) were compared for the Delacroix station. Sea level time series for two different years (2016 and 2017) but the same period (January 2 to April 3) were used to generate the results for the online tidal datum calculator. There results had no uncertainties, hence, the adoption of the standard deviation of the corresponding datums as the uncertainty estimates for the results of the NOAA online datum calculator. As such, the actual uncertainties in the NOAA online tidal datum results could be higher or lower than the uncertainty estimates. Table 2.7 shows that all the tidal datums but MLLW were within Swanson (1974) uncertainty budget for three-months sea level data. Hence, Swanson (1974) uncertainties were adopted for tidal datums estimated using the USM software.

Table 2.6 *Averages of month-by-month datum transfers, the standard deviation of the result and the final datum transfer result using 286 days of data at CSX Railroad and 395 days of data at the Rigolets. Values are relative to station datum. For reference, Swanson (1974) gives uncertainties of ±0.0548 and ±0.0274 m for tidal datum transfers of 1 month and 1 year, respectively in the Gulf of Mexico.*

CSX Railroad Uncertainty Analysis with respect to gage datum				Rigolets Uncertainty analysis with respect to gage datum		
Datums	Mean of 1-month datum transfers (m)	Std of 1-month datum transfer (m)	1 Yr datum transfer (m)	Mean of 1-month datum transfers (m)	Std of 1-month datum transfer (m)	1 Yr datum transfer (m)
DTL	0.22	0.04	0.23±0.03	0.34	0.03	0.33±0.03
Gt	0.43	0.01	0.43±0.03	0.22	0.01	0.22±0.03
MLLW	0.00	0.04	0.02±0.03	0.23	0.03	0.22±0.03
MHHW	0.43	0.05	0.45±0.03	0.44	0.03	0.44±0.03

Table 2.7 *Comparison of datums between USM in-house software and NOAA online datum transfer tool at Delacroix.*

Comparison of datum transfer results			
Datum	USM 2017	NOAA 2017	NOAA 2016
DTL	1.49±0.05	1.45±0.02	1.43±0.02
MLLW	1.37±0.05	1.32±0.01	1.33±0.01
MHHW	1.61±-0.05	1.58±0.04	1.54±0.04
Gt	0.23±0.05	0.26±0.05	0.21±0.05

In the case of the Chandeleur East buoy, the tidal datums were already with respect to the ellipsoid as the sea level data used for tidal datum transfers were with respect to ellipsoid (Table 2.8). Furthermore, VDatum values for the corresponding tidal datums at the Chandeleur East buoy are also shown in Table 2.8.

Table 2.8 *Comparisons of tidal datums from VDatum and USM in-house software transferred datums at the Chandeleur buoy. Datums relative to NAD83(2011) ellipsoid.*

Datum	Chandeleur East buoy (m)	NOAA Vdatum (m)
DTL	-23.63 ± 0.06	-24.03 ± 0.17
MLLW	-23.81 ± 0.06	-24.22 ± 0.17
MHHW	-23.45 ± 0.06	-23.83 ± 0.17
GT	0.36 ± 0.06	0.39 ± 0.17

Discrepancies between VDatum values and the USM estimated tidal datums for all stations (Tables 2.3 and 2.7) are shown in Table 2.9. Table 2.10 shows the variations in the Great Diurnal tide range using the stations that were investigated in addition to other NOAA tide stations.

Table 2.9 *Differences in the vertical separations between tidal datums and NAD83(2011) ellipsoid obtained at the various stations using the USM software and VDatum.*

All values in m	Rigolets	CSX RR	Delacroix	Chandeleur east buoy
Datum relative to NAD83 (2011)	VDATUM minus USM (m)	VDATUM minus USM (m)	VDATUM minus USM (m)	VDATUM minus USM (m)
MHHW	0.17 ± 0.17	0.16 ± 0.17	0.30 ± 0.18	-0.38 ± 0.18
Dtl	0.16 ± 0.17	0.16 ± 0.17	0.19 ± 0.18	-0.40 ± 0.18
MLLW	0.15 ± 0.17	0.15 ± 0.17	0.08 ± 0.18	-0.41 ± 0.18

Table 2.10 *Comparison of great diurnal ranges at primary (published by NOAA on the websites of individual primary stations) and secondary (determined by USM) stations to VDatum results.*

Great Diurnal Range														
Stn.	Shell Beach NOAA		Waveland NOAA		CSX RR USGS		The Rigolets USGS		Delacroix		Pilot Station East NOAA		Pilot Town NOAA	
	Vdatum (m)	SBCH (m)	Vdatum (m)	BW (m)	Vdatum (m)	USM (m)	Vdatum (m)	USM (m)	Vdatum (m)	USM (m)	VDatum (m)	PSE (m)	VDatum (m)	PT (m)
Values	0.464	0.447	0.523	0.539	0.439	0.430	0.241	0.22	0.459	0.23	0.374	0.36	0.313	0.26
Diff.	0.017		-0.016		0.009		0.021		0.229		0.014		0.053	

2.4 Discussion

In comparing the tidal datum to ellipsoidal vertical separations from the GPS surveys and tidal datums transfers at the USGS stations and the tidal datum transfer at the HydroLevel buoy with the values given by VDatum, two diagnostics are useful for determining the source of the differences. Gt gives an indication of whether the model is exhibiting a good fidelity to the tidal variations and DTL gives an indication of whether the TSS has errors. Although DTL and MSL are not the same, an offset in MSL will affect DTL.

The VDatum ellipsoid–tidal datum separation values at the CSX RR and the Rigolets agreed with those found in this study (Table 2.9), within the published ±0.17 m uncertainties for VDatum and the uncertainties for the same quantities found in this study. The Vdatum ellipsoid-tidal datum separations (Table 2.3) were consistently smaller than those found in this study.

At Delcroix the MLLW value agreed with VDatum within the uncertainties, but the other tidal datums showed larger discrepancies (Tables 2.9 and 2.10). The Gt from VDatum at Delcroix was about 0.23 m larger than from the results of this study. That indicates that the model is either not tuned properly, or the bathymetry and/or coastline is incorrect in that geomorphologically complex region. The VDatum Gt (computed from subtracting NAD83 referenced MLLW from NAD83 referenced MHHW) is closer in value to that at Shell Beach, which is the closest NWLON station in straight line distance, than those further south in the delta. Furthermore, DTL from VDatum at the same station was 0.19 m off from our result. This indicates errors in the VDatum TSS. Like at the

Rigolets and CSX RR, the VDatum values of the estimated datums were also consistently closer to the ellipsoid than for those found in this study.

At the HydroLevel Buoy the Gt is only 3 cm different from what VDatum gives (Table 2.8), but DTL is 40 cm different (Table 2.9). Note that at this location the VDatum tidal datum ellipsoidal heights are further away from the ellipsoid than those found in this study. That is the opposite in sign to what was found at the coastal USGS sites. The Gt diagnostic indicates the tidal model is working well in this region, and the DTL diagnostic indicates a problem with the TSS.

Although the USGS coastal sea level gauges are not meant to provide the climate-quality sea level tidal data that the NOAA NWLON gauges do, any long term instability (e.g., subsidence) is mitigated by conducting geodetic surveys and tidal datum transfers over shorter periods of time, like in this study. They provide snapshots of gauge zero ellipsoid heights and tidal datums from gauge zero, which combine to give tidal datums to the ellipsoid that will remain correct even if subsidence occurs, as long as the subsidence and changing coastline do not affect the tidal characteristics. In regions of active subsidence, these resources are arguably more important for constructing VDatum than benchmarks with published tidal datums from tide gauges removed years ago where more recent GPS surveys were done to obtain geodetic coordinates. They also provide an independent set of observations that can be used to validate VDatum with only the cost of performing a GPS geodetic survey and a tidal datum transfer.

Finally, using the NAVD88 elevations from station datums provided to us by the USGS, we are able to get a measure of the subsidence of the USGS stations. The NAVD88 elevations were obtained from either the GEOID03 or GEOID09 models, indicating that a geodetic survey was performed. By adding the GEOID 12B values back to the NAVD88 elevations (having converted the provided offset to GEOID 12B from GEOID09 in the case of Rigolets station) to gauge zero we recover the ellipsoid heights of the USGS stations at the time the geodetic surveys were performed by USGS. We can then compare those to the ones we obtained to determine the amount of subsequent subsidence, if any. Table 2.2 shows this comparison. At the CSX RR, the subsidence is –0.08 m and larger than the uncertainties. On 3 June 2015, the USGS determined that the gauge datum was 0.10 m below NAVD88 and in March 2018 the gauge datum was found to be 0.18 m below NAVD88 (see Table 2.3). That is a subsidence rate of -0.033 m per year. At the Rigolets the change in elevation (+0.01 m) is less than the uncertainties. At Delcroix, however, the subsidence is -0.22 m, and the uncertainty is ±0.04 m. The -0.22 m subsidence occurred from 1 June 2016, when the USGS surveyed the station to mid-July 2018, when it was resurveyed for this study. The subsidence rate over this period is –0.104 m per year. Jankowski Törnqvist, and Fernandes (2017) determined rates of subsidence rate of 0.000 to -0.061 m per year. The rate at the CSX RR is within this range, but that at Delacroix is higher.

CHAPTER III – SUBINERTIAL ANOMALIES IN SEA LEVEL ESTIMATED USING HIGH FREQUENCY RADAR SURFACE CURRENT DATA IN THE MISSISSIPPI BIGHT

3.1 Introduction

To a first order approximation, there is a geostrophic flow in the ocean interior where Rossby and Ekman numbers are assumed to be small. The barotropic component of this flow results from the balance between the horizontal components of the Coriolis and pressure gradient forces where pressure gradients result from gradient in sea level (Cushman-Roisin & Beckers, 2012). Typically, the subinertial (defined here as timescales greater than 2-days) sea level gradient in the open ocean can be attributed to currents in accordance with geostrophic balance. However, the dominance of the geostrophic balance becomes less certain on continental shelves (Lentz & Fewings, 2012). This is partly due to the varying bathymetry and stratification, both of which can contribute to the separation or overlap of the surface and bottom boundary layers (Lentz & Fewings, 2012), as well as the prevalence of high frequency non-linear processes (e.g. surface gravity waves; Woodworth et al., 2019). These changes in ocean dynamics complicates continental shelf processes (Brian Dzwonkowski & Park, 2012). As such, in addition to geostrophic sea level gradient, ageostrophic dynamics can contribute to subinertial sea level gradient on the shelf.

The contributions of physical processes to gradients in sea level are different for different temporal and spatial scales. Many sea level studies have focused on temporal anomalies, but spatial gradients in sea level have been challenging to observe on the shelf, since altimeters have sparse spatial coverage and require special processing on the shelf. Studies of both temporal and spatial sea level gradients can be useful in understanding of the roles of physical processes to sea level gradients (Woodworth et al., 2019). Particularly, in the Mississippi Bight (MSB; Fig. 3.1) of the Northern Gulf of Mexico shelf (nGOMs), such studies have been limited; (MSB extends from the shoreline to the shelf break).

Previous studies in the MSB have focused more on shelf circulation, resulting in only a few studies on sea level gradients. Ohlmann et al., (2001) used satellite altimetry data to investigate mean flows on the shelf rise area of the GOM and determined that the contribution of eddy-generated vorticity flux to mean flow competes with the contributions of wind stress curl. Though they estimated sea level gradients due to eddies, these results were generally at the outer edge of the shelf. On seasonal timescales, Dzwonkowski and Park (2010) using depth integrated velocities from a single moored Acoustic Doppler Current Profiler (ADCP) at the 20 m isobaths offshore of Mobile Bay, observed an eastward flow in the late spring/early summer, which they suspected resulted from a barotropic pressure gradient and westward flow in the late fall/early winter, which resulted from the wind driven current. While at synoptic timescales (i.e. days to weeks), Dzwonkowski & Park (2012) observed a relationship in the variability of coastal sea level and variability of wind as it transitions back and forth between upwelling favorable and downwelling favorable. However, their study was limited to coastal sea level measurements with no consideration of the sea level over the broader shelf.

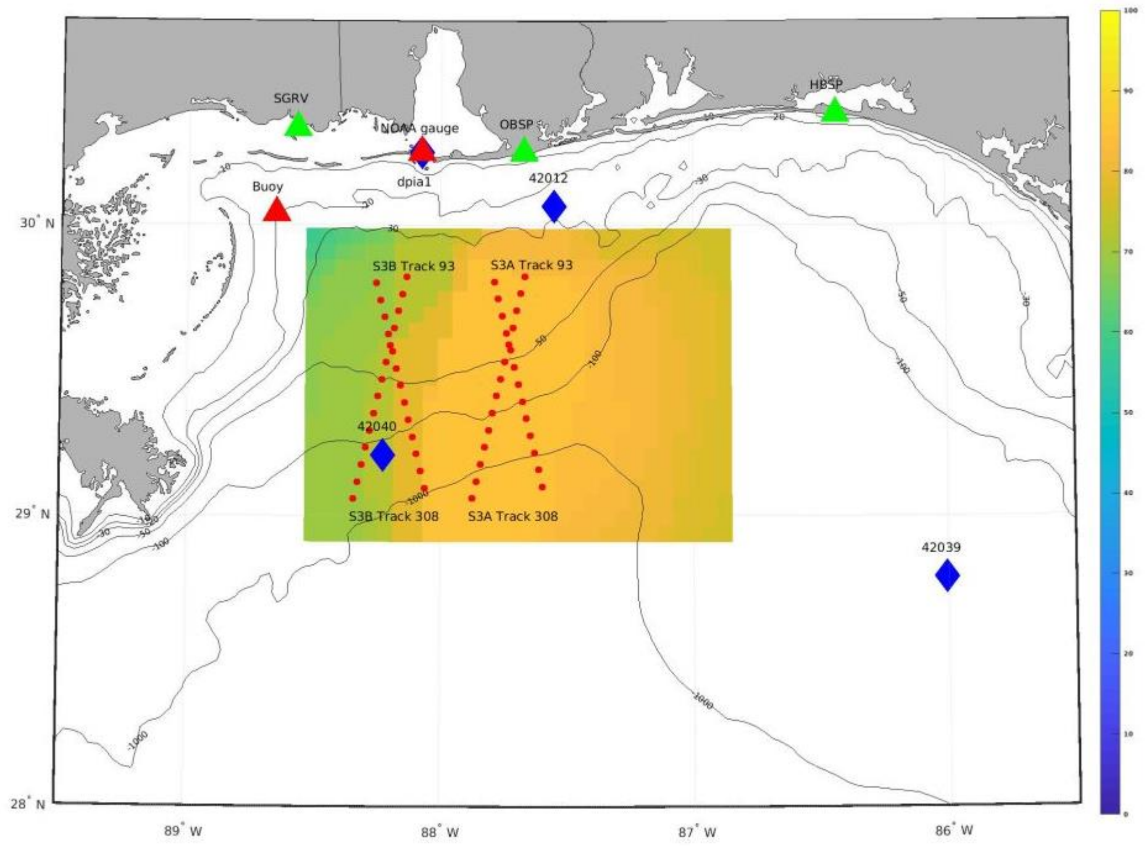

Figure 3.1 *Map of the study region with surface current coverage domain showing percentage of HFR data availability. The blue diamonds represent the locations of wind stations; starting from the northmost and moving in the clockwise direction dpia1 (in a similar location with the northmost red triangle), 42012, 42039 and 42040. The ~5 MHz HFR stations locations are represented by green triangles; starting from the leftmost Singing River Island in Mississippi, Orange Beach in Alabama and Henderson Beach State Park in Florida. Red triangles represent the locations of the sea level stations: coastal gauge (NOAA 8735180 Dauphin Island) and offshore buoy. The first X-crossing is S3B pass 93 and 308 while the second X-crossing is S3A pass 93 and 308.*

Several techniques are available for sea level measurements, each with their own strengths and weaknesses. In coastal regions, sea level is measured using a variety of instrumentation, most of which measure sea level relative to land. These instruments are installed on relatively stable platforms like piers. However, they provide measurements mostly near-shore, at single points and are not evenly distributed. Offshore sea level can be measured using bottom-mounted pressure sensors (with a correction for atmospheric pressure) and/or GNSS installed on buoys (Bisnath et al., 2004; Nwankwo et al., 2019). Sea level observations utilizing GNSS receivers on buoys can be approximated to be from a single point like in coastal tide gauges and staffs and provide absolute (e.g. geodetic) sea level measurements. Though sea level observations from tide gauges and buoys are for single points, they usually provide time series at high temporal resolutions.

Coastal and offshore sea level heights and anomalies can also be estimated from satellite altimetry data and numerical model outputs. Along-track Jason and Topex/Poseidon data are at 7 km intervals, having maximum track spacing of about 300 km and temporal resolution of 10-days. Along-track satellite altimetry data are interpolated to generate sea level data on a regular spatial grid (Ohlmann et al., 2001). In the case of gridded altimetry data, the spatial resolutions are large (Chavanne and Klein, 2010) for instance, 30 km × 30 km (Roesler et al., 2013).

Though satellite altimeters are able to provide estimates of wide areas of absolute sea level (at poor temporal and spatial resolutions), they perform poorly during heavy-rain events (>12 mm hr-1), under low and complex winds and in the presence of surface slicks patches due to calm surfaces (Quartly et al., 1998; Tournadre et al., 2006; Roesler et al., 2013). Chelton et al., (2001) enumerated various drifts and calibrations required for satellite altimetry data. For instance, the measurement system drift is calibrated using tide gauges. Christensen et al. (1994) argued that the drift in satellite altimeter measurements system results from the in-situ tide gauges used in the calibration noting that the tide gauges are vulnerable to subsidence or uplift due to isostatic rebound. Chelton et al., (2001) proposed the use of Global Positioning System (GPS) buoys for calibrating the altimeter measurement system. However, the technique requires the deployment of several GPS buoys along the tracks of the altimeters. Additionally, the integrity of the geophysical corrections applied to altimeter data degrades in the shelf region because shoaling of bathymetry induces more variability in physical processes such as tides (Andersen & Scharroo, 2011). Furthermore, satellite altimeter waveforms are not reliable when the foot print of satellite altimeter such as Jason-2 is closer than 25 km to the coast (Roesler et al., 2013). Rudnick et al., (2014) noted that numerical models such as the Princeton Ocean Model assimilates sea level data from satellite altimetry data. As such, coastal sea level outputs from such models could be degraded when poor quality satellite altimeter data are assimilated. Therefore, there is need for adequate in-situ sea level data on the continental shelf and coastal regions.

A potential alternative to satellite altimetry based measurement of sea level anomalies over shelf regions is using sea level estimates based on currents derived from high frequency radar (HFR). Differential sea level anomalies can be estimated using surface currents data derived from HFR but they do not have an absolute reference like in satellite altimetry. Roesler et al., (2013) used such a method to investigate the validity of different satellite altimetry retrackers (models used to determine the offset of echoes in order to estimate satellite range above the sea surface) close to the coast of California. The same method was also used by Chavanne and Klein (2010) to confirm that sub-mesoscale processes were present in satellite altimetry along-track data.

Given the successes of these previous studies in using HFR to estimate sea level anomalies as well as the limited scope of the previous circulation studies in this region, this paper, seeks to improve the understanding of the subinertial sea level anomalies on the shelf of the MBS. In this context, without an ability to absolutely reference sea level derived from surface velocities, anomalies are computed at each observation time from the spatial averaged derived sea level. Note that from one observation time to another the anomalies are, in general, with respect to a different mean value. This is the first study to use HFR to conduct a large-scale sea level anomalies analysis in the MSB. While the idea of using HFR surface current data to estimate sea level anomalies is not new, a novel technique involving the Least Squares adjustment was adopted in estimating the anomalies in sea level. Diagnostic analysis of the terms in the momentum equation was conducted to investigate if the subinertial MSB sea level anomalies were mainly due to geostrophically balanced currents. Dominant modes in the estimated subinertial sea level anomalies were analyzed using empirical orthogonal functions. Subinertial sea level anomalies are hereinafter referred to as sea level anomalies. Details of the data used and the various data processing techniques applied are discussed in section 2. In section 3, diagnostics of the terms in the momentum equation are presented. Sea level anomalies determined from other sources (coastal sea level gauges, offshore buoy and satellite altimeter) are used to compare to the sea level anomalies estimated using HFR data in section 4. Analysis of EOF modes in the sea level anomalies estimated using HFR data are presented in section 5. In section 6, the results of the analysis are discussed and conclusions from the study are summarized in section 7.

3.2 Data and Data Processing

3.2.1 High Frequency Radar Data

In general, HFR systems are broadly divided based on the antenna configuration (direction finding and phase-array) and the processes involved in estimating surface currents using both systems are similar and were discussed in Paduan & Graber (1997). Summarily, it involves the transmission of vertically polarized high frequency radio signal, backscatter of the signal by Bragg waves (waves satisfying the Bragg condition: wavelengths are half the wavelength of the transmitted signal) and reception of the signals backscattered towards the antenna. The system then estimates range to the scattering waves, bearing of the received signals, signal-to-noise ratio of the signals and Doppler shift (Teague et al., 1997). The estimated Doppler shift corresponds to the Doppler Effect due to the ambient ocean currents and Bragg waves. By eliminating the Doppler Effect due to the Bragg waves, known from the deep water wave dispersion relation, the remainder of the Doppler shift is due to the ambient ocean currents. The remaining Doppler shift is multiplied by the wavelength of the Bragg wave resulting in radial surface currents towards or away from the radar. The effective water column depth of the estimated radial surface currents depends on the wavelength of the HFR signal (Stewart & Joy, 1974) and the current profile below the surface. Because a single HFR only gives information on the component of currents moving towards or away from a given range cell (‘radials’), the total velocities of the surface current are determined by combining the estimated radial currents at angular intersection greater than 30^o but less than 150^o from at least two neighbouring HFR stations (Paduan & Graber, 1997).

The Central Gulf of Mexico Ocean Observing System (CenGOOS) at the University of Southern Mississippi (USM) is a part of the Gulf of Mexico Coastal Ocean Observing System (GCOOS). CenGOOS uses CODAR Seasonde systems which are long (5MHz) and short (25 MHz) range HFRs in the northern Gulf of Mexico. The emphasis of this study is the domain covered by the long range HFR having 1-hour temporal resolution and a spatial resolution of ~ 6 km (Fig. 3.1).

The radial data generated from these long range HFR stations corresponds to currents of the surface water column of an effective depth of ~2 m; however, there are data gaps for various reasons. For example, if tropical storm force winds are forecasted to strike a station within 72 hours, the station is removed and this disrupts surface current observation as noted in Nwankwo et al. (2020) for the analysis of Hurricane Nate. Furthermore, calm seas have few waves to backscatter transmitted signals (Liu et al., 2010). System malfunctions at the HFR stations also disrupts observations and there are limited number of stations in the MSB as shown in (Fig. 3.1). Some of these issues can be significantly reduced by having redundant HFR stations as found on the California shelf (Roesler et al., 2013). Despite the limitations of the HFR network in the MSB, extensive data has been collected over the MSB region.

Surface velocity vectors are generated using the estimated surface current radials. This process was conducted using the MATLAB programs (hfrprogs toolbox) available from the Radio Operators Working Group (ROWG). Various efforts have been made to quality control the data associated with this network. Velocity uncertainties included the Geometric Dilution of Precision (GDOP) are computed from the angle of intersection of surface current radials used to estimate total surface current vectors. While Hode (2019) eliminated velocity data whose uncertainties that were greater than 0.05 m/s, this constraint was relaxed depending on the situation as velocities whose uncertainties that were less than 0.2 m/s were accepted for hurricane periods. Using a 0.05 m/s constraint resulted in prohibitively large data gaps. As a result of this, 0.1 m/s constraint was adopted as a trade-off between accuracy and data availability. It should be noted that this was still a conservative choice as higher HFR data uncertainties have been reported in other studies (Chapman & Graber, 1997; Yoshikawa et al., 2006). After evaluating the data over the life time of the network, the period of February 1, 2016 to November 30, 2019 was selected for the analyses in this study.

3.2.1.1 Interpolation of Gaps in the HF radar Surface Current Data

Surface current data availability varied with space and time. Figure 3.1 showed that the percentage of the surface current data was highest in the mid-region of the three HFR stations as it is the region where the signals from the three HFR stations had a 100% overlap. However, the percentage of data availability declined away from this region due to lack of redundancy in HFR coverage. In cases where data were available in at least three data points that are one grid step in space and time from a missing data point, nearest neighbour averaging interpolation technique was used to fill the missing data point. Other data gaps were interpolated using a Gauss-Markov estimator (Appendix section A) which is a statistical technique similar to the interpolation technique applied in Cho et al., (1998). However, in cases of insufficient data or lack of data around a data gap to build an adequate statistic, the data gap interpolations were ignored. Insufficiency or lack of data was mostly due to system removal or malfunction.

3.2.1.2 Time Averaging and Power Spectra (temporal spectral analysis)

An adequate filtering technique was required to extract the subinertial components from the surface currents. A second order Butterworth filter, which eliminates phases shift by filtering in the forward and backward directions, was adopted.

Considering the presence of data gaps, the filter was applied to only available data that were continuous in time intervals.

The decision on the temporal averaging period was dependent on the near-inertial frequency of the MSB as well as spatial scales. Processes whose spatial scales are smaller than the internal Rossby Radius of Deformation (RRD) in the MSB and at the same time have frequencies which are higher than the MSB inertial frequency are not influenced by the Coriolis force (Cushman-Roisin & Beckers 2012). Cushman-Roisin & Beckers (2012) suggested that in estimating temporal averages, the averaging period should be at least over the period of the processes, which are not of interest, adequate enough for obtaining statistical mean but short so that the evolution of the processes of interest should be captured. A cut-off period of two days was adopted to low-pass filter the surface currents on all the grid points resulting in the low frequency subinertial surface currents (Chavanne & Klein 2010; Liu & Weisberg, 2007). This thereby eliminates high frequency processes like semidiurnal and diurnal tides and inertial motions as noted by Roesler et al., (2013).

Spectral analysis was conducted to investigate the efficacy of the Butterworth filter in reducing high frequency energies. Figure 3.2 displays the spatially averaged total spectral computed from ~50% of the velocity grid points corresponding to continuous data availability in both the raw and filtered data spanning from 10 October 2016 to 10 December 2016. The time frame was chosen because it was the longest window of continuous data in time. The reported frequencies are from the first frequency bin to the Nyquist frequency bin. The zeroth frequency bin was not present because the time mean was removed in the pre-whitening process. The spectra show that the filter mitigates the energies of high frequency signals while preserving the energies in low frequency signals; observe the divergence in the raw and filtered spectral at scales less than the subinertial scale.

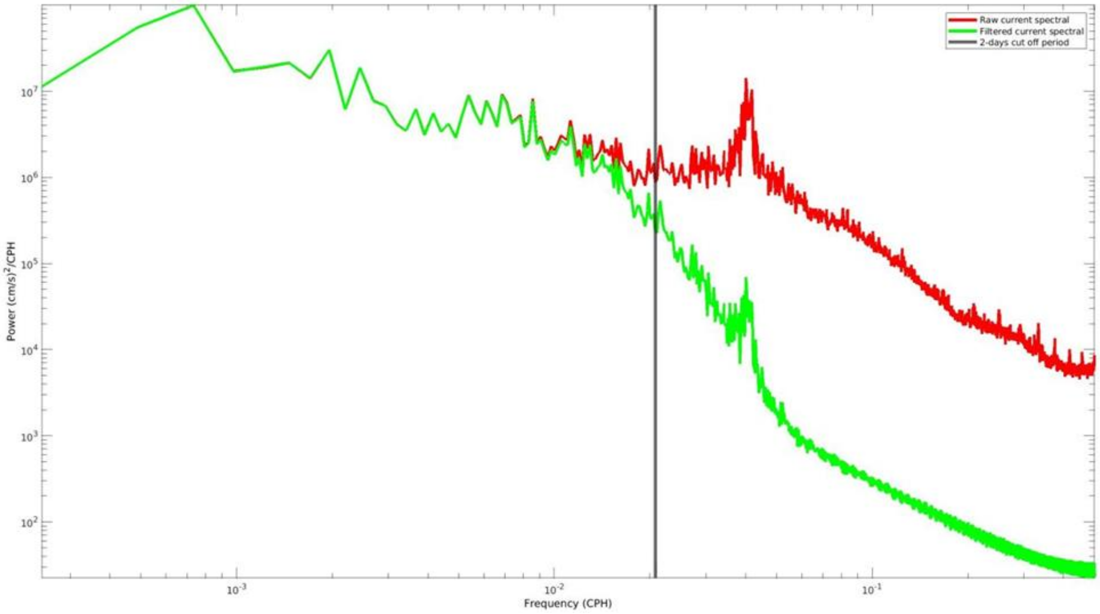

Figure 3.2 *Spatial mean of the total spectral of raw and subinertial surface currents. The vertical line marks the subinertial frequency.*

3.2.2 Satellite Altimeter Data

Sentinel 3A (S3A) and 3B (S3B) along-track sea surface height anomaly (SSHA) data were used in this study. The following corrections had been applied to the datasets: long wavelength error, ocean tide and dynamic atmospheric forcing (Mertz et al., 2017). S3A along-track data that were investigated spanned from February 2016 – November 2019 while S3B along-track data spanned a shorter period from December 2018 – November 2019 given that the S3B satellite was launched two years (2018) after the launching of S3A satellite. The SSHA from the S3 along-track data was used because it has a better spatial resolution (~7 km) compared to the gridded satellite altimeter products. Unlike other satellite altimeter missions such as Topex/Poseidon and Jason, S3 estimates sea surface height in the synthetic aperture radar mode and it provides more reliable results in coastal regions (Bonnefond et al., 2018). Tracks 93 and 308 of the orbits of both S3 satellites pass the HFR domain in the north-south orientation (Fig. 3.1) each with a repeat period of 27 days thereby ensuring at least monthly data availability over the HFR domain for each track. Both tracks (93 and 308) have an interval of 7 days and track 93 of S3A lags track 93 of S3B by 17 days as well as for track 308.

3.2.3 Sea level Data

In addition to along-track SSHA information, coastal and offshore sea level data were analyzed. The coastal station used in this study was the NOAA NWLON gauge (8735180) at Dauphin Island, Alabama. The sea level sampling data interval at the gauge is 6 minutes. Sea level data, downloaded from the coastal station was with respect to the station gauge zero. In addition to the sea level data, atmospheric pressure data were also downloaded from the station. Unlike in the sea level data, there were several months of data gaps in the atmospheric pressure data. Some of the data gaps were filled with data from a nearby meteorological station (8734673) at National Data Buoy Center (NDBC) Fort Morgan, Alabama. Both the coastal sea level and air pressure data were filtered in the same manner as the HFR data. The resulting subinertial sea level data was corrected for inverted barometric effect using the filtered air pressure and adopting the formula in Pugh & Philip (2014).

Offshore sea level data was from a buoy deployed by USM at the 20 m isobath on the Mississippi shelf. Several sensors were installed on the buoy and they include but are not limited to a Trimble NetRS GNSS receiver and antenna. Sensors on the buoy were operational until the storm surge from Hurricane Nate which negatively affected the sensors resulting to loss of data. However, the GNSS sensor survived the hurricane and remained operational until the buoy was retrieved. Sea level data obtained using the ellipsoidal height from the GNSS antenna were referenced to the North American Datum 1983, National Adjustment 2011 (NAD83(2011)). The data had been used to estimate the storm surge at the buoy location in comparison to that at a coastal sea level gauge (Nwankwo et al., 2020). Hence, the buoy data was considered viable in estimating MSB sea level anomalies. It was filtered and corrected for inverted barometric effect as in the case of the coastal sea level data using the atmospheric pressure data measured at the NOAA station 8735180 at Dauphin Island. Considering that the sea level from the coastal and buoy stations had different references, the temporal means of the individual subinertial sea level were subtracted from each corresponding subinertial sea level to estimate anomalies similar to Rudnick et al. (2014).

3.2.4 Wind Data

Given that wind influences the currents in the MSB, local wind data of the same time period as the surface current data were analyzed. There were inconsistences in wind data sampling intervals on the various stations; at some stations (dpia1h and 42039) the wind data were at 1-hour intervals while at the other stations (42012h and 42040h), the data were at 1-hour intervals in some periods and at 10-minutes intervals in other periods. At the stations where the wind data were at 10-minute intervals, they were subsampled to 1-hour intervals by averaging 1-hour data about the hour mark. An optimal wind data was estimated using the various wind data (Appendix Section B). Gaps in the optimal wind were interpolated using a method similar to (Dzwonkowski et al., 2009; Liu & Weisberg, 2007).

3.3 Momentum Equation Terms Diagnostics

The momentum equations are used to diagnose ocean dynamics. Magnitudes of the terms in the equations can vary depending on the temporal and spatial scales of processes under consideration. Through the diagnostics of the terms in the momentum equation, the relative significance of the individual terms in the equations is estimated. For this study, the data available for the diagnostics of the terms includes the subinertial surface current velocities and the corresponding velocity anomalies as well as the wind data. The invariant form of Reynolds' averaged momentum equation Eqn. (1) was adopted (see Madec et al., (1998) and Ohlmann et al., (2001) for the respective invariant form and invariant form of Reynolds' averaged momentum equations) to investigate the contribution of different terms to subinertial sea level:

$$\frac{\partial \bar{\mathbf{u}}}{\partial t} + \left(\bar{\xi} + f\right)\hat{\mathbf{k}} \times \bar{\mathbf{u}} + \hat{\mathbf{k}} \times \left(\overline{\xi' \mathbf{u}'}\right) = -\nabla\left(g\,\bar{\eta} + \frac{1}{2}\,\overline{\mathbf{u}'.\mathbf{u}'} + \frac{1}{2}\,\bar{\mathbf{u}}\,.\,\bar{\mathbf{u}}\right) + \frac{\partial \sigma}{\partial z} \qquad \text{Eqn. 1}$$

where $\bar{\mathbf{u}}$ corresponds to the horizontal velocity of subinertial surface currents, $\mathbf{u}'$is horizontal perturbation velocity estimated from the differences between the velocity of the unfiltered and subinertial surface currents (based on the assumption that the 2-day filtering obeys the Reynolds axioms), $\bar{\xi}$ is the vertical component of relative vorticity estimated using the subinertial currents, ξ' is perturbation of the vertical component of relative vorticity estimated using the perturbation velocity, f is the Coriolis parameter, $\bar{\eta}$ is subinertial sea level anomalies, g is gravity acceleration, $\frac{\partial \sigma}{\partial z}$ is the most important part of the divergence of turbulent viscous stresses in the upper boundary layer which is approximated as wind stresses (kinematic, with units $\frac{m^2}{s^2}$ and referred to τ_x and τ_y for the x and y momentum equations respectively) divided by the boundary layer depth estimate d,

$\hat{\mathbf{k}}$ is the vertical unit vector and × denotes the vector (cross) product. Hereinafter x and y momentum equations will be referred to as along-shelf and across-shelf momentum equations respectively and they correspond to the east-west and north-south orientations respectively using similar conventions as Dzwonkowski & Park, (2012). The other assumptions made in (Eqn. 1) are: f-plane, Boussinesq and Hydrostatic approximations. Under the hydrostatic approximation, the baroclinic effect enters the momentum equations in the horizontal component of momentum via horizontal pressure gradient. Since the equations are written for very thin upper layer of the ocean the effects of density anomaly on pressure are negligible. There was no separation of the flow into barotropic and baroclinic components. Similar approach was adopted in Chavanne and Klein, (2010) to estimate sea level changes. Additionally, as it is commonly assumed in boundary layer consideration (Bretherton, 2002), the terms representing divergence of the Reynolds fluxes accounted only for the vertical shear of horizontal velocity. Terms with overbars involving the product of perturbations were filtered using the same technique as the filtering of the surface currents. In this invariant form of the momentum equation, advection of momentum is replaced by the sum of the vector product of z-component of relative vorticity (ξ) and velocity and the gradient of kinetic energy.

Besides the sea level gradient term, each term in Eqn. (1) can be estimated with the available data. Using the subinertial surface currents, the time derivative, mean vertical component of relative vorticity and gradient of mean kinetic energy terms were computed. The perturbation of the vertical component of relative vorticity and kinetic energy of perturbation were computed using the residual in the difference between the original and subinertial surface currents. The wind data was used to estimate wind stress at the surface using Large & Pond (1981) formula which resulted in kinematic wind stress. In the open ocean the boundary layer depth can be approximated by the thickness of the Ekman layer. However, the Ekman layer as proposed by Ekman in Ekman, (1905) is idealistic as suggested by Cushman-Roisin & Beckers (2012) based on several simplistic assumptions; for instance the assumption of a constant eddy viscosity coefficient in a geophysical flow with vertical shear and the assumption of a homogenous density of the fluid. Monin and Yaglom (1971) proposed an eddy viscosity coefficient for the estimation of the Ekman layer, which is also constant within the boundary layer but the value of the coefficient depends on the kinematics of the fluid property compared to that of Ekman (1905). A different empirical estimate of the Ekman layer that depends on wind was used in this study. With wind as the main source of turbulence in the surface ocean, the vertical length scale of the Ekman layer was parameterized by the scaled turbulence wind mixing layer Eqn. (2) (Stigebbrandt, 1985; Cushman-Roisin & Beckers 2012; Oyarzún & Brierley, 2019).

$$\mathrm{d} = \gamma \frac{\mathrm{u}_*}{\mathrm{f}} \qquad \text{Eqn. 2}$$

where γ is the coefficient of proportionality (0.1), f is Coriolis parameter and $\mathrm{u}_* = \sqrt{|\tau|}$ is the turbulent friction velocity. This parameterization of the Ekman layer does not account for the overlap of both the surface and bottom boundary layers and the effect of stratification. Despite these challenges, this parameterization has been used in other studies. Different values of γ were adopted in previous studies. Modjeld & Lavelle (1984) and Stigebbrandt (1985) suggested the value of γ to be ~ 0.2 while Cushman-Roisin & Beckers (2012) and Oyarzún & Brierley (2019) suggested the value of 0.4. We took a deterministic approach towards the selection of the coefficient γ. The depth of boundary layer decreases due to vertical stratification (Cushman-Roisin & Beckers, 2012) since more wind energy is spent mixing stratified fluid. As such, the boundary layer depth should closely resemble the mixed layer depth. Time series of boundary layer depth were computed for various values of γ. The seasonal cycle of the estimated boundary layer depth was compared to the estimate of the annual variations of the mixed layer depth in (Zavala-Hidalgo et al., 2014) and the value γ at which the boundary layer depth closely resembles the mixed layer depth was determined to be 0.1. When the estimated boundary layer depth exceeds the 0.8 of the bathymetry (e.g. in shallower region), we assume the boundary layer depth to be equal to 0.8 of the bathymetry. The application of the boundary layer depth correction procedure was limited to a region in the inner shelf. The correction procedure was applied in relatively few occasions in time for increased turbulent friction velocity. Despite the exaggeration of the last term in Eqn. (1) that resulted from a lower value (0.1) of γ, the correction procedure is not critical in this study as the term that was approximated was not the leading term in the momentum balance.

The geostrophically balanced dynamics of the subinertial flow in MSB assumes that the leading terms in Eqn. (1) are the Coriolis acceleration and the pressure gradient force due to the slope of the sea level as shown in Eqn. (3):

$$\mathrm{f}\hat{\mathbf{k}} \times \mathbf{u} = -\mathrm{g}\nabla\eta \qquad \text{Eqn. 3}$$

where f is the Coriolis parameter, $\boldsymbol{u}$ is the geostrophic velocity vector, $\nabla\eta$ is the sea level gradient and g is the gravity acceleration. Conventionally, it is assumed that for this balance to hold in the MSB, the Rossby number (R_o) (ratio of relative vorticity and Coriolis parameter Chavanne and Klein, 2010) must be less than 0.1 (Kim, 2010). $R_o <$

0.1, indicating that the Coriolis term in Eqn. (1) is the dominant term given that the advective time scale defines the scale of the time derivative term. Furthermore, the spatial scales of the dominant currents must be greater than the internal RRD. Chelton et al., (1998) while accounting for stratification, earth rotation and water depth estimated the internal RRD for the GOM to be ~40 km while also noting that the RRD varies by < 10 km. Although the spatial scale of the study region is greater than this internal RRD value that did not guarantee that Eqn. (3) adequately represented the dynamics that results in anomalies in sea level in the MSB.

For quantitative analysis of applicability of Eqn. (1) in MSB the terms in Eqn. (1) were evaluated for every internal grid point of the domain. Statistical analysis of each term from the results of the diagnostics was computed over the entire time series. The statistics comprised of the mean and standard deviation values of the individual terms corresponding to the along-shelf and across-shelf momentum equations across the domain (Appendix C: C1-C4). Table 1 was used to summarize these results by representing the statistics of the various terms over the entire time and space.

Table 3.1 *Mean and standard deviation of the along-shelf and across-shelf momentum components computed in time at each grid point and the variability across the HF radar domain of each statistic is given by the corresponding ± standard deviation.*

(Units: 10^{-7} ms^{-2})		
Terms	Mean	Standard deviation
Along-shelf Momentum Components		
$\frac{\partial \overline{u}}{\partial t}$	0.0 ± 0.1	16.5 ± 3.4
$\overline{-\xi}\overline{v}$	-0.0 ± 0.7	7.0 ± 1.7
$-f\overline{v}$	14.3 ± 7.1	66.4 + 4.0
$\overline{-\xi' v'}$	0.5 ± 0.7	5.4 ± 1.2
$\frac{1}{2}\frac{\partial \overline{\boldsymbol{u}'.\boldsymbol{u}'}}{\partial x}$	-0.3 ± 1.2	6.1 ± 2.3
$\frac{1}{2}\frac{\partial \overline{\boldsymbol{u}}.\overline{\boldsymbol{u}}}{\partial x}$	-0.5 ± 1.3	8.4 ± 3.7
$-\frac{\partial \tau_x}{\partial z}$	8.5	34.9
Across-shelf Momentum Components		
$\frac{\partial \overline{v}}{\partial t}$	0.0 ± 0.1	13.2 ± 0.8
$\overline{-\xi}\overline{u}$	1.0 ± 2.0	11.1 ± 4.3
$f\overline{u}$	5.5 ± 16.4	95.2 ± 19.2
$\overline{\xi' u'}$	1.3 ± 1.5	7.2 ± 3.3
$\frac{1}{2}\frac{\partial \overline{\boldsymbol{u}'.\boldsymbol{u}'}}{\partial y}$	-0.7 ± 1.1	6.0 ± 2.2
$\frac{1}{2}\frac{\partial \overline{\boldsymbol{u}}.\overline{\boldsymbol{u}}}{\partial y}$	-0.4 ± 1.3	8.1 ± 3. 0
$-\frac{\partial \tau_y}{\partial z}$	-0.1	34.1

The relative importance of the individual terms in the along-shelf momentum equation were determined from the mean and standard deviation of the terms as shown in (Table 1 and Fig. C1). Absolute values of the mean for individual terms were considered to focus on their magnitudes. The magnitude of the Coriolis term was the greatest and it was also the most variable among the terms, while the magnitude of the time partial derivative term as well as the term involving the mean relative vorticity were the least. The spatial structure of the mean of the Coriolis term (Fig. C1) shows that it becomes smaller towards the shore, which was an indication that the v velocity component reduced towards shore. A similar trend was observed in the time partial derivative term. In the case of the gradient of the mean kinetic energy, there is a distinct spatial trend as peak values were observed in the southern and northeastern regions. These indicated regions of significant low frequency processes. Unlike the gradient of the mean kinetic energy, the spatial structure in the gradient turbulent kinetic energy did not exhibit a clear pattern. Also, the spatial pattern of the mean of the terms involving the mean and turbulent vorticity did not exhibit a clear pattern. Based on the standard deviations of the individual terms, the least and most variable terms are the terms involving the turbulent vorticity and the Coriolis term, respectively. Regions of highest variability for the Coriolis term are the north and southeast. Unlike the Coriolis term, the other terms were most variable in the north-western part of the region.

The structure of the spatial mean and standard deviations of the terms in the across-shelf momentum had some similarities and differences when compared to those from the along-shelf momentum. Similar to the along-shelf momentum equation, the magnitude of the mean Coriolis term was the largest as well as the most variable. Additionally, the gradient of the turbulent kinetic energy term was also the least variable as in the along-shelf momentum equation. Besides the time partial derivative term whose variability also increased towards the southeast, the spatial structure of the standard deviation of all the terms showed that the variability in the terms increased towards the northwest. Unlike the along-shelf momentum equation, the term with the least magnitude was the stress term. Considering the spatial structure of the mean of the terms (Fig. C3), the Coriolis term decreased from the north towards the south of the domain. A similar structure was observed in the time derivative term. The gradient in mean kinetic energy showed an unexpected structure as it decreased from the north and south and towards the center of the domain. The mean of the gradient of the turbulent. kinetic energy showed a different pattern that increased towards the north and southeast regions. Both spatial structures of the terms involving the mean and turbulent vorticity showed that the mean of the terms increased towards the west.

The importance of non-linear terms with respect to the Coriolis terms was further determined from the computation of internal Rossby radius of deformation. R_o was found to be greater than 0.1 in some cases. However, the number of cases (64169 for the along-shelf momentum and 234925 for the across-shelf momentum) for which $R_o > 0.1$ can be considered to be a tiny portion of the total number in space and time (17125919). This implies that the geostrophic balance in Eqn. (3) can be considered as the dominant dynamical balance in MSB for surface velocity.

3.4 Estimates of Sea level and Sea Level Anomalies

A Least Squares adjustment technique was implemented to estimate sea level fields at each observation time, minimizing the squared residual in Eqn. (3). Note that these sea level estimates are indeterminate to a reference level. For a two-dimensional velocity vector field, the u and v components can be rewritten using two scalar functions: stream function and potential, describing the rotational (non-divergent) and potential parts of the velocity field respectively. Sea level estimated using the geostrophic approximation Eqn. (3) corresponded to the non-divergent part of the subinertial surface currents. The reconstructed sea level minimizes the cost function (Eqn. (4)) using a Quasi-Newton with a Limited-Memory Broyden–Fletcher–Goldfarb–Shanno (LBFGS), optimization algorithm

$$J = 0.5\sum W_1(g\nabla\eta + \mathbf{U})^2 + 0.5\sum W_2(\Delta\eta)^2 \qquad \text{Eqn. 4}$$

where J is comprised of two terms: a 'data term', where $g\nabla\eta$ is the finite-difference approximation of the pressure gradient, and $\mathbf{U}$ is the left hand side of Eqn. (3) and a smoothness term, where $\Delta\eta$ is the finite-difference Laplacian of the sea level. The summation goes over all grid points where $\mathbf{U}$ is available for the first term of the cost function and over all grid points where the Laplacian of the sea level is computed. The smoothness term is introduced to penalize grid-scale sea level variations and to produce a smooth interpolation of sea level to the regions where data gaps were present. The data term weight W_1 and the smoothness term weight W_2 are represented by diagonal matrices. The diagonal weight matrices ($W_1$and W_2) in Eqn. (4) were defined using a deterministic procedure. W_1 was initially set to be a unit matrix. Using this matrix, the cost function was evaluated for the flat sea level field and the resulting cost function value with units $(\frac{m}{s^2})^2$ was used to normalize W_1. This normalization did not affect the result of the optimization because the cost function is defined up to an arbitrary multiplicative factor. W_2 was also initialized as a unit matrix scaled with the ratio of the nominal value for the first term of the cost function and the second term of the cost function evaluated for an analytical grid scale oscillating field. As such, the units of W_2 were inverse of the units of the squared Laplacian term which automatically makes the second term of the cost function unitless. This initial scaling did not mitigate small-scale features in the estimated sea level. The optimal weight of the smoothing term was determined by conducting a set of Least Squares experiments with a range of weights of the smoothness term. Real data were used in the experiments. At the end of each experiment, the first and second terms of the cost function were determined. Both the first and second terms of the cost function increased as the weight of W_2 increased. The optimal weight W_2 corresponded to the Least Squares fit where small-scale sea level features were filtered while the increase of the first term of the cost function was less than 10% of the first term of the cost function value for W_2 equal zero.

Over the study period, the spatial variation in the vertical range in the reconstructed sea level anomalies was between 0.01 m – 0.50 m. The minimum spatial range occurred on November 17, 2016 while the maximum spatial range was on October 10, 2018. A spatial range of 0.50 m is not typical for the region as the mean spatial range was estimated to be 0.12 ± 0.06 m, however because of mesoscale features, which sporadically approach the region (e.g. Ohlmann et al., 2001, Plate 4a), larger ranges can occur. Hereafter, we will refer to the reconstructed sea level anomalies as HFR SSHA.

The above Least Squares technique of estimating sea level differ from the Optimal Interpolation technique adopted in Roesler et al., (2013). While the Optimal Interpolation technique is a statistical approach and requires prior knowledge of data and background error covariances, the Least Square technique is a deterministic approach and does not require prior knowledge of the error covariances. Roesler et al., (2013), applied an amplification factor to their optimal interpolation estimated HFR SSHA to correspond to satellite altimeter SSHA. This amplification factor was not required in the HFR SSHA estimated in this study.

Before the application of the Least Squares technique to observed data, the technique was used to reconstruct an analytical sea level field using an analytical velocity field while considering cases of data gaps in the current data. Due to the indeterminacy of the reconstruction sea level to reference level, an anomaly field with respect to the spatial mean was computed for both the reconstructed and analytical sea level fields for comparison. The accuracy of the reconstructed field (norm of the difference between the reconstructed anomalies in sea level and the analytical sea level anomalies) was at the millimeter level when 30% of data gaps were present in the analytical current field. It was much smaller than one millimetre when 0% of data gap was considered.

Sea level was only reconstructed if gaps in the domain were less than 25% of the total data points to ensure that sufficient amount data were available for estimating sea level anomalies across the domain. For all estimated sea level , the spatial mean across the domain was subtracted so that the anomalies had a zero spatial mean.

Uncertainties in the geostrophic HFR SSHA were determined using an ensemble approach. This approach involves random perturbation of observations to generate ensemble of data realizations. An ensemble approach was adopted in several studies for estimation of background error covariance models (e.g. Zagar et al., 2004; Pereira & Berre, 2006). Errors in the radial surface currents data were assumed to be uncorrelated. For each radial data used to generate surface current vectors, an ensemble of realizations was randomly generated using random normal numbers with zero mean and standard deviation was assigned the value of the error corresponding of the radial data. All the procedures undertaken to arrive at HFR SSHA were repeated for all the simulated realizations of data. Ensemble mean and standard deviations were computed to estimate the HFR SSHA uncertainties for each grid point. The maximum estimated standard deviation (0.01 m) was adopted as the geostrophic HFR SSHA uncertainty and it was more pronounced near the boundary of the domain where there are the most data gaps (Fig. 3.1).

The S3 SSHA data was adopted to check the fidelity of the Least Squares technique in estimating sea level anomalies. Using the cost function, anomalies in sea level were estimated from the raw hourly surface currents data using the invariant form of the momentum equation, which is similar to (Eqn. 1) but ignoring the perturbation terms. As speculated in Roesler et al., (2013), the resulting HFR SSHA was expected to be relatively comparable to the SSHA from S3 as both have the contributions of high frequency signals. While both datasets are comparable, there were still some differences present. S3 SSHA are instantaneous observations while the hourly surface current products from HFR are hourly mean over the hour mark (http://www.codar.com/intro_hf_currentmap.shtml). The hourly HFR surface currents contain the contributions of tidal currents while ocean tides were eliminated in the S3 SSHA using models, which may or may not accurately remove the contributions of ocean tides in the study area. There is an unknown bias in the differential sea level anomalies estimated using the cost function but it is not present in the S3 data. Therefore, for each satellite pass, the along-track mean of the S3 SSHA data was subtracted to reduce the SSHA to a zero reference. The estimated HFR SSHA from the raw and filtered surface current data were interpolated on the grid points of the S3 tracks and the spatial mean corresponding to the individual interpolated HFR SSHA were removed to also reduce the sea level anomalies to a zero reference.

Plots of 86 corresponding HFR and S3 SSHAs are shown in (Fig. C5) but few instances are shown in (Fig. 3.3). A notable difference between S3 and HFR SSHAs is the presence of high wavenumber oscillations in S3 SSHA (Fig. 3.3). The spatial resolution of the HFR estimated currents (6 km) are similar to the along-track altimeter sea level resolution. However, the process of estimating sea level from currents is an integrative process and acts as a low-pass filter. The high wavenumber oscillations in the along-track altimeter data were also reported in (Chavanne and Klein, 2010; Roesler et al., 2013). This contributed to the root mean square differences (rmsd) between the S3 and the HFR SSHAs estimates computed from raw HFR surface currents ranging from 0.00 - 0.09 m. Accounting for the errors in S3 SSHA (3.4 cm) and HFR SSHA estimated from raw surface currents (2 cm), 64% of the computed rmsd were within the error budget of 4 cm (Fig. 3.4a); for instance (Fig. 3.3a-3.3c). A similar result was obtained when the HFR SSHA estimated using geostrophic approximation was compared to S3 SSHA for an error budget of 3.5 cm (Fig. 3.4b). This suggests an encouraging result regarding the prospect of using the Least Squares technique in estimating anomalies in sea level. Furthermore, the result is in line with Chavanne and Klein, (2010) who had previously noted an agreement between the two products (HFR SSHA estimated using raw and subinertial surface currents and satellite altimeter SSHA) but in the open ocean region where satellite altimeter data are more reliable. However, there were cases when both S3 and HFR SSHAs were out of phase (Fig. 3.3d and 3.3f) and it was not surprising based on the differences in the two datasets that were previously enumerated as such, contributing to rmsd larger than the respective error budgets. Moreover, it is not unique to this study as Roesler et al., (2013) reported instances of statistically significant negative correlations in their study even after smoothing the open ocean satellite altimeter data to enhance its agreement with the HFR SSHA. Figure 3.3e is an instance when the rmsd was large due to the divergence of only three offshore points but there was agreement in the reminder of the points which further suggests that the differential sea level anomalies reconstructed using the Least Squares technique are reasonable.

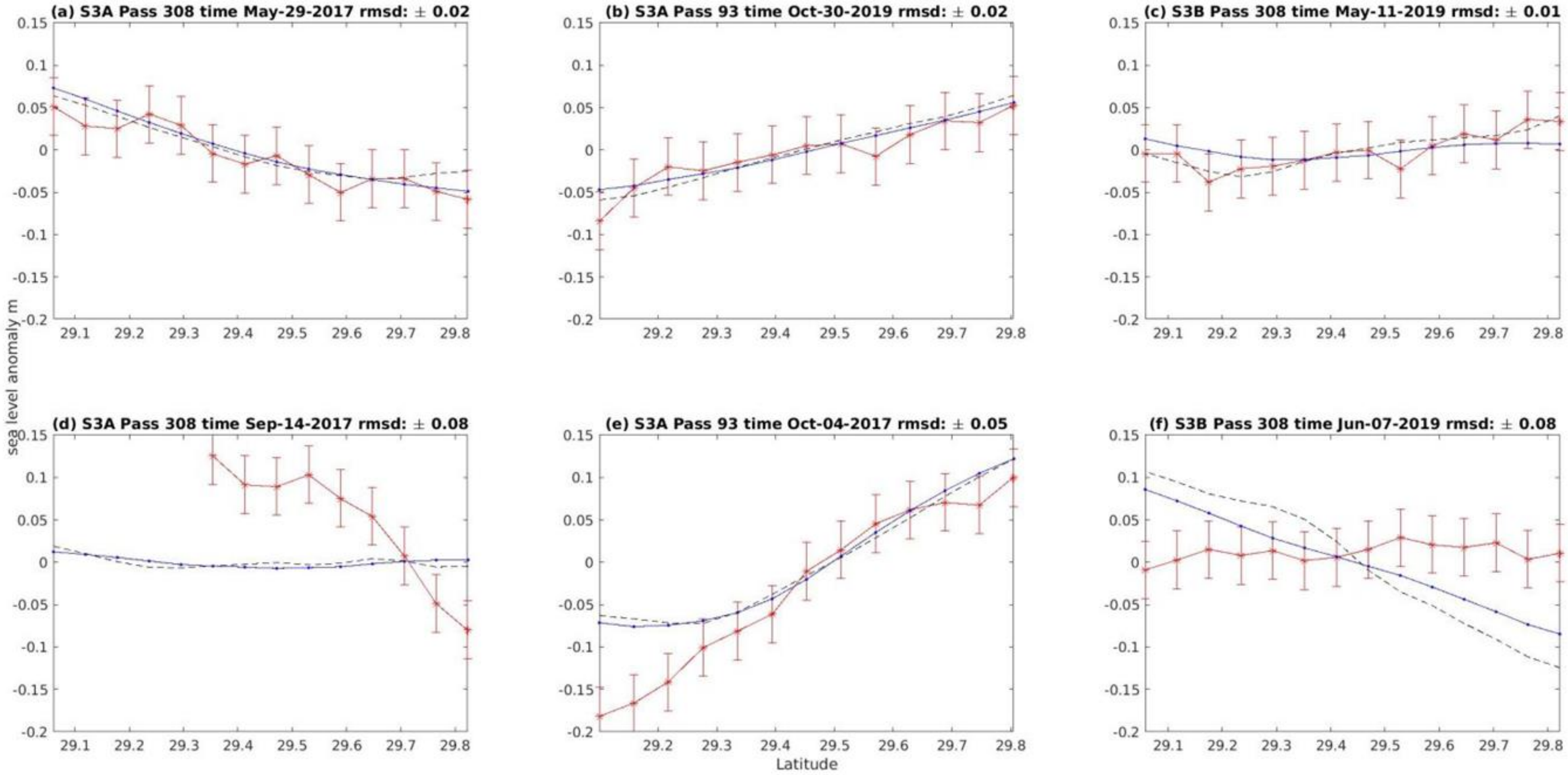

Figure 3.3 *S3A and S3B SSHA (red solid line with error bars of 3.4 cm), HFR SSHA estimated using geostrophic approximation (blue solid line with dots) and invariant form of the momentum equations applied to raw surface currents (blue dash line) and root mean square difference between S3 and HFR SSHA (from raw surface currents) (rmsd). Instances of agreement and disagreement between S3 and HFR SSHA are shown in panels a-c and d-f respectively.*

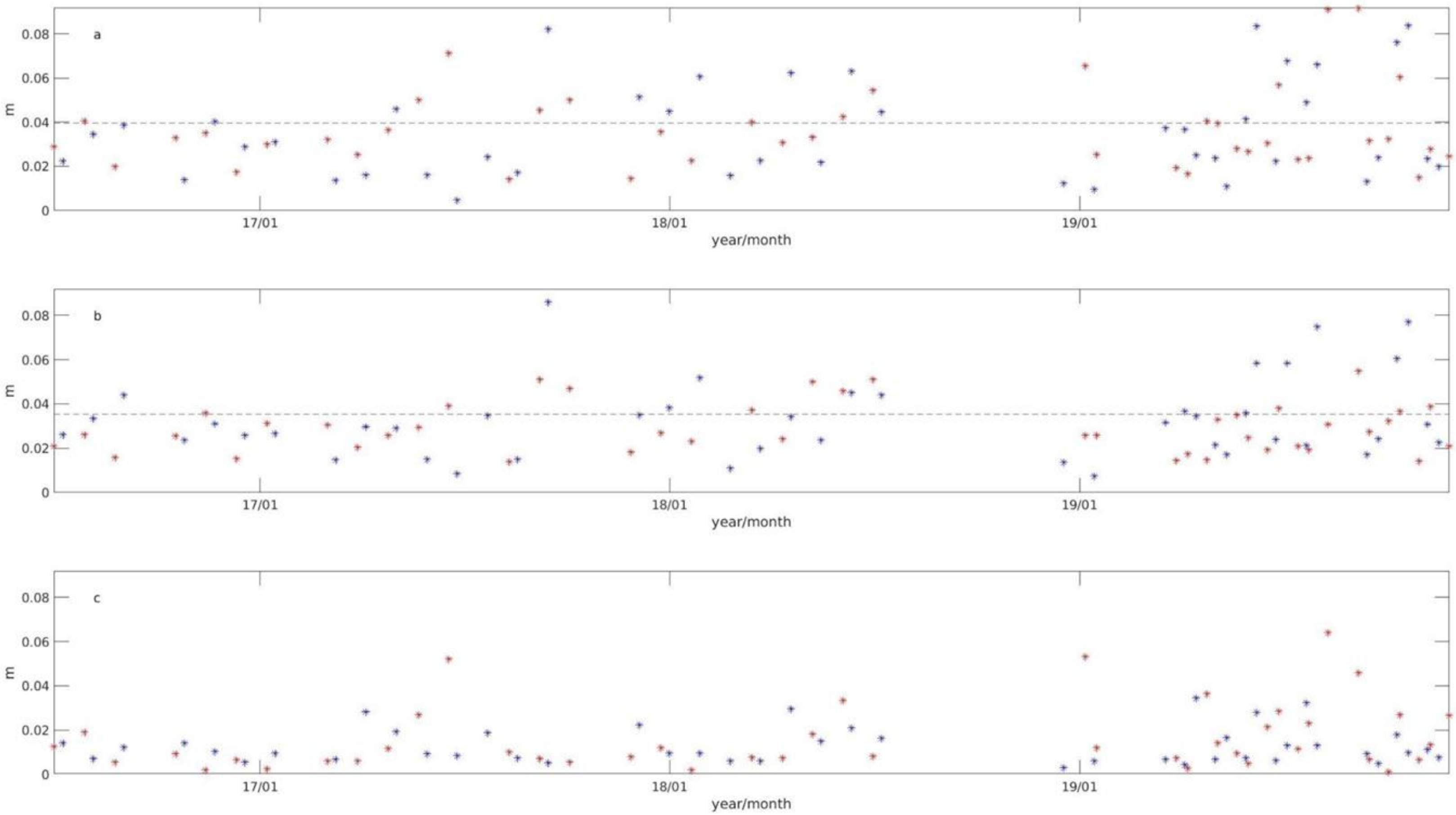

Figure 3.4 *(a) rmsd between S3 SSHA and HFR SSHA (raw surface currents). (b) rmsd between S3 SSHA and HFR SSHA (geostrophic approximation). (c) rmsd between HFR SSHA (raw surface currents) and HFR SSHA (geostrophic approximation).*

We compared the sea level temporal anomalies of the coastal gauge and the buoy to investigate the validity of the buoy datasets. This was done because, unlike the coastal gauge, the buoy was not stationary relative to the land. Both sea level stations were ~60 km apart. Figure 3.5a, shows that the magnitude of the sea level temporal anomalies at the coastal station was not always greater than the magnitude of the anomalies observed at the offshore buoy. For instance, a higher sea level anomaly observed at the buoy in October was due to Hurricane Nate as it approached the nGOM west of the buoy. Besides the contribution of the hurricane, we expected the amplitude of the sea level temporal anomalies at the coastal station to be higher, based on the influence of shoaling bathymetry on sea level amplitude (Woodworth et al., 2019). Considering that both stations were not co-located, we also expected a phase lag between the sea level temporal anomalies at the two locations. There was rather no pronounced phase lag in the sea level anomalies between the two stations. Considering a significant correlation coefficient of 0.94 at 95% confidence level between the two time series, it was safe to assume that the sea level temporal anomalies at the offshore buoy could serve as a check to the HFR SSHA.

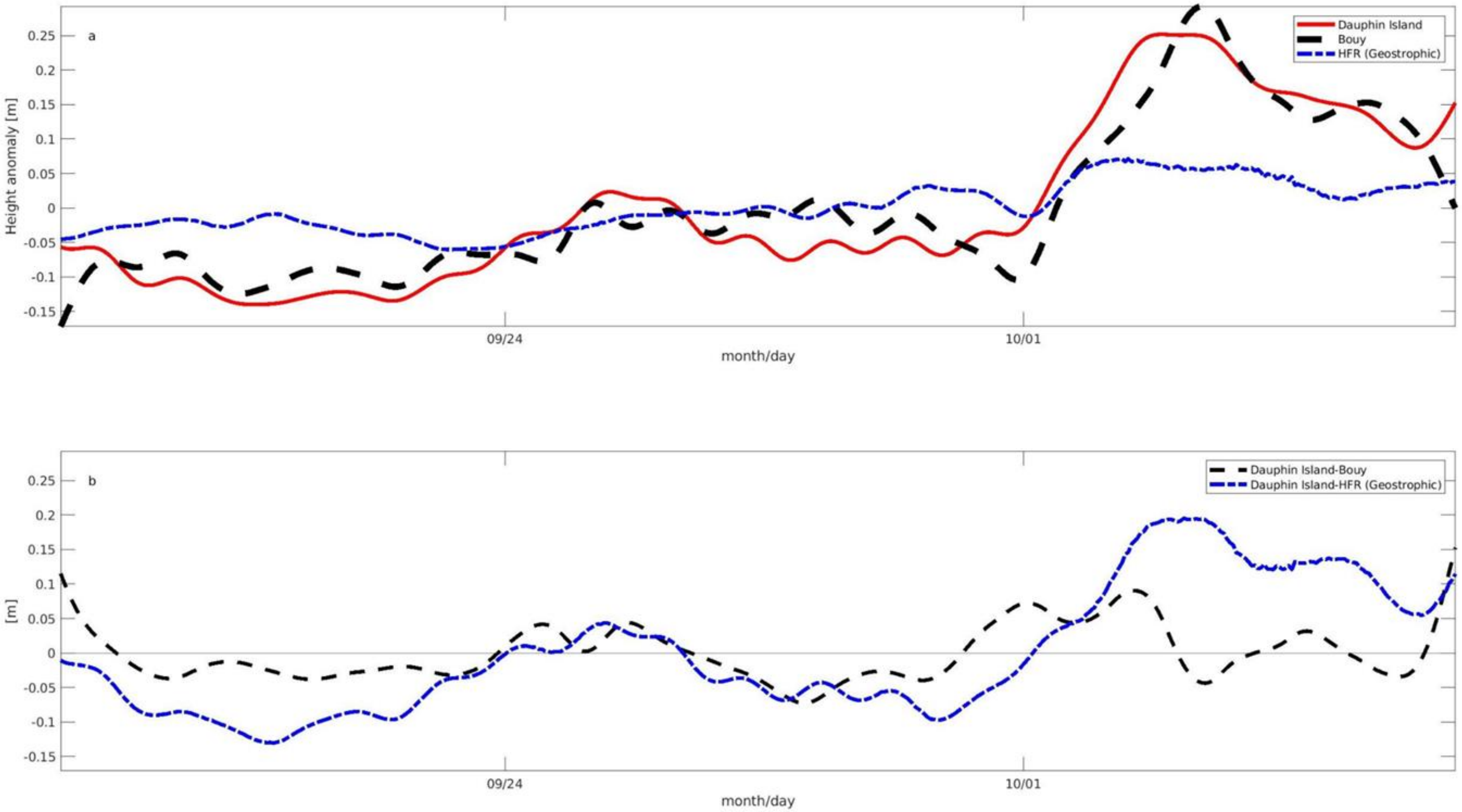

Figure 3.5 *(a) SSHA from 2017/9/18 – 2017/10/06 NOAA coastal sea level gauge 8735180 Dauphin Island (solid line) and offshore buoy (dashed line), and HFR estimates using geostrophic (dashed line and dot)from the nearest grid point to the buoy location. (b) SSHA differences between the coastal sea level gauge and offshore buoy (dashed line), and between the coastal sea level gauge and the same HFR estimates as in (a).*

HFR SSHA estimated from the geostrophic equation was compared with the buoy sea level temporal anomalies. Both time series were not of the same nature considering that the HFR SSHAs were with respect to a zero spatial mean while the buoy anomalies were with respect to a temporal mean. Irrespective of the different nature of the SSHA time series, we still compared the two. Firstly, a new HFR SSHA time series was generated from the centered spatial average of four HFR SSHA grid points in the vicinity of the buoy where the center of the average region was ~20 km from the buoy location. Secondly, the temporal mean of the resulting HFR SSHA time series was computed. By subtracting the temporal mean of the HFR SSHA, it became slightly more consistent with the buoy sea level temporal anomalies. We did not anticipate high correlations coefficients between the two SSHAs. It was rather surprising that the correlation coefficient and rmsd between the buoy and HFR SSHA were 0.80 ($p<0.05$) and 0.08 m respectively. Figure 3.5b further shows the similarities between these two time series as they were individually subtracted from the coastal sea level time series.

3.5 Empirical Orthogonal Functions (EOF)

Spatial and temporal patterns in the estimated HFR SSHA using Eqn. (4) were analysed using EOF. The field of SSHA was setup to correspond to the S-mode analyses which involves the re-arrangement of the sea level data into a 2-dimensional matrix where the columns of the matrix correspond to spatial positions while the rows correspond to time (Björnsson et al., 1997). Temporal means of each column were removed and the result was used to form a covariance matrix. The eigenvectors of the covariance matrix corresponding to the two largest eigenvalues were extracted. These eigenvectors (empirical modes) explained 85% of the spatiotemporal variability in the

HFR SSHA. Evolution of the various empirical modes was determined through the resulting principal component.

Figures 3.6 shows the first two empirical modes and their corresponding principal components. The first mode accounts for 47% of the variability in the HFR SSHA while the second mode accounts for 38% of the variability. The first mode shows that SSHA in the MSB slopes down towards offshore when the principal component is positive and towards the coast when the principal component is negative. In the case of the second mode, SSHA slopes down towards the west when the principal component is positive and towards the east when the principal component is negative. In the original principal component plots for the respective modes, patterns were not obvious due to high frequency oscillations. They were both filtered using a window of one month to reveal the more energetic low frequency signals (Fig. 3.6). Mode 1 principal component appears to have a periodicity of about 6 months in the first year between March 2016 and February 2017; it was positive in spring and fall but negative in summer and winter. Between March 2017 and February 2018, the pattern of the principal component was similar as in the previous year except for spring season, which was partly positive and partly negative. Due to the presence of gaps, the pattern of mode 1 principal component could not be adequately determined for the period between March 2018 and February 2019. It did however show that the principal component was positive in spring and tended towards negative in the summer as in the first year. The remaining record of the principal component resembled the second year as it was partly positive and partly negative in the spring, negative in the summer and mostly positive in the fall. The maximum magnitude of the principal component was in the fall of 2019. Unlike the mode

1 principal component, there was no obvious pattern in the mode 2 principal component. The magnitude of the principal component of mode 2 was mostly less than the magnitude of mode 1 and its maximum magnitude was in fall 2019. When the two principal components are in-phase (for instance: summer 2016 and 2017), the slope of sea level will be in the northeast-southwest orientation. This orientation changes to the northwest-southeast when the principal components are about 180^o out of phase (for instance: winter 2017, winter 2018, spring, summer and fall 2019).

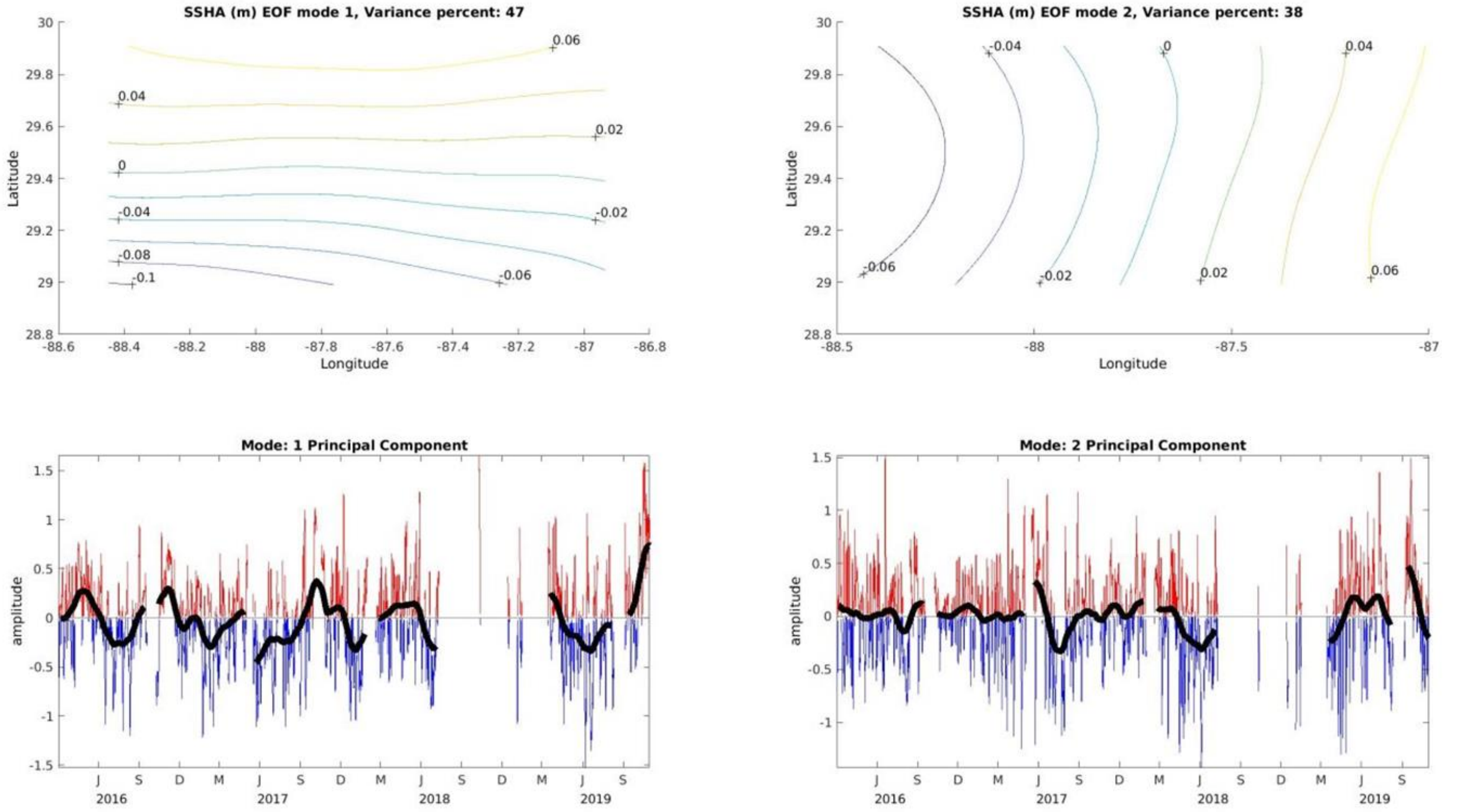

Figure 3.6 *First two empirical modes of the HFR SSHA (top plots) and one-month window box-car filtered Principal components of the first two empirical modes where the various seasons were represented in the horizontal axis: winter (December-February), Spring (March-May), Summer (June-August) and Fall (September-November) (bottom plots).*

3.6 Discussion

HFR data was fundamental in the analysis carried out in this study. While other studies in the MSB used depth integrated flow estimated using data from ADCP to study the circulation in the MSB, this study used surface flow estimated from HFR data to diagnose the terms in the momentum equation, estimate SSHA and the leading modes in the SSHA variability. The major drawback in the MSB HFR long-range data was the presence of the gaps. Simple and robust techniques were adopted in filling a reasonable amount of the data gaps but some gaps remained. If there was redundancy in the number of HFR observing stations, it might not only mitigate data gaps resulting from system mal-functioning but also data gaps resulting from environmental hazards such as Hurricanes. It is believed that with redundancy in HFR observing stations, the data gaps will be negligible and could be filled using an adequate interpolation technique. Furthermore, with redundancy in the HFR stations, there will be a better quality assurance in the resulting surface currents radial and vector data.

Using the available HFR and wind data, diagnostics of the terms in the momentum equation were conducted to determine if the geostrophic balance was dominant at the subinertial time scales in the MSB. Results of the diagnostics showed that the Coriolis terms were dominant in both the along-shelf and across-shelf momentum equations, as the $R_o<0.1$ prevailed in the domain. Consequently, the sea level gradient terms will balance the Coriolis terms implying that geostrophic balance is dominant. A similar balance was found in the across-shelf momentum equation of the West Florida Shelf by Liu & Weisberg (2005). Liu & Weisberg (2005) using depth averaged momentum equations showed that the magnitudes of the Coriolis and bottom pressure gradient terms were larger compared to the other terms in the across-shelf momentum equation, and both were significantly correlated and balanced each other. Their results further indicated that when the other terms in the across-shelf momentum equation were added to the Coriolis term, the balance with the pressure gradient term slightly improved as there was about 14% and 4% increase in correlation in the nearshore (~15 m depth) and offshore (~126 m depth). Unlike the across-shelf momentum, Liu & Weisberg (2005) noted that geostrophic balance was not dominant in the nearshore region of the along-shelf momentum. However, it would become the dominant balance from ~30 m depth towards offshore as the magnitude of the Coriolis term became dominant. Thus, the results in Liu & Weisberg (2005) were consistent with the results of our study even though our analysis were based on data from the ocean surface. Considering that the magnitude of the ageostrophic terms were insignificant and could be neglected, the dynamics in the MSB can be adequately represented by geostrophic approximation.

The feasibility of obtaining reliable SSHA using a Least Squares technique was validated using SSHA from a satellite altimeter. Satellite altimeters provide high frequency (20 Hz) instantaneous along-track sea level data. The data used in this study were the average of the high frequency data at 1 Hz. Hence, the small-scale sea level anomalies present in the observed altimeter data (Fig. 3.3). Unlike the satellite altimeter SSHAs, SSHAs from HFR were not from measured sea level but estimated from subinertial surface currents after the application of Least Squares technique. The interpolation of the estimated HFR SSHA along the track of the satellite and the removal of the individual along-track SSHA spatial mean resulted in consistent and relatively comparable datasets. From both products, it was deduced that the MSB SSHA amplitude along the satellite track, which is in the north-south orientation, is mostly less than 0.1 m. In more than half of the cases of corresponding S3 and HFR SSHA, the rmsd that resulted from the comparison of the HFR SSHA estimates (filtered (subinertial) and raw surface currents) to the SSHA from satellite altimeter were within the error budget of S3 SSHA. This was an indication that reliable SSHA for the MSB can be determined by applying the Least Squares technique to HFR data.

Instances of large rmsd do not necessarily invalidate the SSHA from either technique. Liu et al., (2012) acknowledged that the differences in measuring techniques and measured variables complicates the comparisons of both datasets. For instance, S3 provides instantatenous SSHA and if a trending signal in the domain is short-lived (< 1 hour) and prevailed during the satellite overpass, the magnitude is preserved in the S3 data. However, the signal may not be dominant in the HFR SSHA given that the surface currents from the HFR are not instantatenous. This will result in a divergence between both S3 and HFR SSHA. Divergence between both S3 and HFR SSHA could result from unreliable SSHA. In events of high radar backscatter from the surface ocean (Sig0 > 14 dB) and high significant wave height (SWH > 3m) the reflected altimeter signals from the ocean surface are not reliable, hence this results in degraded satellite altimeter data (Tournadre et al. 2006; Roesler et al., 2013). The study by Roesler et al., (2013) casts doubts on the reliability of satellite altimeter data on the shelf due to the complexities of shelf processes compared to open ocean processes. Additionally, Liu et al., (2012) reported that the root mean square differences between the ‘geostrophic velocities’ estimated from X-TRACK ‘a coastal satellite altimeter product’ and observed velocities from HFR were not within their study error budget. However, it is not consistent with the result of this study potentially due to differences in study regions, compared variables and data sources. The HFR SSHA estimated in this study can be unreliable in cases when there are gaps present in the data especially when the gaps are near the boundary of the domain. This is another reason for redundancy in HFR stations in the region. The detailed analyses of the reason(s) for the large rmsd between the S3 and HFR SSHA is beyond the scope of this study as there is no sufficient data.

SSHAs determined using the geostrophic balance approximation and the invariant form of the momentum equations provided some insights on the dominance of geostrophic balance. If the other terms in the invariant form of the momentum equation besides the Coriolis and pressure gradient terms are significant then when they are included in the estimation of MSB SSHA the resulting SSHA should differ significantly from the SSHA estimated using geostrophic approximation. Several instances that were considered confirmed that there were differences between the two HFR SSHA estimations (Fig. 3.3). Though there were differences in the magnitude of the SSHA, in most cases, there were agreement in the trends of the two SSHA estimates, which resulted in small values of the computed rmsd (Fig. 3.4c). It implies that even at scales lower than subinertial scales geostrophic balance is important in the MSB. As such, at subinertial scales, contributions of the non-linear and time derivative terms to sea level gradient can be ignored in the MSB. Consequently, the estimation of MSB SSHA from geostrophic approximation is reasonable. The major drawback in using this balance is inability to observe finer details in the MSB dynamics.

Based on the principle of geostrophy, high pressure (sea level) is to the right of geostrophic currents in the northern hemisphere. The first EOF mode of the SSHA reveals that the currents in the MSB were majorly in the east-west orientation hence the north-south sea level gradient. This is consistent with the mode 1 of the surface currents reported in Ohlmann & Niiler (2005). Coincidentally, we both reported the same percentage of energy for mode 1. Surface currents variance ellipses for the region from other sources (Ohlmann et al. 2001; Hode, 2019) showed the currents are mostly along the east-west orientation which is similar to the orientation of the bathymetry of the region. The orientation of the currents changes to the north-south based on the SSHA mode 2. This was partly consistent with the mode 2 reported in Ohlmann & Niiler (2005) which not only had a north-south component but also an east-west component.

The results of our study did not entirely agree with the results of previous studies. We assume that the discrepancies with some of the studies stems from differences in techniques as well as prevailing conditions. He & Weisberg (2003), reported that the mean currents for the spring of 1999 flowed towards the east. Though our result showed that there was no preferred current direction in spring 2017 and 2019, it also showed that currents flowed towards the west in spring of the other years. Their analysis focused on model result depth-averaged currents, which was similar to the model result mid-depth currents unlike our analysis that involved only HFR surface currents. Additionally, while our data is insufficient (~ 4 years) to draw a statistical conclusion on the nature of the flow for the various seasons, we had more statistics compared to analysis based on a single season. We suspect that the eastward flow in the spring (March to May of 2005-2008) that was also reported by Dzwonkowski & Park (2010) was because their analysis was based on depth averaged velocities. However, based on the velocity profiles for the spring season (Dzwonkowski & Park, 2010 figure 4), it appears that the surface velocities tended towards the west as well as surface velocities for the other seasons. While the surface velocities reported in Dzwonkowski & Park (2010) were consistent with our results in some season, other seasonal study focused around this site showed temporal and spatial variability in the surface currents attributed to the close association with Mobile Bay estuarine discharge (Dzwonkowski & Park, 2012; Dzwonkowski et al., 2014). It did not correspond to the surface currents reversal reported in Ohlmann & Niiler (2005) thus, the misrepresentation of the surface currents likely resulted from poor extrapolation. A better comparison to our results are the studies conducted by Morey et al., (2003a) and Ohlmann & Niiler (2005) using drifters and by Hode (2019) using HFR. The dataset used by Morey et al. (2003a) and Ohlmann & Niiler (2005) has some overlap hence, we could expect some similarities in results. The same applies to the data used in Hode (2019) and our study. In Morey et al. (2003a), westward flow reported for the winter season was not consistent with our result however, the eastward flow in the summer season was consistent with our result. Monthly mean velocities reported in Ohlmann & Niiler (2005) were also not entirely consistent with the results reported in Morey et al. (2003a) as currents were mostly towards the west in January, February and August, towards the east in July and no preferred direction in June and December. Ohlmann & Niiler (2005) also showed that there were no preferred current direction in the spring thus, not consistent with He & Weisberg (2003). Our results for the fall season are in agreement with Ohlmann & Niiler (2005) except for September where they showed that there was no preferred current direction. When compared to the monthly climatology of the surface currents reported in Hode (2019), our result are consistent for the fall and summer seasons. The results are largely consistent with the winter seasons except for

December when there was no preferred current direction. In spring, Hode (2019) reported that currents flowed towards the west in March but had no preferred direction in April and May. The agreement between our results and the result of previous studies consolidates our assumption of geostrophic balance as the dominant balance in the MSB. The details of the physical processes involved with the anomalies in geostrophic sea level are beyond the scope of this study.

CHAPTER IV – CONTRIBUTIONS OF FORCING MECHANISMS TO THE SEASONAL CHANGES IN SEA LEVEL IN THE MISSISSIPPI BIGHT

4.1 Introduction

One of the ways the ocean responds to the variabilities in physical processes is through changes in sea level. These variabilities in physical processes are initiated by forcing mechanisms, which includes but are not limited to atmospheric pressure, wind and gravitational pull from astronomical bodies. For instance, changes in the differences between gravitation pull of the moon and sun and the centrifugal force on earth with respect to the respective barycenters of the earth-moon and sun-earth barycenter cause low and high ocean tides (Pugh & Woodworth, 2014). When the contributions of these mechanisms are coherent such as the combination of the inverted barometric effect of a decrease in atmospheric pressure and a persistent wind stress towards a coast in high tide, a large sea level gradient develops that can subsequently result in catastrophic flooding to coastal residents (Woodworth et al., 2019).

Different forcing mechanisms prevail at different spatiotemporal scales in different water bodies. Woodworth et al., (2019) posited that in coastal regions, wind stress dominates the inverted barometric effect of the atmospheric pressure. They further noted that the presence of the coast leads to the formation of a horizontal gradient in sea level as it obstructs wind driven transport. Wind is the major forcing mechanism on the continental shelves of the Gulf of Mexico (GOM) (He & Weisberg, 2003b; Liu & Weisberg, 2005).

Wind stress influences nGOM circulation and sea level at different temporal scales. GOM wind regime changes significantly in events of tropical cyclones and cold fronts (Zavala-Hidalgo et al., 2014). Between the two, tropical cyclones (hurricanes) lead to higher sea level changes (~1m) as shown in (Nwankwo et al., 2017a,b; Nwankwo et al., 2020). The passage of cold fronts result in relatively lesser wind magnitude when compared to tropical cyclones and causes clockwise changes in wind direction from the northwestwards to southeastwards direction (Dzwonkowski et al., 2015). Due to the lower intensity, there are also lower changes in sea level (<0.5m) (Dzwonkowski et al., 2015; Woodworth et al., 2019). Given that these are considered as high frequency processes (Woodworth et al., 2019), the gradient in sea level due to these events are not sustained once the wind magnitude reduces or the wind changes direction (Walker et al., 2013). Low frequency variability in wind has been previously reported to influence the nGOM sea level gradient. Mitchum & Clarke, (1986) and Chuang & Wiseman, (1983) reported the wind to be correlated with sea level changes in the West Florida Shelf (WFS) and Texas-Louisiana shelf respectively. Dzwonkowski & Park, (2012) noted a relationship between wind forcing and coastal water-level in response to upwelling and downwelling favorable winds. However, there are no studies of the impact of wind on the sea-level gradient over the broad shelf region of the nGOM.

Similarly, the role of the LC on sea level gradient in the nGOM remains an open question. The Loop Current (LC), including the Loop Current Eddies, (LCE anticyclone) is the major physical process that influences the circulation in the GOM (Morey et al., 2003a; Morey et al., 2003b). The influence of the LC becomes pronounced as the loop intrudes towards the nGOM. Maul, (1977) and Sturges & Evans, (1983) showed how far the intrusion of the LC can extend towards the nGOM. Based on the difference in the periodicity of the LC intrusion that they respectively estimated, it implied that LC intrusions towards the northern Gulf are episodic ranging from months to interannual time scales. The behavior of the LC as a dynamical feature affects shelf circulation. Studies on the WFS have shown the influence of the LC intrusion on salinity and temperature (e.g. Huh et al., 1981), sea level (e.g. Sturges & Evans, 1983; Li & Clarke, 2005; Liu et al., 2016), and currents (e.g. He & Weisberg, 2003a). Li & Clarke, (2005) reported that LCE which propagate westwards, contribute to sea level changes on the Texas shelf. Sturges & Evans, (1983) noted that the LC rarely extends onto the shelf of the nGOM and the importance of this major feature on shelf processes in the nGOM is unclear. In one of the few cases when the LC intruded onto nGOM shelf, Huh et al., (1981) reported that the LC enhanced cross-shelf flow but did not state if the LC had any influence on sea level.

The first and fourth largest freshwater sources (Mississippi River (MR) and Mobile Bay (MB) respectively) (Dzwonkowski & Park, 2010) in the continental United States empty into the northern shelf of the nGOM yet it is unknown how much the instances of increased freshwater discharge contribute to sea level gradients in the nGOM. Both freshwater sources contribute to the buoyancy changes in nGOM surface layer through the formations of both horizontal and vertical density gradients. Unlike the previous two mechanisms, freshwater discharge has a lesser contribution to GOM circulation (Greer et al., 2018). The contributions of freshwater discharge to the GOM circulation are more pronounced in the inner to mid shelf regions (Morey, et al., 2003a; Greer et al., 2018). The reason is because both regions are closer to the source of the freshwater discharge and the water column in the regions respond faster to temperature fluctuation due to shallow water depths (Morey & O’Brien, 2002; Dzwonkowski & Park, 2010). Freshwater discharge have been previously reported to contribute to an along-shelf southeastwards jet in the WFS (He & Weisberg, 2003b). Furthermore, freshwater discharge enhances cross-shelf circulation as reported in (Dzwonkowski et al., 2017). Dzwonkowski & Park, (2010) speculated that the barotropic pressure gradient due to freshwater discharge may be responsible for the eastward depth averaged flow over the inner shelf of Alabama. Dzwonkowski et al., (2015) showed an increase in sea level at the mouth of Mobile Bay as the momentum of freshwater discharge increase due to a flood event with no discussion of the impact of freshwater discharge on nGOM sea level gradient.

As noted by Dzwonkowski & Park, (2012), there are few oceanographic studies on the nGOM but even fewer studies on the contributions of different mechanisms to the variability of sea level gradient in nGOM. The focus of this study is to investigate the effects of wind stress, LC and freshwater discharge on the patterns of variability in the sea level gradient calculated in the previous chapter at monthly to interannual time scales. At such temporal scales, variability in sea level gradient has a corresponding variability in circulation due to the prevalence of the geostrophic balance. Irrespective of some data unavailability that hampered a robust analysis, this study attempted filling the gaps in previous studies using the available datasets. Given that the influence of wind is dominant on the shelf and results in sea level setup (Weisberg et ., 2005; Kim et al., 2010; Lentz & Fewings, 2012), a model was developed to determine to which extent the wind contributes to sea level gradient variability. The part of the sea level gradient variability not explained by the wind was used to investigate the individual contributions of LC and freshwater discharge to the patterns in the sea level gradient.

4.2 Data and Methods

4.2.1 Data Sources

Data from several sources were synthesized in the analysis of the individual contributions of the mechanisms of interest to nGOM sea level gradient. Coastal sea level and wind data had previously been analyzed, while sea surface height anomaly (SSHA) data were recovered from high frequency radar (HFR) data. Detailed descriptions of the various data can be found in Chapter 3. (Note that the SSHA were with respect to the individual differential sea surface height spatial mean at a given time stamp). Hereinafter the recovered SSHA from HFR data is referred to as HFR SSHA. The HFR SSHA was derived from surface currents data measured using HFR maintained by the Central Gulf of Mexico Ocean Observing System (CenGOOS) at the University of Southern Mississippi (USM). The estimated HFR SSHA were on a regular grid and covered both the mid and outer shelf (Fig. 4.1). An optimal wind data was generated by combining wind data from wind stations (Fig. 4.1) close to the study area. The coastal sea level data was from NOAA station 8735180 at Dauphin Island and was eventually corrected for inverted barometric effect. The coastal sea level, HFR SSHA and wind data were at hourly intervals and spanned from February 1, 2016 to November 30, 2019.

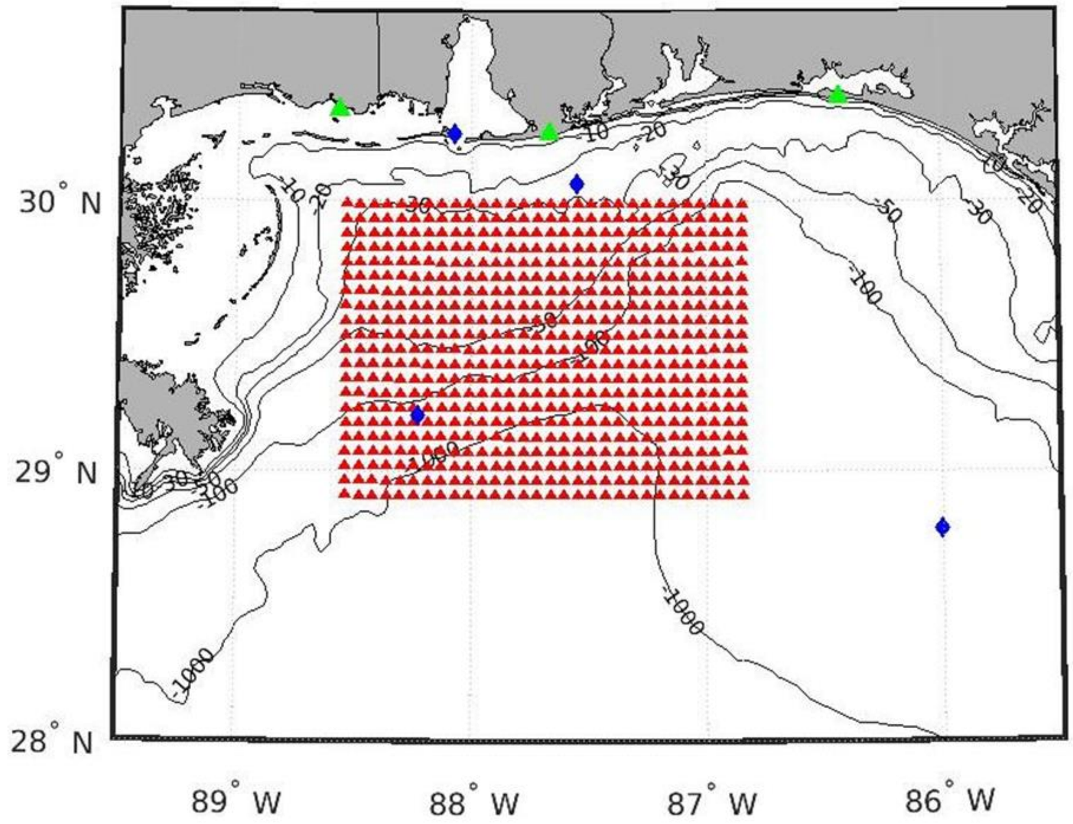

Figure 4.1 *The wind stations (blue diamonds: starting from the northmost and moving in the clockwise direction dpia1, 42012, 42039 and 42040), the ~5 MHz HF radar stations (green triangles) located at Singing River Island, Orange Beach and Henderson Beach State Park (from left to right) and surface current grid points (red triangles).*

Data for investigating the contributions of LC to the nGOM sea level gradient can be obtained from different techniques. These methods of identifying the LC in data have evolved with advancement in technology. An isotherm (20^o C) determined at a given depth from hydrographic data can be used to identify the intrusion of the LC (Maul, 1977; Sturges & Evans, 1983). The technique is expensive, as it requires ship-based observations. However, the advent of satellite based observations made LC identification easier. Considering the higher temperature of LC water masses with respect to GOM water masses, infrared images from satellites provided a cost effective method of observing LC intrusions as shown in Huh et al., (1981). However, during the summer season the upper layer of the GOM becomes warm and nearly homogenous presenting a challenge in studying LC intrusion from infrared images (Sturges & Leben, 2002). Gridded sea surface height (SSH) determined from satellite altimeter were used in LC studies without the difficulties of near homogenous summer SST (e.g. Sturges & Leben, 2002; Walker et al., 2013). For this study, LC intrusions were determined using gridded SSH data provided by the Gulf of Mexico Coastal Ocean Observing System, GCOOS, at Texas A&M University, Dept. of Oceanography. The gridded SSH resulted from the interpolation of data from different satellite altimeters and are corrected for geophysical errors (Leben et al., 2002). The SSH data used in this study spanned over the study period.

Freshwater discharge from both the MB and MR are used in this study. Discharge into the MB is predominantly from two river sources Alabama River and Tombigbee River. Discharge data from stations 02428400 Alabama River at Claiborne (https://waterdata.usgs.gov/nwis/dv?referred_module=sw&site_no=02428400) and 02469761Tombigbee River at Coffeeville both in Alabama (https://waterdata.usgs.gov/nwis/dv?referred_module=sw&site_no=02469761) were used for estimating MB discharge. MR discharge at Tarbert Landing provided by the U.S. Army Corps of Engineers from was used (https://rivergages.mvr.usace.army.mil/WaterControl/stationinfo2.cfm?sid=01100Q&fid=RCKI2&dt=S&pcode=QR). Discharge data for both stations were at daily intervals and over the study period.

4.2.2 Data Processing

Here is a brief description of the steps taken in processing the HFR surface currents, wind data and coastal water-level data. Using a cut-off period of two days, the HFR surface currents data were low-pass filtered to obtain sub-inertial surface currents. A Least Squares procedure was applied to the sub-inertial surface currents to estimate the sub-inertial HFR SSHA that retains the geostrophic balance with velocities. Empirical orthogonal decomposition of the sub-inertial HFR SSHA revealed the two dominant modes of SSHA in the MSB and the corresponding principal components (PC). Additionally, monthly means of the HFR SSHA were computed to reveal low frequency features and to understand the evolution of the spatial variabilities in the HFR SSHA. Wind stress components (τ_x and τ_y) were estimated using the Large & Pond, (1981) formula. The τ_x and τ_y of the wind stress components are in the east-west and north-south orientations respectively where the east and north directions are positive while west and south directions are negative. The coastal sea level data was corrected for inverted barometric effect before the temporal mean was subtracted from the coastal sea level data. These time series (PC1 and PC2 of HFR SSHA, τ_x, τ_y, and coastal sea level anomaly) and the other time series used in this study were filtered using a window of one-month. The filter window was chosen to mitigate the energy of high frequency processes while preserving the low frequency (greater than one month) variabilities in the mechanisms.

Unlike the previous data, all the necessary geophysical corrections were already applied to the satellite altimeter gridded SSH data hence, no other corrections were required before features of interest were identified. In this study, it was assumed that LC intrusion begins when the northmost portion of the margin crosses latitude 26° N from south to north and ends when a LCE has separated from the LC and the LC retracts below 26° N from north to south. The LC and LCE were considered as a single Loop Current system because as the LCE detaches and separates from the LC it retains the high velocity core of the LC (Leben, 2005; Donohue & Watts, 2016), while the Loop Current Frontal Eddies (LCFE) were treated as a different system. Walker et al., (2013) previously identified both the LC and LCE using + 0.17 m SSH contour and the LCFEs using – 0.15 m SSH contour. A similar convention was adopted in identifying the LC, LCE and LCFE features approaching the study region. The features were identified only when they cut across or were within the latitudes 26° N – 29° N and longitudes 86.5° W – 88.5° W as it is the region where they might influence MSB shelf processes. Cyclonic and anticyclonic features observed in the study region from the gridded satellite altimeter SSH were not considered because sea level changes on the shelf and coastal regions (mostly small-scale features) from gridded altimeter products are usually less reliable than the large-scale sea level changes in the open ocean (Leben et al., 2002). For any of the identified features, only the latitude of the northmost position of the contour within the designated region is determined. In the cases of more than one LCFEs around the LC or LCE margin, the northmost LCFE is identified.

The MR discharge data was readily available for analysis but additional processing was required for MB discharge data. The MB discharge was estimated from Alabama River and Tombigbee River discharge data using Equ. 1.

$$q_2 = {}^{q_1}\!/_{C} \qquad \text{(Equ. 1)}$$

where q_1 is the sum of both daily discharge data from Alabama River and Tombigbee Rivers and C is 0.895 which corresponds to the ratio of the total watershed area and the watershed area of the two rivers sources (Dykstra & Dzwonkowski, 2020).

4.2.3 Data Analysis

Complex linear correlation and regression analyses were the two analytical techniques used to determine the role of wind stress in the development of MSB sea level gradient and evolution. The relationship between the principal components (PC1 and PC2) and the wind stress (τ_x and τ_y) was determined from the correlation coefficient computation. Complex correlation technique (Kundu, 1976) was adopted in the computation of correlation coefficients. In this study, all the computed correlation coefficients are statistically significant at the 95% confidence level. Any instance of insignificant correlation coefficients is explicitly stated. A regression model (Eqn. 2) was developed to estimate the temporal variability in the sea level gradient due to the wind stress.

$$PC_m = b_1 \times \mathrm{T} + b_0 \qquad \text{Eqn. 2}$$

where, PC_m is a model generated complex principal components whose real and imaginary parts are PC1 and PC2 respectively, b_1 is a regression complex coefficient, T is complex wind stress where the real and imaginary parts are τ_x and τ_y respectively and b_0 is a complex y intercept. A similar regression model but involving real vectors was used by Dzwonkowski & Park, (2010) to estimate the non-wind component of along-shelf current in the coastal region north of the study area. Components of PC_m corresponding to PC1 and PC2 were subtracted from the original respective PC1 and PC2. Residuals of the principal components were further investigated for the contributions of other mechanisms (LC and freshwater discharge).

In the analysis of the contribution of the LC to the residual PC, a qualitative approach was adopted. It involved the visual analysis of the evolution of the mean monthly HFR SSHA and the variability of the residual PC1 as the LC as well as the LCFE intruded towards the northern shelf of the nGOM. This visual approach is a speculative technique compared to the quantitative approach (cross-spectra analysis) adopted in Sturges & Evans, (1983). Though speculative approaches are not recommended in scientific analysis Li & Clarke, (2005) utilized this approach in the discussion of the contributions of the LC to the coastal sea level variability of the nGOM.

In addition to the previous two analyses, the potential contribution of freshwater discharge to the study area with emphasis on the residual principal component was analysed from freshwater discharge data, monthly MODIS-Aqua satellite imagery of gelbstoff and detrital material absorption coefficient, and kinetic energy of velocity anomalies estimated in the previous chapter. The monthly MODIS-Aqua satellite imagery of gelbstoff and detrital material absorption coefficient was provided by Ocean Biology Processing Group (NASA/GSFC/OBPG). The absorption coefficient was estimated using generalized inherent optical property algorithm. With regards to the kinetic energy of velocities anomalies, it increases because of the increased velocity shear caused by freshwater front (Dzwonkowski et al., 2015). As such, with respect to sub-inertial currents, these velocity anomalies can be considered as ‘turbulent currents’ (currents whose variabilities are on timescales less than 2-days) contributing to the dynamics via Reynolds fluxes of momentum. EOFs of the gradient turbulent kinetic energy were estimated to determine the modes in the variabilities of the gradient turbulent kinetic energy so as to investigate if they are related to the fluctuations in freshwater discharge. Hereinafter the gradient turbulent kinetic energy of the turbulent current is referred to as turbulent energy.

4.3 Results

4.3.1 HFR SSHA Variabilities

Figures 4.2 and 4.3 show the spatial variability in the HFR SSHA. Some monthly mean HFR SSHA field were missing due to data gaps. Based on the available monthly mean HFR SSHA field (Fig. 4.2), the range in sea level anomaly varied between 0.01 m and 0.10 m. Some of the features shown in Fig. 4.2 did not necessarily prevail over an entire month but had a predominantly high sea level anomaly amplitude in the domain; for example the cyclonic feature present in the domain in October 2016. Fig. 4.2 does not show any regular pattern in the HFR SSHA. However, the empirical modes (Fig. 4.3) depicted a more defined spatial variability in the HFR SSHA; mode 1 showed a sea level gradient in the north-south orientation while the sea level gradient in mode 2 was in the east-west orientation.

There were differences in the evolution of the HFR SSHA spatial features in the monthly means and the EOF modes. There was no obvious temporal cycle in the monthly plots. If the HFR sea level gradient responded to the influence of either wind or freshwater discharge, which have known temporal variability, then a temporal pattern should be present in the HFR sea level gradient. Conversely, the PC (Fig. 4.4a) of the respective modes of sea level gradients shown in (Fig. 4.3) have different patterns.

Between the two PCs, PC1 has a more pronounced temporal cycle with a periodicity of ~6-months (Fig. 4.4a). PC2 was mostly positive with negative excursions mainly in the summer and sometimes in the spring (Fig. 4.4a).

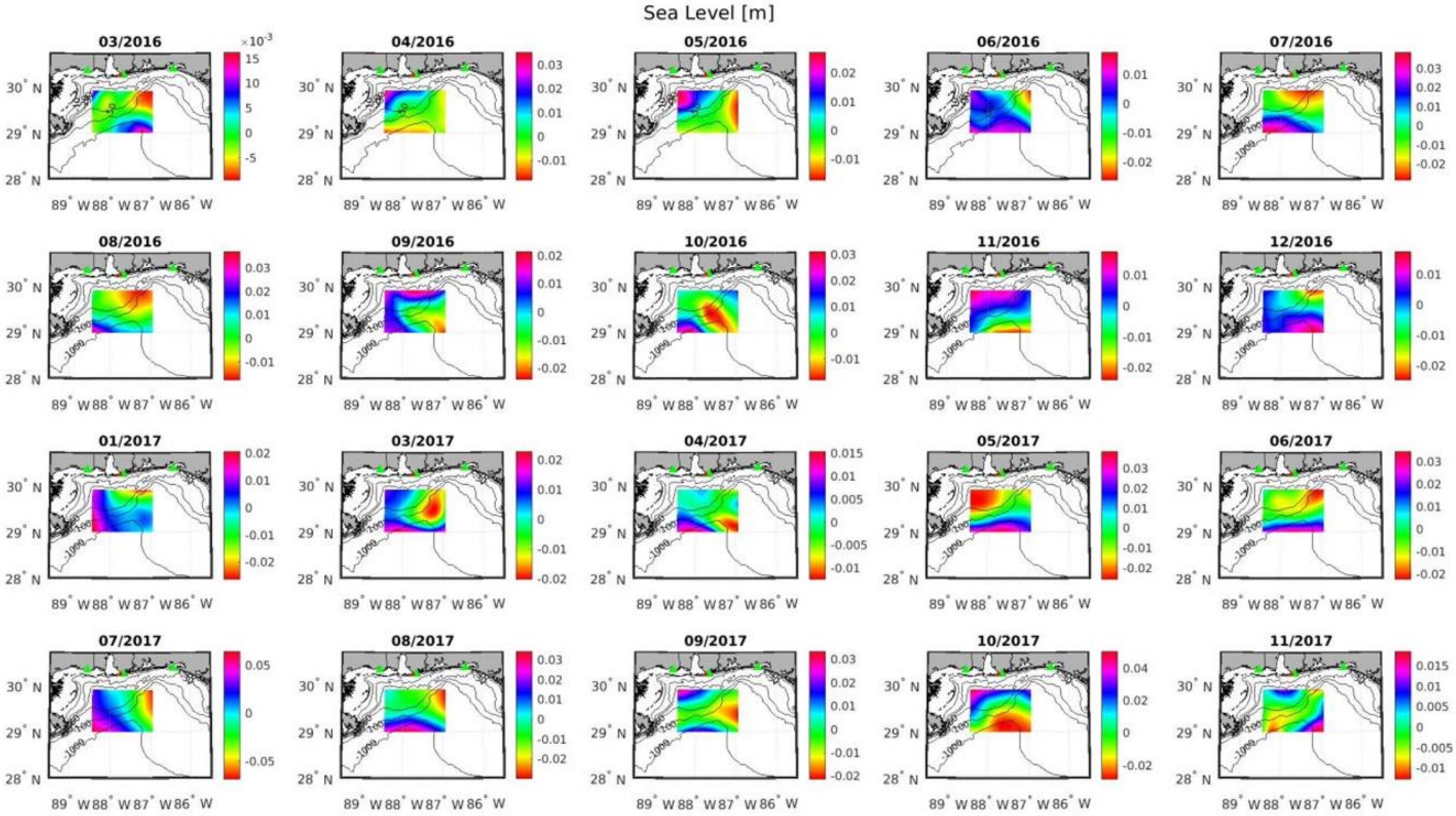
Sea Level [m]
03/2016
04/2016
05/2016
06/2016
07/2016
08/2016
09/2016
10/2016
11/2016
12/2016
01/2017
03/2017
04/2017
05/2017
06/2017
07/2017
08/2017
09/2017
10/2017
11/2017
30° N
29° N
28° N
89° W
88° W
87° W
86° W
-1000
-100
-50
×10^-3

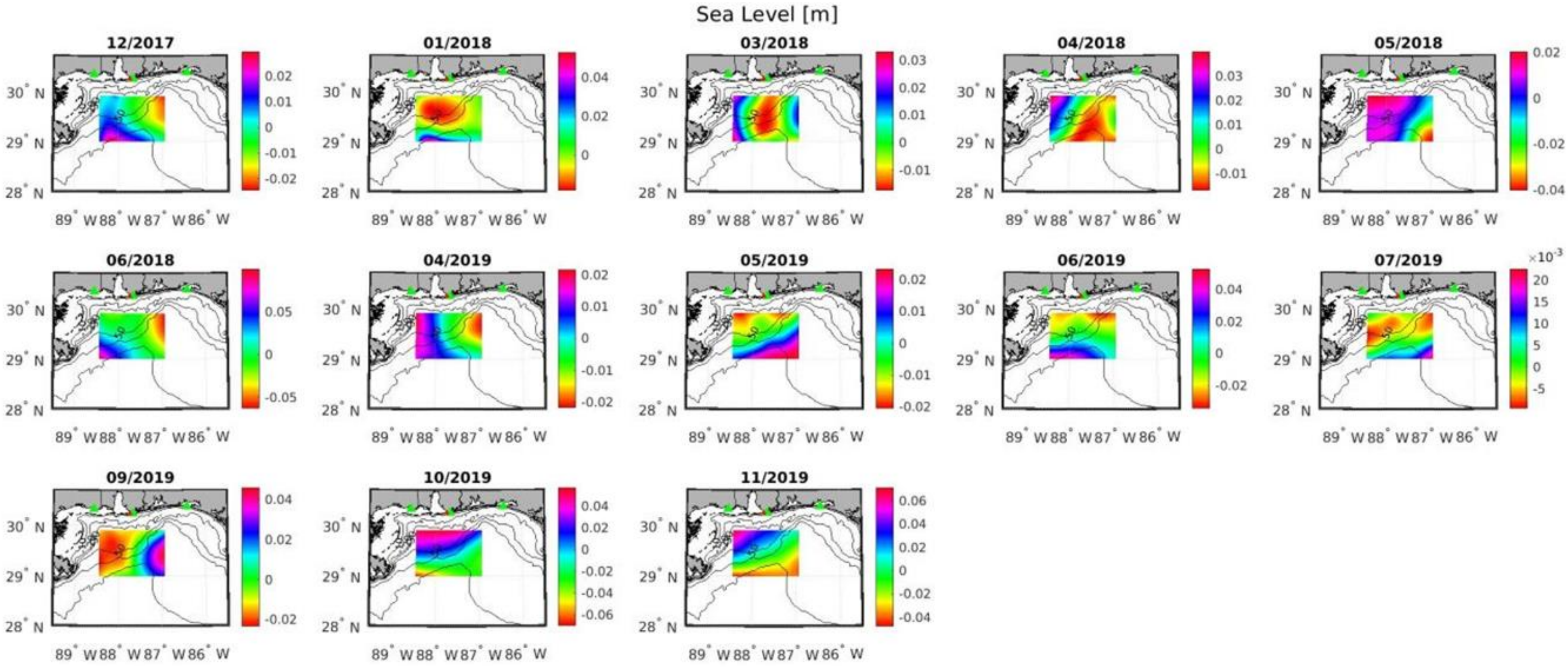

Figure 4.2 *Monthly mean HF radar SSHA*

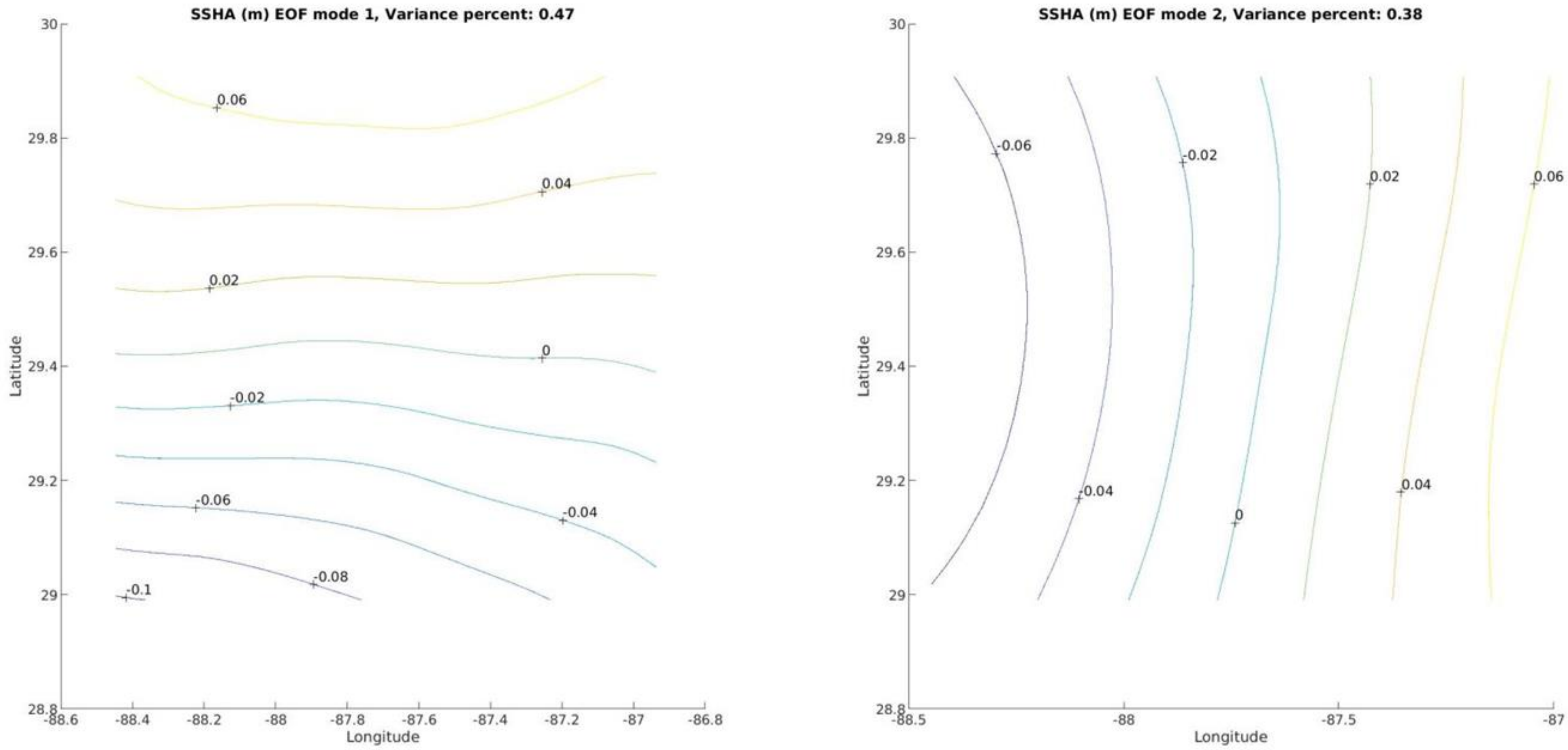

Figure 4.3 *First two empirical modes of the HF radar SSHA.*

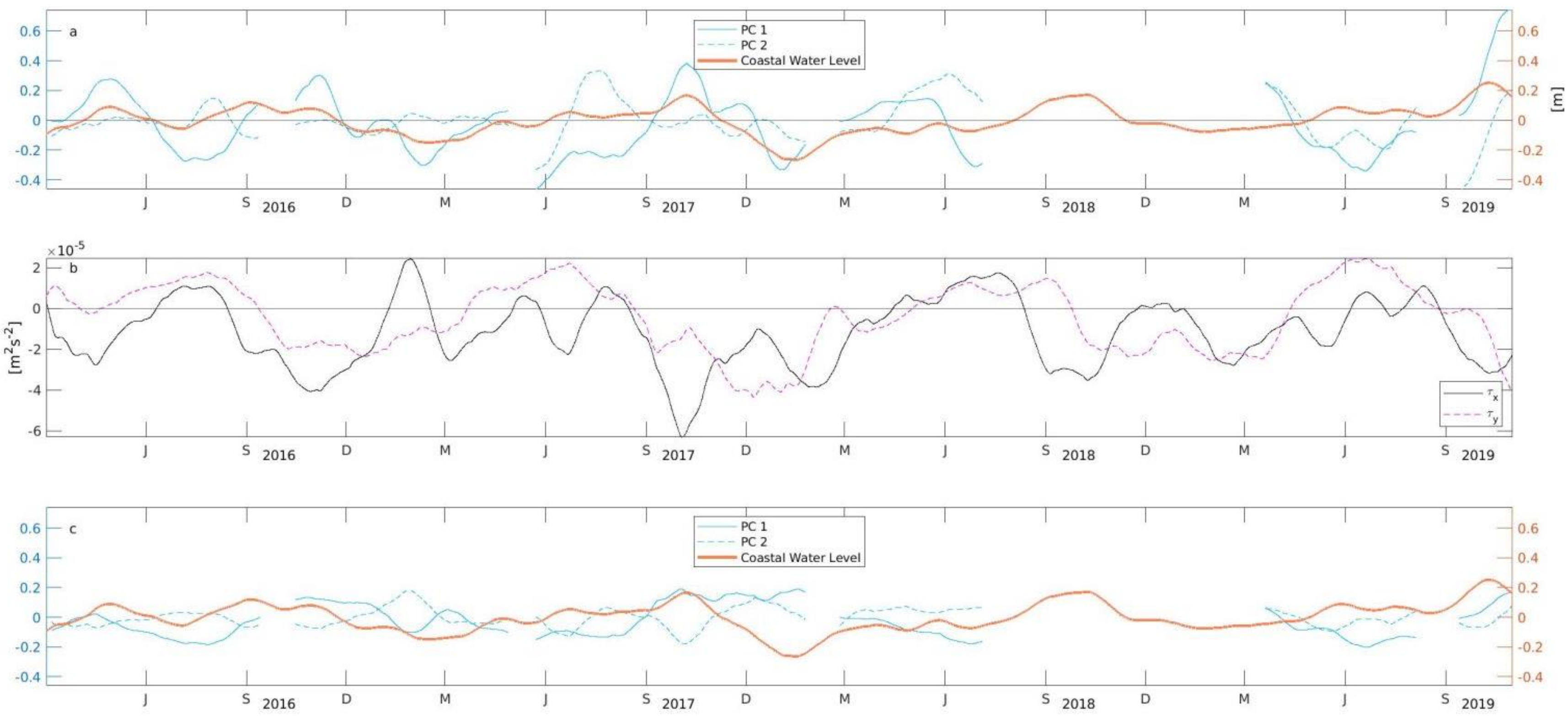

Figure 4.4 *(a) One month filtered mode 1 and 2 PC and Coastal Water Level. (b) One month filtered τ_x and τ_y.* *(c) Regression of Mode 1 and 2 PC and Coastal Water Level. The regression model explained 35% of the variability in the PCs. Here and in other cases, the horizontal axes represent time in seasons similar to the seasonal definitions by Dzwonkowski & Park, (2010): spring (March to May), summer (June to August), and fall (September to November) and winter (December to February).*

4.3.2 Wind Stress Relation to MSB Sea Level Gradient

Based on GOM wind monthly climatology, the magnitude of the southerly and northerly components dominate the easterly component in both summer and winter seasons respectively while in the fall and spring seasons, the easterly component dominates the northerly component (Johnson, 2008). The wind data was not entirely consistent with the GOM wind climatology as wind in the nGOM was westerly most of late spring and summer as indicated by positive τ_x (Fig. 4.4b). Additionally, τ_x was not strongly easterly in the spring season but it was in the fall season which is consistent with the climatology. τ_y was mostly consistent with GOM wind climatology as it was predominantly positive (southerly) in summer seasons and negative (northerly) in the other seasons.

The relationship between wind stress and subinertial currents used in estimating the HFR SSHA was determined. Based on the assumption that wind is spatially consistent in the study region, the spatial mean of the sub-inertial surface currents at all sampling times were computed. Using the resulting surface current time series, a significant correlation (0.60) between the wind stress and surface current was determined and the surface current was at 60^o angle to the right of the wind stress. As the study region was partitioned into inshore (regions inshore of the 50m isobaths) and offshore (regions offshore of the 50m isobaths), it resulted in different correlation coefficients and phase angles. The correlation increased while phase angle reduced (0.61 and 55^o respectively) when the inshore surface current data was used in the correlation computation. The result reversed (0.56 and 65^o respectively) when the offshore surface currents were used. The observed correlation between the current and wind stress indicated that there might be a relationship between the wind stress and sea level gradient.

Correlation between the wind stress components and PC1 and PC2 (Fig. 4.4a,b) were estimated to determine if the two were related. There is a significant negative correlation between PC2 and τ_x (-0.36) but the correlation between τ_y and PC2 is not statistically significant (-0.04). There is also significant negative correlations between PC1 and τ_x (-0.56) and between PC1 and τ_y (-0.42). When both components of the PCs and the wind stress were used in complex correlation computation, a significant correlation (0.37) was determined.

Having determined a significant correlation between both components of the wind stress and PCs, the proportion of the sea level gradient that is due to the contribution of wind stress was estimated from the regression model (Fig. 4.4c). While there is resemblance between the original PCs and regressed PCs, the magnitude of the regressed PCs are smaller compared to the original PCs. A notable difference between the two is in winter 2017 where PC1 was negative in the original time series but positive in the regressed PC1 time series. This was indications that all the variability in the PCs cannot be attributed to wind stress.

4.3.3 Influence of the LC System Including the LCFE MSB Sea Level Gradient

Over the study period, there were three cases of LC intrusion within ~200 km of the study region. In the first intrusion, the northmost margin of the LC was already in the specified region for LC identification as of February 1 2016. Figure 4.5b shows that the identified LCFEs were consistently to the north of the LC system throughout the first intrusion. Walker et al., (2013) also observed the LCFE around the LC margin. On 14

April 2016, a LCE separated from the LC. The LCE was circular in shape and propagated northwards as well as the LCFE north of its margin (Fig. 4.5a and Fig. 4.6a). The northmost position of the LCFE corresponded to positive PC1 (Fig. 4.5a). After a few days, the LCE propagated southwards alongside the LCFE. However, as the LCE drifted westwards and out of the specified region, the LCFE remained relatively stationary and its SSHA reduced.

The second intrusion commenced on 22 May 2017 and it was the longest among the three intrusions. As in the previous intrusion, LCFEs were around the margin of the LC system. As the LC margin progressed towards the north, an anticyclonic feature north of the LCFE split; one-half propagated towards the west while the other half remained northwest of the LCFE (Fig. 4.6b). Notice that PC1 was negative in the period when the anticyclonic anomaly was southeast of the study region, consistent with a high sea level to the south of the study area. The anticyclonic anomaly propagated in the southwest direction towards the 'bird foot river delta' as the intensity of the sea level anomaly diminished. Two anticyclonic formations detached from the LC that caused the LC to retract below 26^o N, hence the gap in Fig 5b during the second intrusion. The features were not identified because the SSHA was lower than +0.17 m. One of the two anticyclonic features propagated towards the west. The second anticyclonic anomaly propagated as far as 28.5^o N and was due south of the study area for most January 2018 (Fig. 4.6c). In that interim, PC1 was also negative as in the previous case when an anticyclonic formation was near the study area. The LC reattached to the anticyclonic formation as it crossed latitude 26^o N on December 31. Another anticyclonic feature (also not identified) detached from the LC on 15 February 2018 but it propagated towards the west. The northern margin of the LC retracted due to the detachment (Fig. 4.5a). A LCE eventually detached from the LC on 8 July 2018. It reattached three times to the LC before it separated on 28 October 2018. Between the first detachment and the separation of the LCE, a LCFE was always present to the north of the margin and both propagated towards the west and away from the specified area. Both the LCE and the corresponding LCFE did not travel as far north as in the first intrusion (Fig. 4.6d). Furthermore, the LCFE was smaller compared to the LCFE in the first intrusion.

On 13 January 2019, the northern margin of the LC crossed latitude 26° N during the third intrusion (Fig. 4.5a). Data gaps and artifacts, which resulted from data processing were present in the data between mid-April and early June and they made the analysis of the third intrusion challenging. On 13 July 2019, a LCE detached from the LC that caused the LC northern margin to retract about one degree south of 26° N (Fig. 4.6e). Unlike the previous intrusions, there was no cyclonic feature to the north of the detached LCE. PC1 was already negative before the detachment of the LCE. It was not clear if the LCE reattached to the LC as data gaps and data processing artifacts were presented (Fig. 4.6f) before the eventual westward propagation of the LCE.

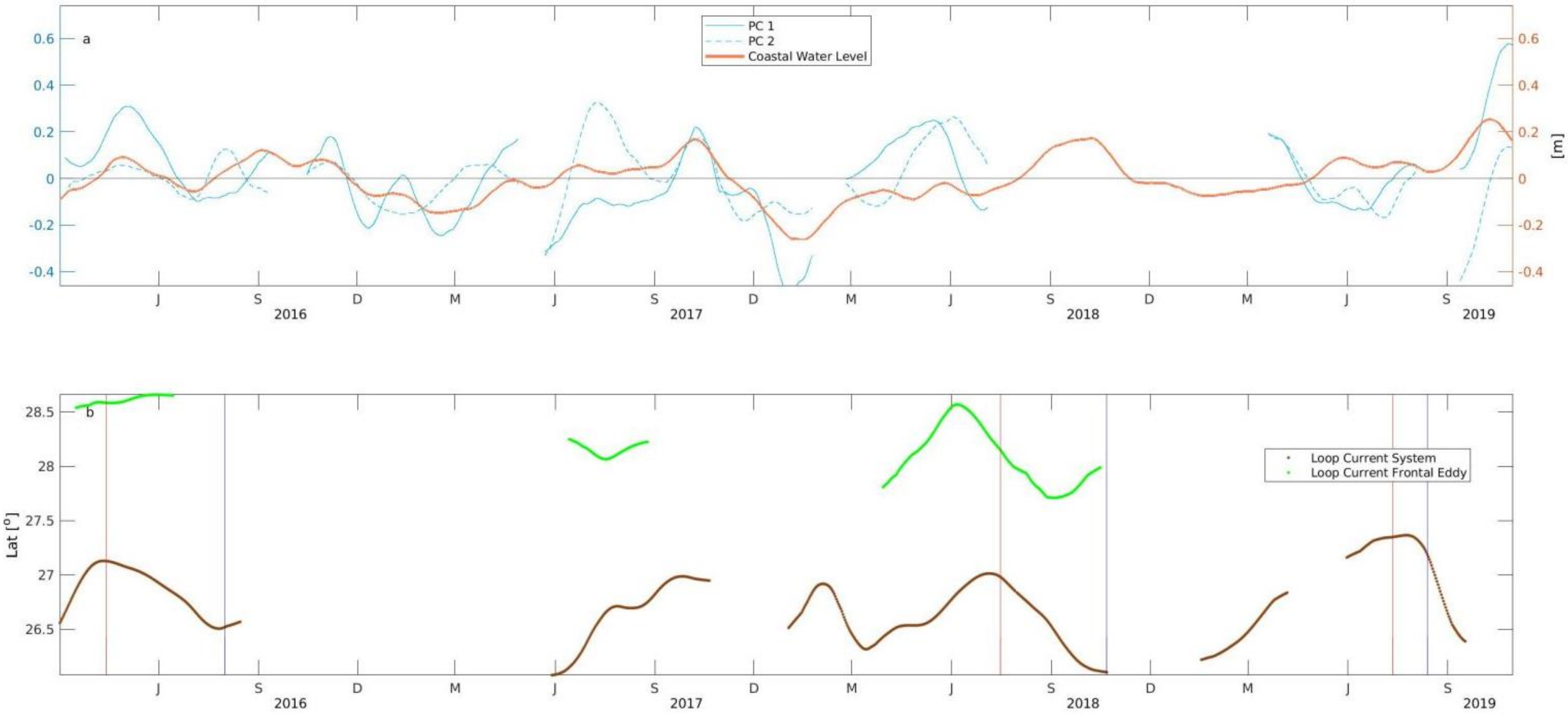

Figure 4.5 *(a) PC1 and PC2 residual after subtracting model generated PCs (Fig. 4.4c) from original PCs (Fig. 4.4a) and Coastal Water Level. (b) One month filtered northmost latitude of the LCFE and the LC system comprising of both the LC and LCE (vertical lines indicate detachment/separation of LCE (red) and reattachment or exit from the prescribed region for feature identification (blue)). The gaps in (b) were due to the absence of the LC, LCE and LCFE in the within the defined area for identification.*

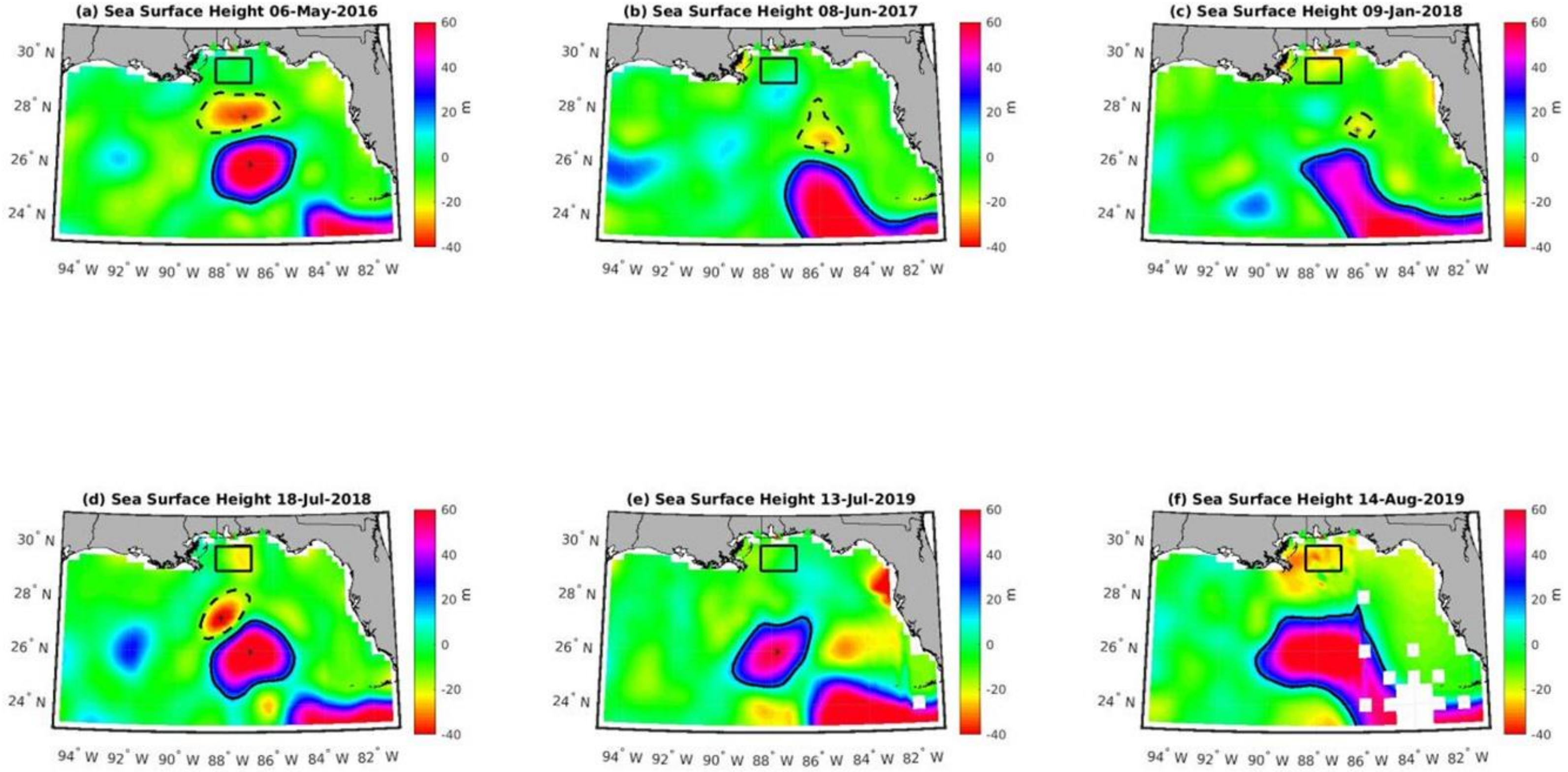

Figure 4.6 *Samples of the intrusions of the LC system (black solid contour) and the LCFE (black dash contour). The black rectangle represents the study area.*

4.3.4 Freshwater Discharge

Discharge data from the two freshwater sources provided some insights on how much freshwater was deposited into the GOM from the two sources over of the study period. Variability in MR discharge over the study period was between 41,000 m^3s^{-1} and 5000 m^3s^{-1}. Comparatively, MB discharge variability was smaller 100 m^3s^{-1} – 11,000 m^3s^{-1}. The largest and smallest discharge from both sources were in spring and fall respectively. Other pulses of peak discharge at both sources occurred in winter, spring and summer seasons (Fig. 4.7b).

Given that there was a sustained high discharge from MR between March and July 2019, this is a reasonable window to investigate the possible influence of MR discharge on sea level changes in the study area. The investigation was conducted using the results of the one-month filtered principal component 1 and 2 of the turbulent energy (Fig. 4.8), the monthly absorption coefficient of gelbstoff and detrital materials (Fig. 4.9) and HFR SSHA PC2. Aurin et al., (2018) suggested that gelbstoff is a viable tracer of freshwater discharge and that the concentration decreases towards offshore. Based on this, when there is an increase in the concentration of gelbstoff and detrital material from the inner shelf towards offshore it implies that at least a mechanism (discharge, wind, eddies) is responsible. Considering that several mechanisms can result in a gradient in turbulent energy, when the gradient in turbulent energy is towards the MR ’bird foot delta’ it could be attributed to the freshwater discharge from MR. Modes 1 and 2 of the turbulent energy show that such gradient was present (Fig. 4.8 a and b). A corresponding gradient was observed in the concentration of gelbstoff and detrital materials from March to July between the years of 2016 to 2019. Furthermore, if a pressure head developed by the MR discharge was in geostrophic balance, the signature should be present in the HFR SSHA PC2 (Fig. 4.7a); negative episodes of HFR SSHA PC2 lagging behind peak discharge periods (Fig. 4.7b). A lag between the two time series was expected because the discharge gauge was located at ~ 300-river mile. From Fig. 7a,b, almost all periods of negative HFR SSHA PC2 were after instances of peak discharge. It was unclear if the negative episodes of HFR SSHA PC2 resulted solely from the peak discharge. That notwithstanding, the instances of negative HFR SSHA PC2 occurrences suggested that there was a relationship between the two time series (HFR SSHA PC2 and MR discharge). However, the inconsistencies in the lag suggests otherwise as it ranged from 1 to 3 months (peak to peak). Moreover, the transition of HFR SSHA PC2 from negative to positive in 2019 irrespective of the sustained high discharge was another indication that there might be no relationship between the two time series. Besides hydrographic data limitation, activities of mesoscale processes in the region presented an additional challenge in estimating the potential contribution of MR discharge.

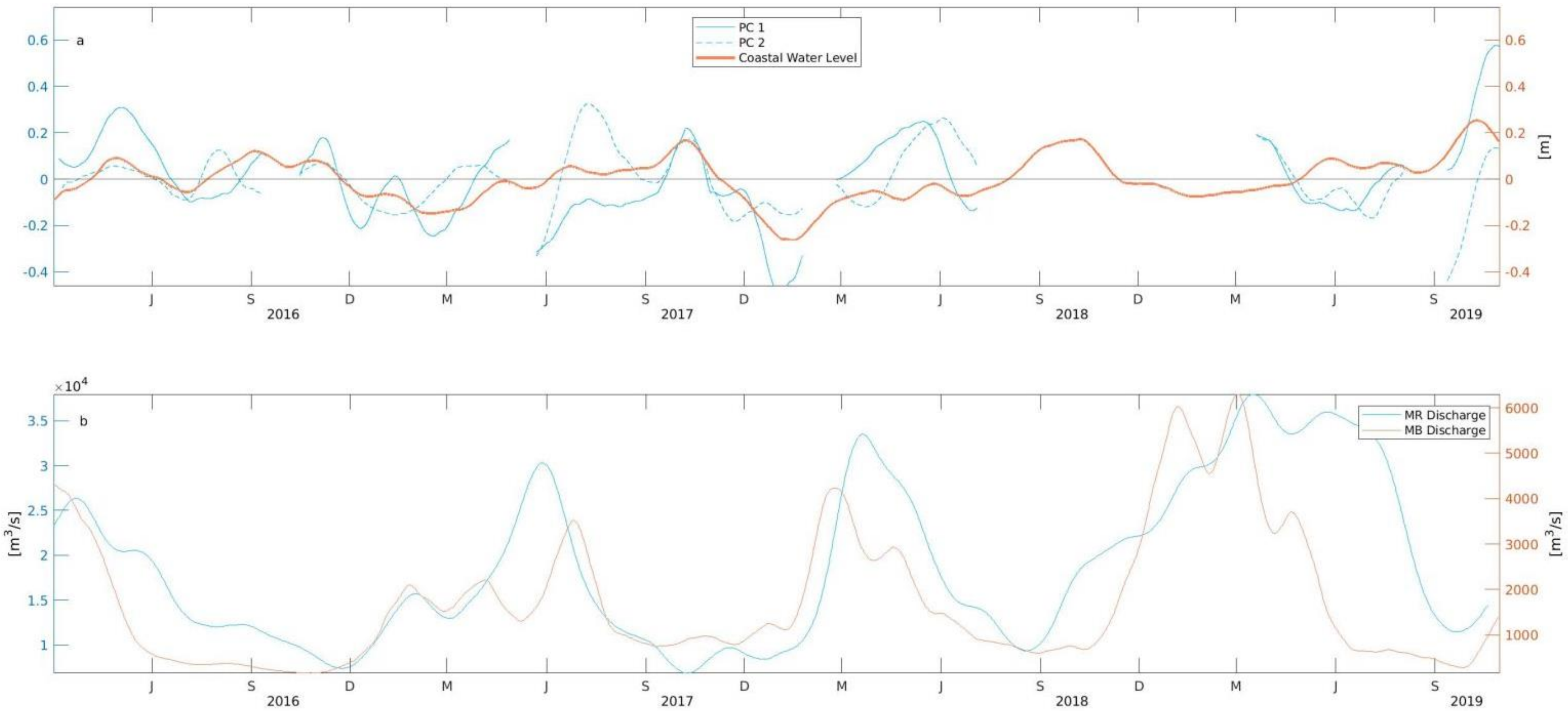

Figure 4.7 *(a) PC1 and PC2 residual after subtracting model generated PCs (Fig. 4.4c) from original PCs (Fig. 4.4a). (b) One month filtered daily discharge from Mobile Bay and Mississippi River.*

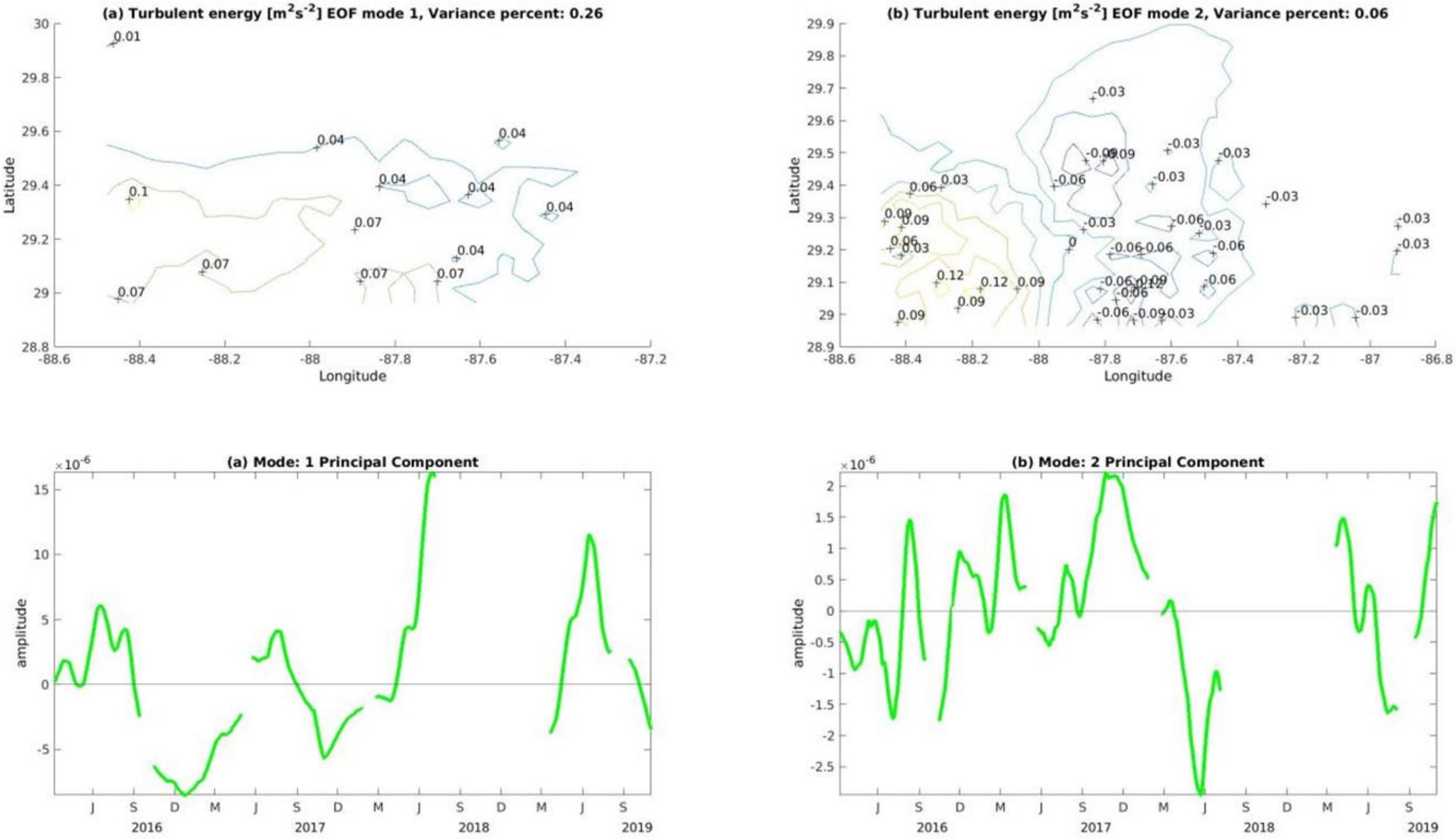

Figure 4.8 *First two empirical modes of turbulent energy.*

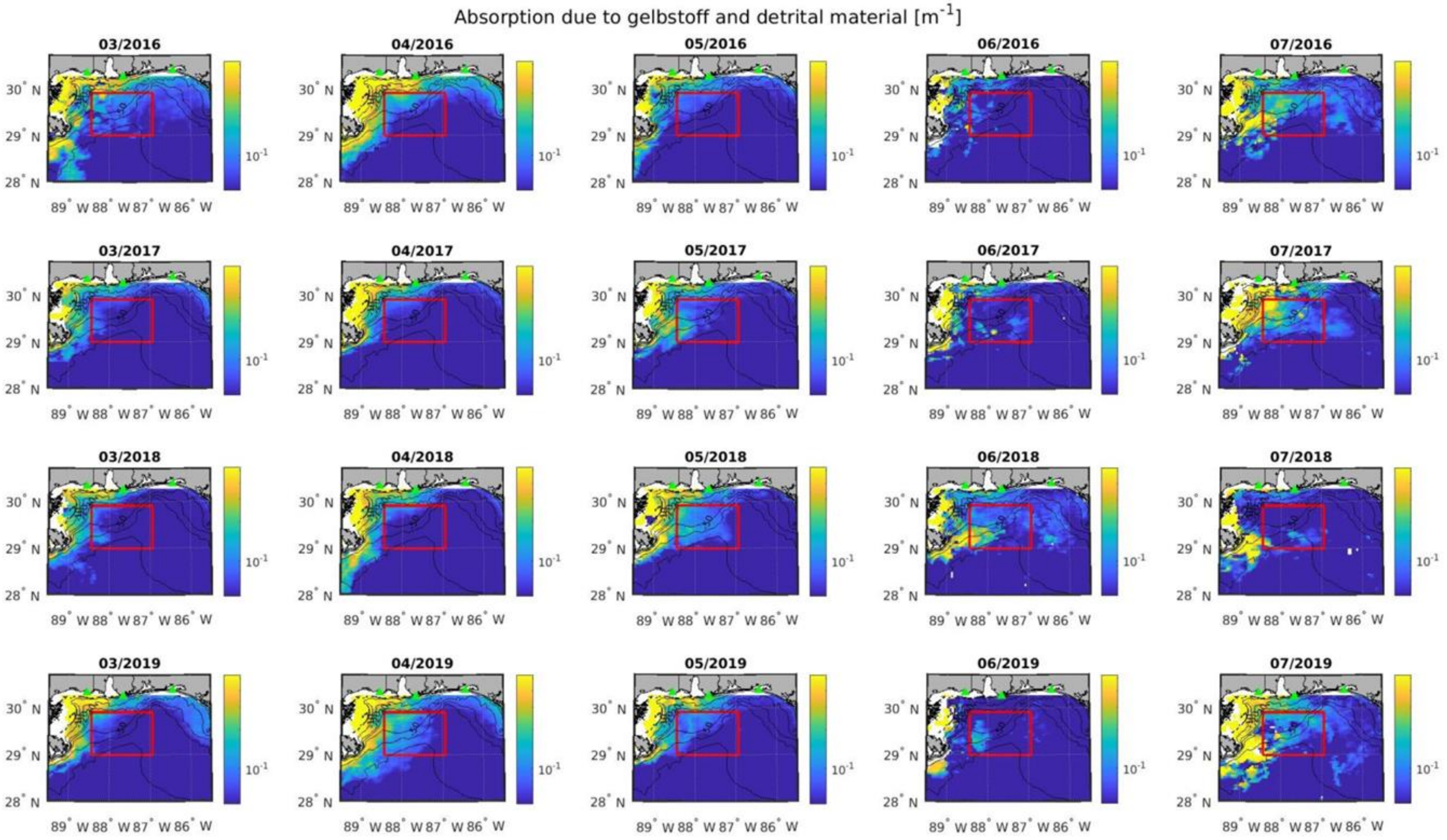

Figure 4.9 *Monthly mean of absorption coefficient due to gelbstoff and detrital materials for the months of March, April, May, June and July 2016-2019.*

The signature of the MB discharge was similar to that of MR discharge but smaller in magnitude (Fig. 4.4d). Focusing on periods of peak discharge and Figures 4.6 and 4.7, there was no feature present that suggested that MB discharge influenced the study region. Based on Dzwonkowski et al., (2015) definition of flood event at MB (discharge > 7000 m^3s^{-1}), the MB flooded in summer 2017, winter 2017/2018, winter 2018/2019 and spring 2019 and one can argue that these events, especially the flooding in March 2019, influenced the study area at shorter timescales. There was a gradient in the hourly turbulent energy between March 21 and 29, 2019 in the region of the domain close to the MB. However, there was no corresponding gradient in the daily gelbstoff and detrital material absorption coefficient to suggest that the feature was due to the discharge from MB. There was no relationship between MB discharge (Fig. 4.4d) and SSHA PC 1 (Fig. 4.4a) largely because MB discharge does not have a shelf-wide contribution. Its contributions are pronounced in the inner shelf region as noted in Dzwonkowski et al., (2015).

4.4 Discussion

Physics of the mechanism by which wind affects sea level is different at different temporal-spatial scales. During wind spin up at timescales shorter than the inertial period, wind sets the ocean surface in motion in the direction of the wind. It results in increase (decrease) in sea level at the coast if the wind flows towards (away from) the coast. The first order balance at that timescale is between the time derivative of the surface current and the vertical divergence of turbulent stresses. Additionally, there will be a momentum flux from the wind that leads to the increase in turbulent kinetic energy subsequently resulting in the formation of the turbulent boundary layer. Over an inertial period where the wind and acceleration are relatively constant, the surface boundary layer is expected to be fully formed and close to the coast a new balance is established and it becomes the balance between the pressure (sea level) gradient and wind stress terms. Walker et al., (2013) hinted at the phenomenon of coastal sea level gradient in the direction of the wind at the nGOM coast.

At timescales greater than the inertial period and assuming no bottom stress influence at the base of the fully formed surface boundary layer, there will be an Ekman transport if the depth of surface boundary layer is less than the water column. Ekman's theory assumes that if steady wind blows over a homogeneous fluid with no horizontal gradient in current, it results in the development of a surface boundary layer, and the vertically integrated transport in the boundary layer is 90^o clockwise to the direction of the wind in the northern hemisphere ("Ekman transport", Ekman, 1905). At the surface, the surface current will be at about $5^o – 20^o$ to the right of the wind stress (Cushman-Roisin & Beckers, 2012). The results of the correlation between the sub-inertial wind stress and surface current (positive and to the right of the wind stress vector) supports the Ekman transport phenomenon. However, the estimated phase angle between the two vectors was not consistent with the empirical results of $5^o – 20^o$ reported in Cushman-Roisin & Beckers, (2012). Nevertheless, previous studies such as Ardhuin et al., (2009) reported phase angles similar to the phase angles in this study. The potential reasons why the observed phase angles were not consistent with empirical phase angle results of Cushman-Roisin & Beckers, (2012) are that the surface currents estimated using HFR actually represented a depth-integrated currents over a depth layer of ~2 m, and the sub-inertial velocities which are not in Ekman balance are always present in the region.

The presence of a coastline to the right/left of the wind direction, will potentially enhance the sea level gradient as the Ekman transport towards/away from the coast. For the nGOM region under consideration, zonal wind can be considered as along-shelf wind with respect to the northern boundary. For negative τ_x (wind flowing towards the west), there will be an Ekman transport towards the northern coast which will result in sea level gradient towards the coast (positive PC1) at sub-inertial scales. The gradient is expected to reverse as the direction of τ_x reverses. The anti-correlation between τ_x and PC1 indicated that the Ekman transport due to τ_x sets up sea level gradient in the north-south orientation of the region. Dzwonkowski & Park, (2012) reported this type of Ekman dynamics in the coastal region north of the study area. At the timescales considered in this study, the established sea level gradient due to Ekman transport underwent geostrophic adjustment. Therefore, this resulted in a local geostrophic balance. The resultant current in geostrophic balance with the sea level gradient will be in the direction of the wind stress. The anti-correlation between τ_x and PC2 was not consistent with the findings that along-shelf pressure gradient force acted in the opposite direction to τ_x as reported in Dzwonkowski & Park, (2012). Dzwonkowski & Park, (2012) attributed the relationship to the ~ 90^o change in bathymetry west of the study area as noted by Yankovsky, (2015) in cases of such changes in a coastline. The change in bathymetry explains why a positive correlation between τ_y and PC2 considering the Ekman dynamics was not observed. The negative correlation between τ_y and PC1 is physically not feasible. The reason is, if τ_y had played a significant role in the setup of a north-south sea level gradient, it should result in a positive correlation instead of a negative correlation. Similarly, the negative correlation between τ_x and PC2 is also not physically feasible and this further indicated that other mechanisms besides wind stress play some role in the sea level gradient over the study area.

The result from the regression model was a further indication that the temporal variability of PCs was not entirely due to the contribution of the wind stress as ~1/3 of the variability in the PCs was explained by the wind stress. As such, the other mechanisms were investigated to determine how they contributed to the discrepancies.

A qualitative approach was adopted in the investigation of the contribution of the LC to the residual PC. Unlike in Sturges & Evans, (1983), the time series of this study is too short to quantitatively determine the contribution of the LC based on the variability of the LC. In a different study, Li & Clarke, (2005) did not quantitatively determine the variability in the coastal sea level on the WFS due solely to the LC. Li & Clarke, (2005) rather attributed the trend in the EOF of the interannual sea level variability on the WFS to the interannual LC intrusion based on the coherence between the two at the interannual scale that was reported in Sturges & Evans, (1983). Even in this study, while the intrusions of the LC towards the nGOM have been described, the exclusive contributions of the LC to sea level gradient in the study area was not quantitatively determined. The LC exhibits both barotropic and baroclinic instabilities (Donohue & Watts, 2016). The development of these instabilities enhance the northward intrusion of the LC. Besides the northern boundary, the detachment and separation of the LCE limits the northward propagation of the LC towards the northern shelf of the nGOM to about ~28º N (Sturges & Evans, 1983; Donohue & Watts, 2016). Ohlmann et al., (2001) highlighted that momentum flux and the setup of sea level gradient are the techniques by which the LC contributes to the GOM circulation. The proximity of both the LC system and the LCFE to the study region as well as the size of the LCFE north of the LC during the first LC system intrusion suggests that the LC system remotely influenced sea level gradient of the study area. The LCFE was the largest (~130 km (north-south), ~300 km (west-east)) when compared to the LCFEs during the other LC intrusion cases and it was directly south of the study area. Northward intrusion of the LC system enhanced the northward intrusion of the LCFE. The southward boundary of the study area is ~ 29^o N and from Fig. 4.4b, the LCFE was ~ 50 km (~0.5^o latitude) away from entering directly the study region. The LC was reported to have an influence over a similar distance despite the shoaling bathymetry of the west Florida shelf constraining the intrusion of the LC according to the Taylor Proudman theorem (He & Weisberg, 2003a). Hence, at such size and proximity from the study area, the LCFE is not only expected to result in the momentum flux towards the study region but also should setup a sea level gradient towards the coast. It is consistent with the south-north sea level gradient observed in the monthly sea level plots for April and May 2016 as well as the positive residual PC1 for the same period when the LCFE was south of the study area.

Unlike the wind stress and LC system, there was no discernable contributions from MB and MR to the patterns in PC1 and PC2. Fresh and oceanic water are separated by a front or series of fronts. If the variability of the rim current along the frontal zone is small, a geostrophic balance will prevail especially when the fresh water plume is large compared to the internal Rossby Radius of Deformation of the region. This will be captured in the current data when the plume propagates into the HFR domain and the signal will be obvious in the estimated sea level gradient if it is large enough. However, for fast and large current variability over the frontal zone, the geostrophic balance may not establish. Consequently, there will be no observed influence of fresh water discharge to the patterns of the sea level gradient. Unlike the MR, there was no observed feature, which suggests that the MB influenced the study area and this was largely due to the characteristics of MB. The freshwater plume from MB alongside the associated rim current are mostly localized to the inner shelf as shown in Dzwonkowski et al., (2014) and Dzwonkowski et al., (2015) otherwise the turbulent energy EOF would have revealed a seasonal signal in the north of the study area. Given that the MB peak discharge was one order of magnitude less than MR discharge, this explains why the plume does not propagate much into the mid-shelf due to the momentum of the discharge. Dzwonkowski et al., (2015) showed that the structure of the freshwater plume from MB is not sustained as discharge decreases and also due to the influence of wind. They further noted that the along-shelf component of the wind propagates the plume towards either the west or east depending on the prevailing wind direction and predominantly in the inner shelf region. The EOF of the turbulent energy suggests that the discharge from MR influenced the dynamics of the study area as the gradient in the turbulent energy was towards the southwest. The gradient in turbulent energy formed due to the velocity shear that resulted from the freshwater front that propagates into the study area because of the high MR momentum. Considering Dzwonkowski et al., (2015, Fig, 3) where sea level in the Bay slightly increased in response to increased discharge, a similar response is expected in the vinicity of the mouth of the MR during peak discharge and this would result in the increased river discharge momentum. However, the pressure head that developed during MR peak discharges was localized to the inner shelf which seem to be the reason why there was no observed contribution to the patterns of the estimated sea level gradient.

The discussed mechanisms (LC + LCFE, wind stress, freshwater discharge) did not completely explain the patterns in the estimated sea level gradient. Besides freshwater discharge, the LC system had a limited influence on the sea level gradient and the contribution of the Ekman transport to the formation of sea level gradient was not consistent throughout the entire time series. Hence, other mechanisms that were within and/or offshore of the study area but were not accounted for in this study contributed to the sea level gradient. Wind stress was the major mechanism that influenced the observed patterns but the magnitude was the least in spring 2018 when compared to other periods. Thus, the unaccounted mechanisms dominated and influenced the patterns in sea level changes. In June 2017 and winter 2017/2018, the magnitude of wind stress was relatively nominal but, wind stress was not the dominant mechanism responsible for the patterns observed in PC1. In both cases, an anticyclonic anomaly was present offshore of the study region (Fig. 4.5b,c) and both had different sizes and proximities to the study area. Though it was unclear if the anticyclonic formation observed in June 2017 solely influenced the pattern in sea level changes, the corresponding monthly mean of the sea level changes for June 2017 as well as the negative PC1 were consistent with the expected sea level gradient (high sea level anomaly offshore). A similar pattern in the monthly mean sea level anomaly was observed in winter 2017/2018 and it was unlikely due to the anticyclonic feature which was smaller in size and further away from the study area. There was a breakdown in the negative correlation between the along-shelf wind stress and the coastal sea level time series which suggests that the contribution of another mechanism to the sea level gradient prevailed over the contribution of wind stress. The mechanism potentially responsible for the observed pattern was a cyclonic anomaly, which propagated into the study area from the DeSoto canyon while hugging the northern coast. Though sea level anomalies from the coastal sea level time series were consistently negative in the winter season, the presence of the cyclonic feature was potentially responsible for the peak negative anomalies observed in winter 2017/2018 (Fig. 4.4a). Furthermore, though the SSH from the gridded satellite altimeter product for the study area was ignored, negative SSH was observed close to the coast (Fig. 4.5c) which further supports the contribution of the cyclonic formation.

CHAPTER V – CONCLUSION

This dissertation is comprised of three studies carried out to characterize sea level along the Louisiana/Florida Shelf. These studies were intended to fill some gaps on the limited sea level studies on the Louisiana/Florida shelf.

In the first study, errors in the NOAA's VDatum tool in the nGOM were estimated using a novel technique, which involved USGS sea level data that were not intended for geodesy or tidal applications while testing hypothesis 1. The study focused on the southeast coast of Louisiana, where NOAA tidal observations and geodetic data are poor leading to the large uncertainties in VDatum (Yang et al., 2010). In this region, including western coastal Mississippi, NOAA warns that VDatum uncertainties may be as high as 0.20–0.50 m (https://vdatum .gov). The study demonstrated that by utilizing coastal USGS sea level gauges and a HydroLevel buoy, VDatum values could be checked against independent data. Even while uncertainties were considered, discrepancy in Gt at Delacroix was attributed the tidal modeling range errors. This supports the first hypothesis that the model used to develop VDatum in the region did not accurately simulate the spatial variabilities of the various mean tidal ranges. Furthermore, when the separation with respect to the ellipsoid of all tidal datums is larger than tidal datums estimated in this study and DTL discrepancy was not within VDatum uncertainty as in the case of Chandeleur East buoy, it was an indication of error in TSS, which resulted from subsidence. Considering that the buoy was in the VDatum large uncertainty region indicated by NOAA, the result supports the second hypothesis that subsidence played a major role in the VDatum large uncertainties. In future updates of VDatum in this region, these types of data could be used to produce a more accurate product.

Importantly, although subsidence is significant in this region (Shinkle and Dokka, 2004; Yang et al., 2010), performing GNSS surveys at sea level gauges, or from buoys, and running tidal datum transfers over observations periods shorter than the 19-years period produce geodetic heights of tidal datums that are not affected by further subsidence. In a more general context, it would be advantageous to treat the NAD83(2011) ellipsoid as the primary reference (a virtual primary bench mark) for tide gauges in the United States. This also has the advantage of removing the problem associated with subsidence or uplift of physical benchmarks corrupting tidal datums at decommissioned tide gauge sites.

The second study was focused on the shelf of MSB where the second and third hypotheses were addressed. From the diagnostics of the terms in the momentum equation, it was noted that geostrophic balance was the dominant balance at subinertial scales hence, other terms in the momentum equation can be neglected. The results of this study validated the second hypothesis; geostrophic balance is the dominant balance for subinertial currents in MSB. Furthermore, the study highlighted the benefits of having HFR stations along the coast as the data can be used to describe circulation of a domain as well as the sea level changes. The mapped sea level anomalies over the HFR coverage in MSB were estimated using a novel technique involving Least Squares. This is the first high resolution (temporal and spatial) mapped sea level estimates over the MSB, other than the gridded sea level estimates derived from coarse (spatial and temporal) satellite altimetry data. The study went on to show that the sea level anomalies on MSB have two major empirical modes, which supports the third hypothesis that there are dominant empirical modes in MSB sea level gradient. Ohlmann et al. (2001) argued that using

SSHA data from satellite altimetry, viable information such as shelf rise flow due to eddies at the shelf rise can be obtained. They further stated that the data could be assimilated in models and also used to validate models. The results of this project provides similar oceanographic outputs to satellite altimetry but at better temporal and spatial resolutions. Though the along-track satellite altimeter has an equivalent along-track spatial resolution, it does not adequately provide adequate 2-dimensional spatial information of oceanographic processes such as eddies. Consequently, SSHA from the HFR can be used to effectively validate SWOT altimeter data. The major drawback in using HFR SSHA is the unknown time dependent vertical offset. In future studies, a survey grade buoy will be deployed in the domain of the HFR coverage to estimate absolute HFR SSHAs.

The novelty of the third study is in the estimation of the contributions of the LC system, wind-stress, and freshwater discharge to the patterns in the MSB sea level changes estimated in the second study. The northmost propagation of the LC system including the LCE northern margin was 27.5^{o} N latitude, which is about ~250 km from the study area. From the study, it was determined that the LCFE influences sea level changes in the study area when the size of the LCFE is comparable to the study area and when its proximity is ~ 50 km away from the study area. It was also determined that the intrusion of the LFCE towards the northern shelf of the nGOM was enhanced by the LC system. The consistency between PC 1 and LCFE during the first LC system intrusion indicates that the LC system remotely influences SSHA on the shelf of MSB. That rejects the fourth hypothesis of the dissertation that the LC system does not remotely influence sea level changes on the shelf of the MSB. The study also showed that wind-stress played majority of the role in the pattern of sea level gradient through Ekman transport which set-up or set-down sea level in the north-south orientation. Wind stress explained one-third of the variability in the sea level gradient. While there were signals, which showed that freshwater discharge especially from MR propagated into the study area, there was no evidence of significant influence from freshwater discharge from both freshwater sources that were considered. Cyclonic formations within the study area were accounted. However, from the result of the study, the contributions of these features can dominate the contribution of wind stress to the sea level gradient of the study area. This was consistent with Ohlmann et al., (2001) who reported that GOM eddies were as important as wind stress when considering the circulation in the GOM. In future studies, in-situ data from moored ADCP and hydrographic data will be used to validate the remotely sensed data used in this study.

APPENDIX A – Gauss-Markov Estimator

Gauss-Markov interpolation technique is the statistical approach (Drygas, 1983) utilizing correlation between observed (data) and missing values (data gaps). Missing values are recovered according to (Eqn. A1):

$$u' = R_{ud}R_{dd}^{-1}\, d' \qquad \text{Eqn. A1}$$

where R_{ud} is covariance matrix describing the covariance between unknown velocity and data, R_{dd} is covariance matrix describing the data covariance. Both matrices were built under the assumption of isotropicity and homogeneity. d' is data deviation from the mean field and u' is velocity anomaly with respect to the mean at the location of data gap. A simple Gaussian model for isotropic and homogenous correlation function was fitted to the mean covariance matrix estimated from the observed data. Kim, (2010) adopted similar approach. The correlation function model was assumed to be isotropic and homogeneous in both time and space (Eqn. A2):

$$Rdd^{-1} = \left(0.5\left(\mathrm{e}^{-\left(\frac{r^2}{\delta^2}\right)}\mathrm{e}^{-\left(\frac{\tau^2}{T^2}\right)}\right) + 0.5\right) \qquad \text{Eqn. A2}$$

where r and τ are the spatial and temporal distances respectively between the gap grid point and the grid point of available data while δ (3.6 km and 4.72 km for respective u and v velocity components) and T (4 hr for time) are the typical correlation scales in space and time respectively. Due to the magnitude of data gaps leading to insufficient statistics, some gaps remained even after the interpolation processes.

APPENDIX B – Optimal Wind Estimation

Wind speed and direction from the wind data were converted from meteorological direction convention (direction wind comes from) to oceanography direction convection (direction wind is flowing towards) using (http://colaweb.gmu.edu/dev/clim301/lectures/wind/wind-uv) to estimate wind velocity vectors. Complex correlations using Kundu, (1976) (Eqn. B1) between the wind data at the various stations were calculated for the entire time series

$$\mathrm{r} = \frac{< \mathrm{u}_1\mathrm{u}_2 - \mathrm{v}_2\mathrm{v}_1 >}{< \mathrm{u}_1^2 + \mathrm{v}_1^2 >^{1/2} < \mathrm{u}_2^2 + \mathrm{v}_2^2 >^{1/2}} + \mathrm{i}\frac{< \mathrm{u}_1\mathrm{v}_2 - \mathrm{u}_2\mathrm{v}_1 >}{< \mathrm{u}_1^2 + \mathrm{v}_1^2 >^{1/2} < \mathrm{u}_2^2 + \mathrm{v}_2^2 >^{1/2}} \qquad \text{Eqn. B1a}$$

$$\alpha_{\mathrm{av}} = \tan^{-1}\frac{< \mathrm{u}_1\mathrm{v}_2 - \mathrm{v}_1\mathrm{u}_2 >}{< \mathrm{u}_1\mathrm{u}_2 + \mathrm{v}_1\mathrm{v}_2 >} \qquad \text{Eqn. B1b}$$

where r is the correlation coefficient, (u_1,v_1) are the components for vector 1 which serves as the reference, (u_2,v_2) are the components for vector 2, α_{av} is the average phase angle between the vectors 1 and 2, $i = \sqrt{-1}$ and < > denotes averaging over a time period which in our case corresponded to the entire time series period. Based on table B1, the smallest correlation coefficient between the wind stations was 0.66% and it was between the furthest stations. Correlation coefficients between the other stations were above 0.7, which indicated that wind was well correlated and had relatively insignificant variability for the region. Wind data from station 42012h was adopted as the optimal wind data as it not only correlated best with the wind stations but also had the second least gaps after dpia1h. Gaps in the optimal wind data were filled using wind data from station 42040h and if the data was also missing then data from dpia1h was used while correcting for vector rotation using (Eqn. B2).

$$\mathrm{OWD} = (\mathrm{u} + \mathrm{iv})\mathrm{e}^{\mathrm{i}\alpha_{\mathrm{av}}} \qquad \mathrm{Eq.\,B2}$$

where OWD means optimal wind data, (u,v) are velocity components from wind stations 42040h or dpia1h, e is exponential, α_{av} is the average phase angle between wind station 42012h and wind station (42040h or dpia1h) and i = √-1.

Table B.1 *Relative correlation coefficients and angle between wind stations*

Correlations coefficient between wind stations of the total time series				
Wind stn	42012	42039	42040	dpia1
42012	1	0.72, 0.64	0.84, -0.53	0.86, +3.92
42039	0.72, -0.64	1	0.79, -3.32	0.66, +3.57
42040	0.84, +0.53	0.79, +3.32	1	0.77, +5.27
dpia1	0.86, -3.92	0.66, -3.57	0.77, -5.27	1

APPENDIX C Statistics of Terms in the Momentum Equations

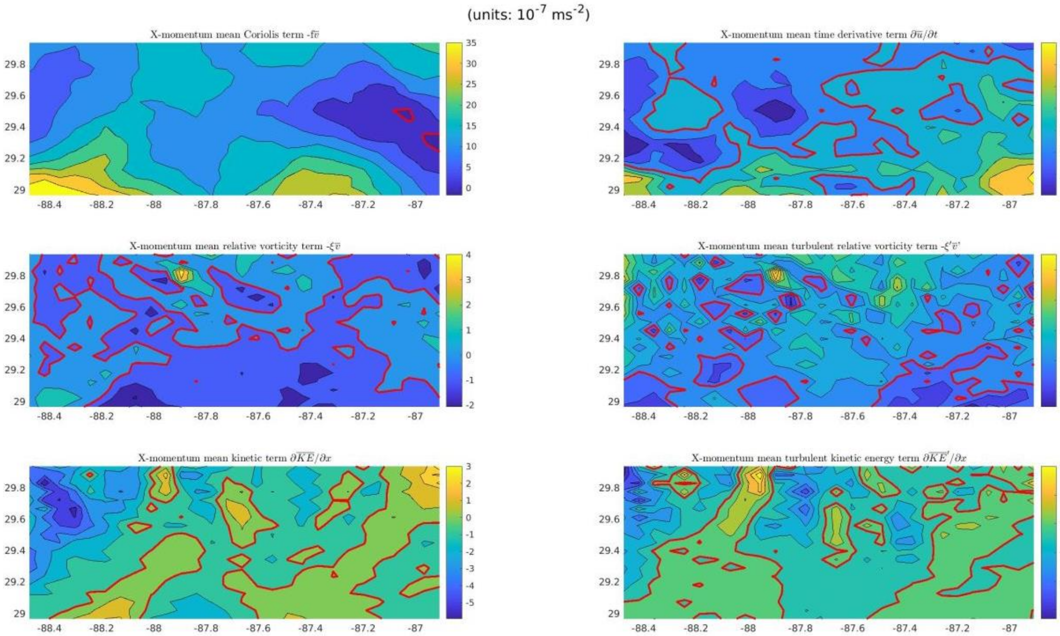

Figure C.1 *Mean values of the X-momentum components across the HF radar domain excluding the wind stress term.*

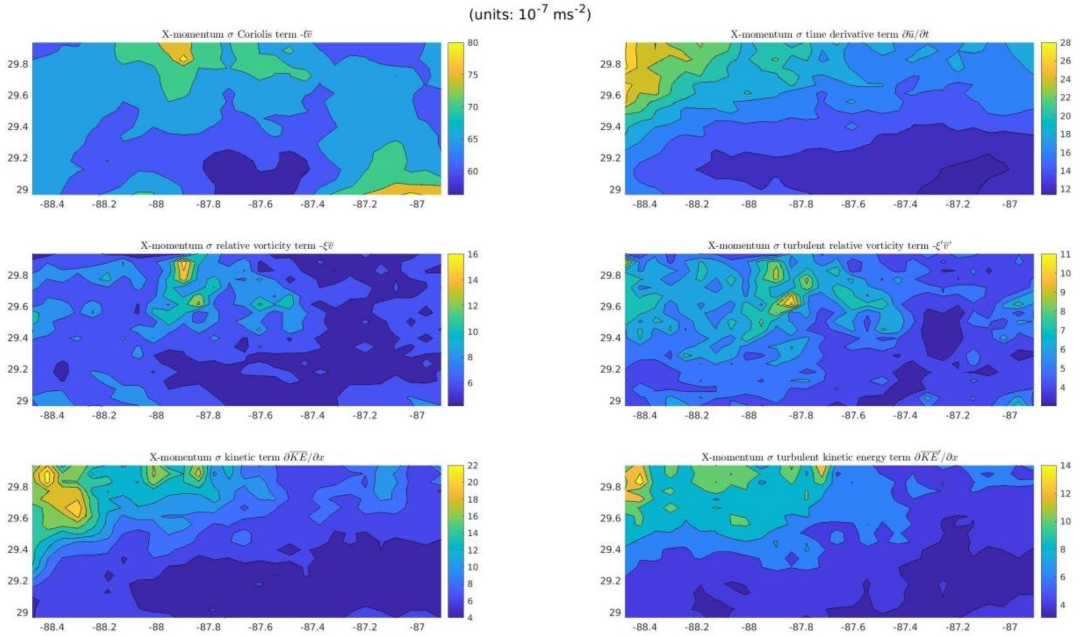

Figure C.2 *Standard deviations of the X-momentum components across the HF radar domain excluding the wind stress term.*

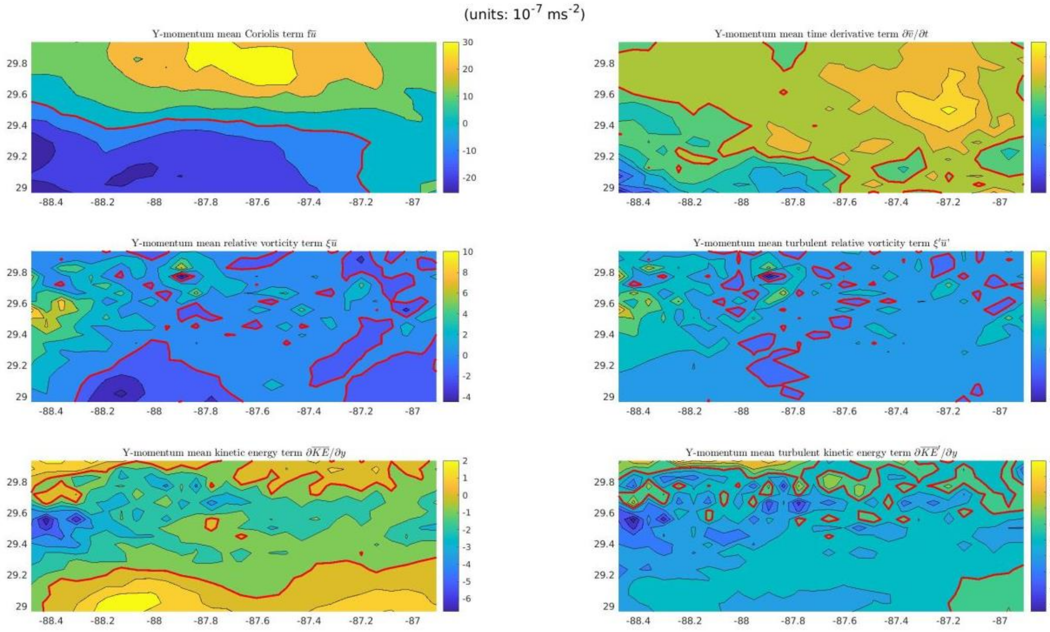

Figure C.3 *Mean values of the Y-momentum components across the HF radar domain excluding the wind stress term.*

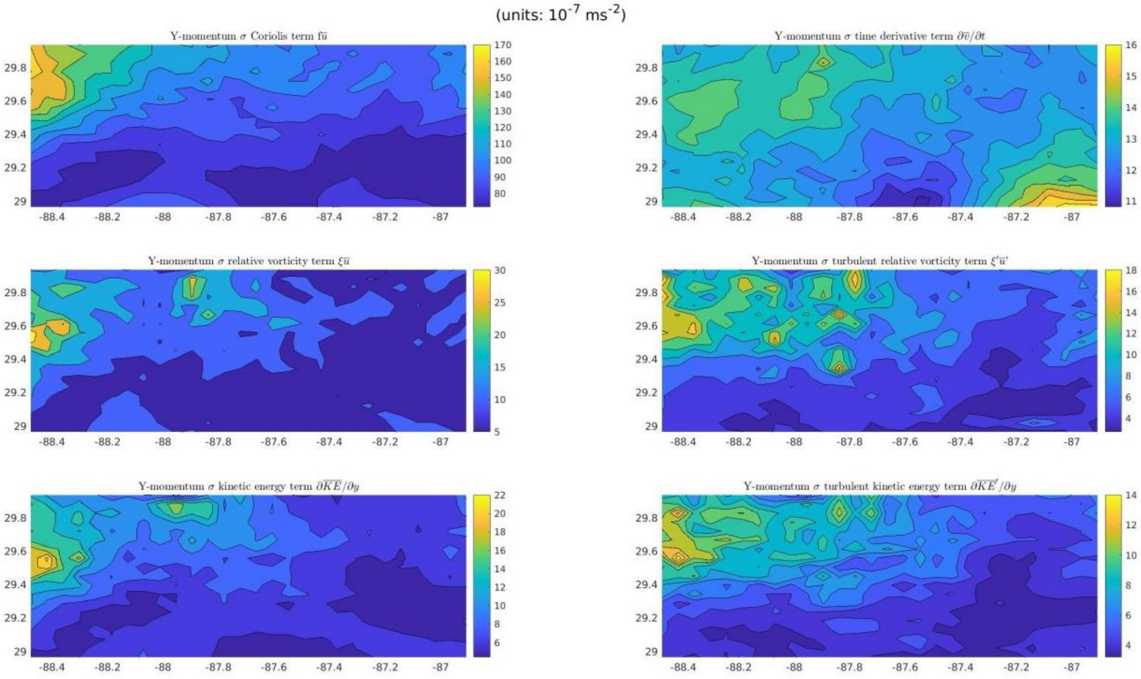

Figure C.4 *Standard deviations of the Y-momentum components across the HF radar domain excluding the wind stress term.*


Pass 93 time Jul-02-2016 rmsd: ± 0.03
Pass 93 time Jul-29-2016 rmsd: ± 0.04
Pass 93 time Aug-25-2016 rmsd: ± 0.02
Pass 93 time Oct-18-2016 rmsd: ± 0.03
Pass 93 time Nov-14-2016 rmsd: ± 0.04
Pass 93 time Dec-11-2016 rmsd: ± 0.02
Pass 93 time Jan-07-2017 rmsd: ± 0.03
Pass 93 time Mar-02-2017 rmsd: ± 0.03
Pass 93 time Mar-29-2017 rmsd: ± 0.03
Pass 93 time Apr-25-2017 rmsd: ± 0.04
Pass 93 time May-22-2017 rmsd: ± 0.05
Pass 93 time Jun-18-2017 rmsd: ± 0.07
Pass 308 time Jul-09-2016 rmsd: ± 0.02
Pass 308 time Aug-05-2016 rmsd: ± 0.03
Pass 308 time Sep-01-2016 rmsd: ± 0.04
Pass 308 time Oct-25-2016 rmsd: ± 0.01
Pass 308 time Nov-21-2016 rmsd: ± 0.04
Pass 308 time Dec-18-2016 rmsd: ± 0.03
Pass 308 time Jan-14-2017 rmsd: ± 0.03
Pass 308 time Mar-09-2017 rmsd: ± 0.01
Pass 308 time Apr-05-2017 rmsd: ± 0.02
Pass 308 time May-02-2017 rmsd: ± 0.05
Pass 308 time May-29-2017 rmsd: ± 0.02
Pass 308 time Jun-25-2017 rmsd: ± 0
sea level anomaly m
Latitude
0.1
0
-0.1
-0.2
29.1
29.2
29.3
29.4
29.5
29.6
29.7
29.8

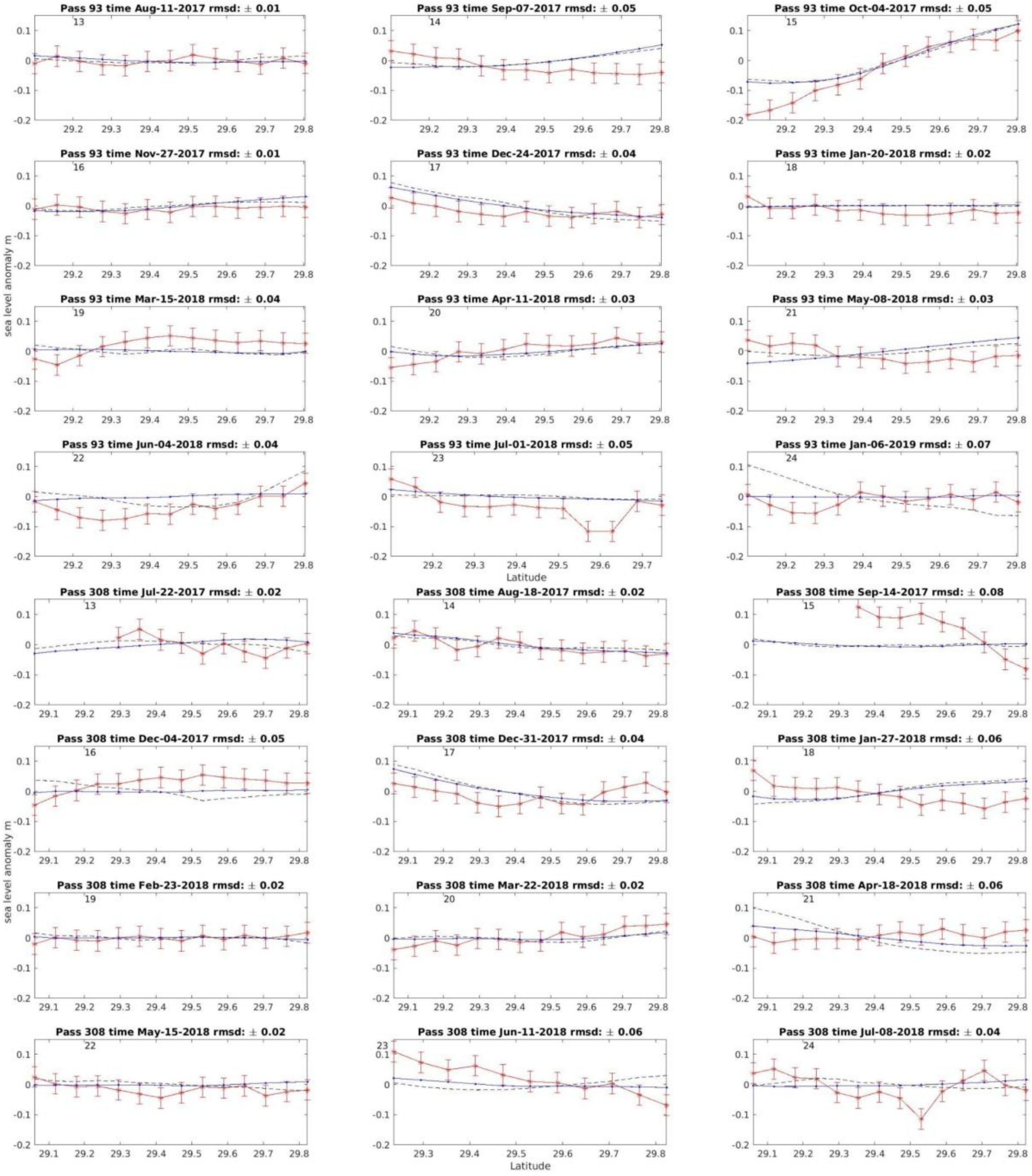
Pass 93 time Aug-11-2017 rmsd: ± 0.01
13
Pass 93 time Sep-07-2017 rmsd: ± 0.05
14
Pass 93 time Oct-04-2017 rmsd: ± 0.05
15
Pass 93 time Nov-27-2017 rmsd: ± 0.01
16
Pass 93 time Dec-24-2017 rmsd: ± 0.04
17
Pass 93 time Jan-20-2018 rmsd: ± 0.02
18
Pass 93 time Mar-15-2018 rmsd: ± 0.04
19
Pass 93 time Apr-11-2018 rmsd: ± 0.03
20
Pass 93 time May-08-2018 rmsd: ± 0.03
21
Pass 93 time Jun-04-2018 rmsd: ± 0.04
22
Pass 93 time Jul-01-2018 rmsd: ± 0.05
23
Pass 93 time Jan-06-2019 rmsd: ± 0.07
24
Pass 308 time Jul-22-2017 rmsd: ± 0.02
13
Pass 308 time Aug-18-2017 rmsd: ± 0.02
14
Pass 308 time Sep-14-2017 rmsd: ± 0.08
15
Pass 308 time Dec-04-2017 rmsd: ± 0.05
16
Pass 308 time Dec-31-2017 rmsd: ± 0.04
17
Pass 308 time Jan-27-2018 rmsd: ± 0.06
18
Pass 308 time Feb-23-2018 rmsd: ± 0.02
19
Pass 308 time Mar-22-2018 rmsd: ± 0.02
20
Pass 308 time Apr-18-2018 rmsd: ± 0.06
21
Pass 308 time May-15-2018 rmsd: ± 0.02
22
Pass 308 time Jun-11-2018 rmsd: ± 0.06
23
Pass 308 time Jul-08-2018 rmsd: ± 0.04
24
sea level anomaly m
Latitude
0.1
0
-0.1
-0.2
29.1
29.2
29.3
29.4
29.5
29.6
29.7
29.8

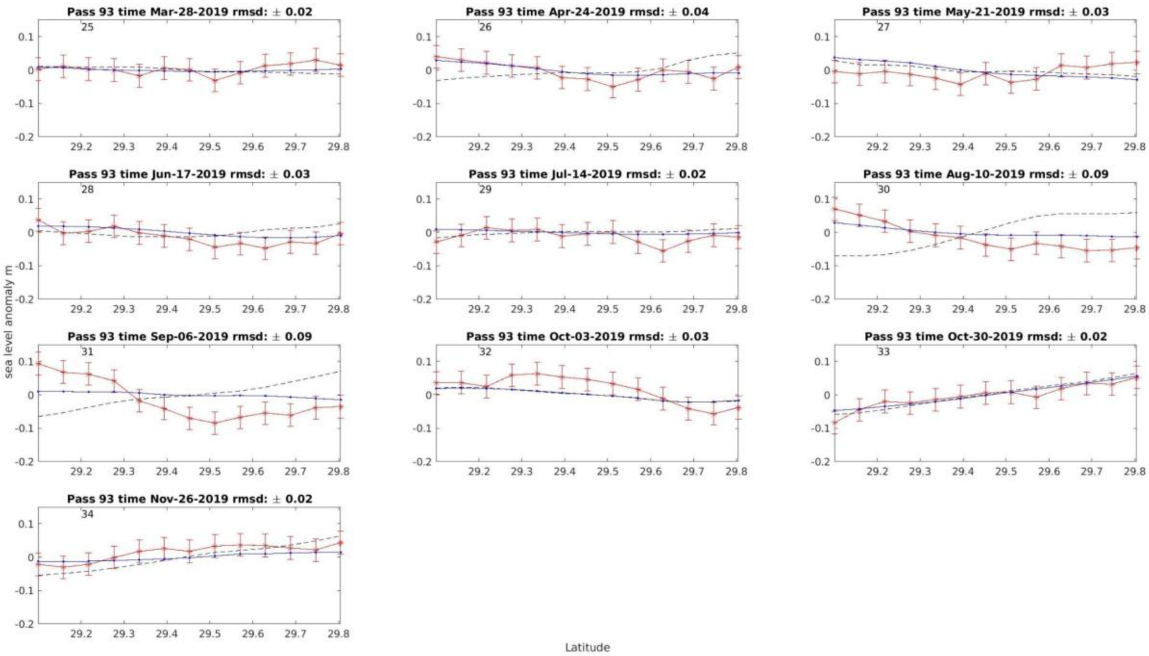
Pass 93 time Mar-28-2019 rmsd: ± 0.02
25
Pass 93 time Apr-24-2019 rmsd: ± 0.04
26
Pass 93 time May-21-2019 rmsd: ± 0.03
27
Pass 93 time Jun-17-2019 rmsd: ± 0.03
28
Pass 93 time Jul-14-2019 rmsd: ± 0.02
29
Pass 93 time Aug-10-2019 rmsd: ± 0.09
30
Pass 93 time Sep-06-2019 rmsd: ± 0.09
31
Pass 93 time Oct-03-2019 rmsd: ± 0.03
32
Pass 93 time Oct-30-2019 rmsd: ± 0.02
33
Pass 93 time Nov-26-2019 rmsd: ± 0.02
34
sea level anomaly m
0.1
0
-0.1
-0.2
29.2
29.3
29.4
29.5
29.6
29.7
29.8
Latitude

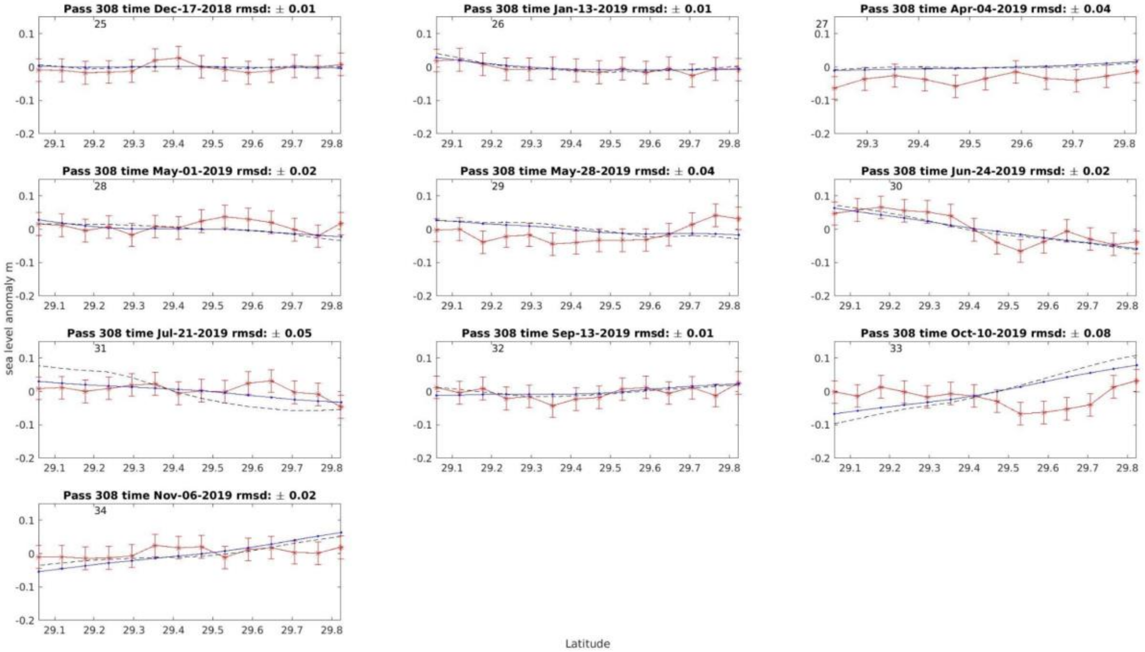
Pass 308 time Dec-17-2018 rmsd: ± 0.01
25
Pass 308 time Jan-13-2019 rmsd: ± 0.01
26
Pass 308 time Apr-04-2019 rmsd: ± 0.04
27
Pass 308 time May-01-2019 rmsd: ± 0.02
28
Pass 308 time May-28-2019 rmsd: ± 0.04
29
Pass 308 time Jun-24-2019 rmsd: ± 0.02
30
Pass 308 time Jul-21-2019 rmsd: ± 0.05
31
Pass 308 time Sep-13-2019 rmsd: ± 0.01
32
Pass 308 time Oct-10-2019 rmsd: ± 0.08
33
Pass 308 time Nov-06-2019 rmsd: ± 0.02
34
sea level anomaly m
0.1
0
-0.1
-0.2
29.1
29.2
29.3
29.4
29.5
29.6
29.7
29.8
Latitude

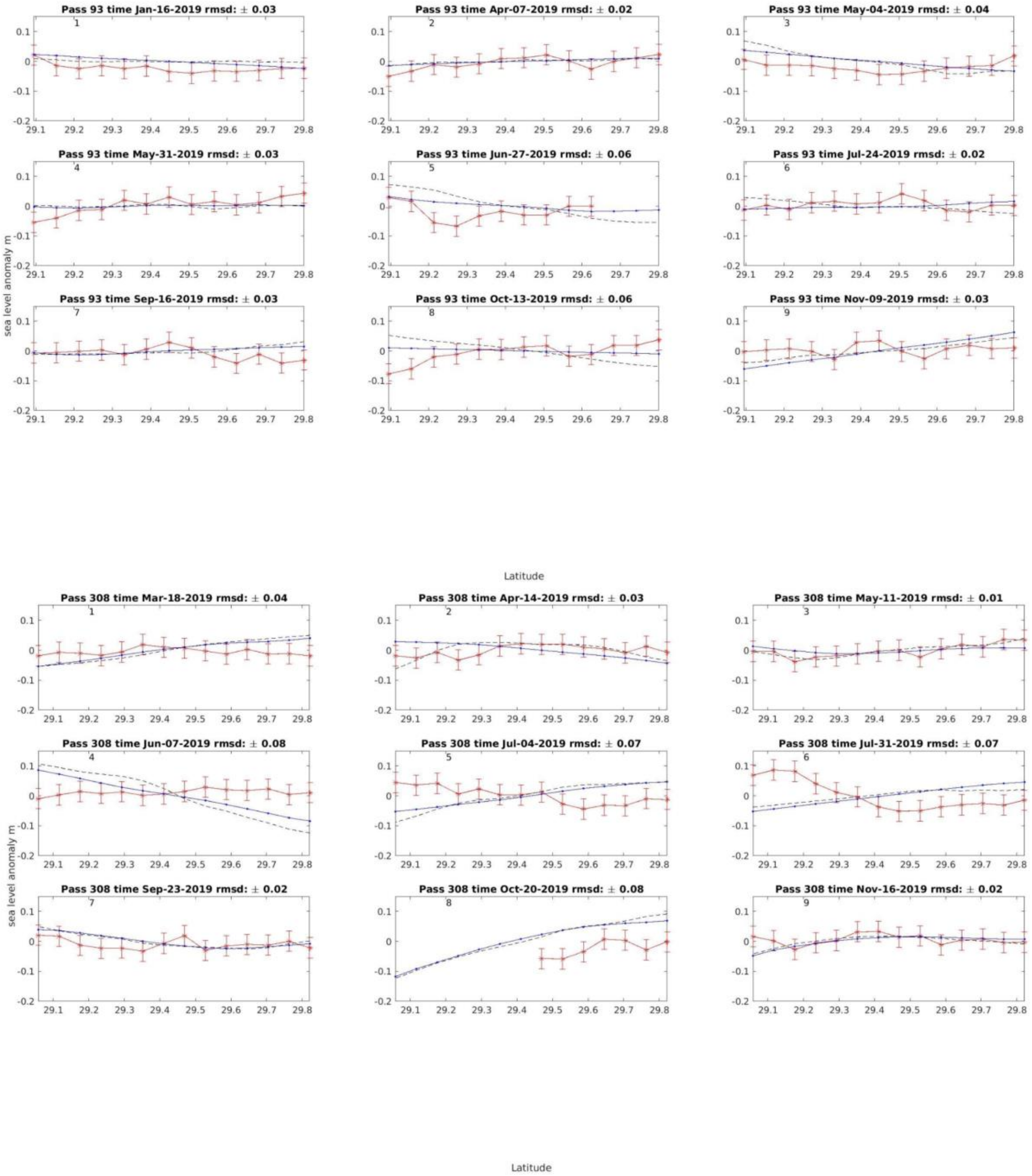

Figure C.5 *S3A and S3B SSHA (passes 93 and 308) (red solid line with error bars of 3.4 cm), HFR SSHA estimated using (geostrophic approximation (blue solid line with dots) and invariant form of the Reynold's averaged momentum equation applied to raw surface currents (blue dash line)), and root mean square difference between S3 and HFR radar SSHA(from raw surface currents) (rmsd).*

REFERENCES

Andersen, O. B., & Scharroo, R. (2011). *Range and geophysical corrections in coastal regions: And implications for mean sea surface determination* (S. Vignudelli, A. Kostianoy, P. Cipollini, & J. Benveniste, Eds.). Springer Berlin Heidelberg.

Ardhuin, F., Marié, L., Rascle, N., Forget, P., & Roland, A. (2009). Observation and estimation of lagrangian, stokes, and Eulerian currents induced by wind and waves at the sea surface. *Journal of Physical Oceanography*, *39*(11), 2820–2838. https://doi.org/10.1175/2009JPO4169.1

Aurin, D., Mannino, A., & Lary, D. J. (2018). Remote sensing of CDOM, CDOM spectral slope, and dissolved organic carbon in the global ocean. *Applied Sciences (Switzerland)*, *8*(12). https://doi.org/10.3390/app8122687

Bamford, H. A. (2013). Final programmatic environmental assessment for the Office of Coast Survey hydrographic survey projects. Program Planning and Integration, National Ocean Service, NOAA, U.S. Dept. of Commerce, Silver Spring. https://repository.library.noaa.gov/view/noaa/2679

Barrick, D. E., & Lipa, B. J. (1997). Evolution of Bearing Determination in HF Current Mapping Radars. *Oceanography*, (10), 72–75.

Bisnath, S., Wells, D., Santos, M., & Cove, K. (2004). *Initial Results from a Long Baseline , Kinematic , Differential GPS Carrier Phase Experiment in a Marine Environment*. 26–29.

Bjorkstedt, E., & Roughgarden, J. (2012). Larval Transport and Coastal Upwelling: An Application of HF Radar in Ecological Research. *Oceanography, 10*(2), 64–67. https://doi.org/10.5670/oceanog.1997.25

Björnsson, H., Venegas, S. a., Bjornsson, H., & Venegas, S. a. (1997). A Manual for EOF and SVD Analysis of Climatic Data. *CCGCR Report*, *97*(97), 52. https://doi.org/10.1002/elps.200700001

Bonnefond, P., Laurain, O., Exertier, P., Boy, F., Guinle, T., Picot, N., … Dinardo, S. (2018). Calibrating the SAR SSH of Sentinel-3A and CryoSat-2 over the Corsica facilities. *Remote Sensing*, 10(1), 1–14. https://doi.org/10.3390/rs10010092

Bowen, M. M., Emery, W. J., Wilkin, J. L., Tildesley, P. C., Barton, I. J., & Knewtson R., R. (2002). Extracting multiyear surface currents from sequential thermal imagery using the maximum cross-correlation technique. *Journal of Atmospheric and Oceanic Technology*, *19*(10), 1665–1676. https://doi.org/10.1175/1520-0426(2002)019<1665:EMSCFS>2.0.CO;2

Bretherton, C. (2002). Atm. Sci. 547 Boundary Layer Meteorology.

Cazenave, A., Cabanes, C., Dominh, K., & Mangiarotti, S. (2001). Recent sea level change in the Mediterranean sea revealed by Topex/Poseidon satellite altimetry. *Geophysical Research Letters*, *28*(8), 1607–1610. https://doi.org/10.1029/2000GL012628

Chapman, R D, Shay, L. K., Graber, H. C., Edson, J. B., Karachintsev, A., Trump, C. L., & Ross, D. B. (1997). *On the accuracy of HF radar surface current measurements : Intercomparisons with ship-based sensors (HF) radar systems can provide difficult to interpret since HF systems measure currents averaged over an area eggs . Ecologically , many pollutants , suc*. *102*.

Chapman, Rick D., & Graber, H. C. (1997). Validation of HF radar measurements. *Oceanography*, *10*(SPL.ISS. 2), 76–79. https://doi.org/10.5670/oceanog.1997.28

Chavanne, C. P., & Klein, P. (2010). Can oceanic submesoscale processes be observed with satellite altimetry? *Geophysical Research Letters*, *37*(22), 2–5. https://doi.org/10.1029/2010GL045057

Chelton, D. B., Ries, J. C., Haines, B. J., Fu, L. L., & Callahan, P. S. (2001). Chapter 1 Satellite Altimetry. *International Geophysics*, *69*(C), 1–183.

https://doi.org/10.1016/S0074-6142(01)80146-7

Cheng, K. (2005). Analysis of sea level measurements using GPS. PhD diss. The Ohio State University, Ohio. https://etd.ohiolink.edu/!etd.send_file?accession=osu1127151397&disposition=inline

Cho, K., Reid, R. O., & Nowlin, W. D. (1998). Objectively mapped stream function fields on the Texas-Louisiana shelf based on 32 months of moored current meter data. *Journal of Geophysical Research: Oceans*, *103*(C5), 10377–10390. https://doi.org/10.1029/98jc00099

Choi, K. (2007). Improvements in GPS Precision: 10Hz to One Day. PhD diss. University of Colorado.

Christensen, E. J., Haines, B. J., Keihm, S. J., Morris, C. S., Norman, R. A., Purcell, G. H., … Nerem, R. S. (1994). Calibration of TOPEX/POSEIDON at Platform Harvest. *Journal of Geophysical Research*, *99*(C12), 24465. https://doi.org/10.1029/94jc01641

Chuang, W., & Wiseman, W. J. J. (1983). Coastal sea level response to frontal passages on the Texas–Louisiana shelf. *Journal of Geophysical Research-Oceans*, *88*(2615–2620).

Church, J. A., & White, N. J. (2006). A 20th century acceleration in global sea level rise. *Geophysical Research Letters*, *33*(1), 94–97. https://doi.org/10.1029/2005GL024826

Cushman-Roisin, B., & Beckers, J.-M. (2012). *Introduction to Geophysical Fluid Dynamics: Physical and Numerical Aspects* (Second edi; R. Dmowska, D. Hartmann, & T. Rossby, Eds.). Academic Press.

Codiga, D. L. (2011). Unified tidal analysis and prediction using the UTide Matlab functions (p. 59). Narragansett, RI: Graduate School of Oceanography, University of Rhode Island.

Dilkoski, D.B., Richards, J.H. & Young, G.M. (1992). Results of the general adjustment of the North American Vertical Datum of 1988. *Surveying and Land Information Systems* 53:133–49.

Dodd, D., & Mills, J. (2012). Ellipsoidally referenced surveys - separation models. FIG Working Week 2012. International Federation of Surveyors, Rome, Italy.

Donoghue, J. F. (2011). Sea level history of the northern Gulf of Mexico coast and sea level rise scenarios for the near future. *Climatic Change*, *107*(1), 17–33. https://doi.org/10.1007/s10584-011-0077-x

Donohue, K., & Watts, D. R. (2016). Loop Current Eddy formation and baroclinic instability. *Dynamics of Atmospheres and Oceans*, *76*, 195–216. https://doi.org/10.1016/j.dynatmoce.2016.01.004

Drygas, H. (1983). SUFFICIENCY AND COMPLETENESS IN THE GENERAL GAUSS-MARKOV MODEL By. *The Indian Journal of Statistics, Series A (1961-2002)*, *45*(1), 88–98. https://doi.org/10.1177/0008068319570201

Dykstra, S. L., & Dzwonkowski, B. (2020). The Propagation of Fluvial Flood Waves Through a Backwater-Estuarine Environment. *Water Resources Research*, *56*(2), 1–24. https://doi.org/10.1029/2019WR025743

Dzwonkowski, B., Greer, A. T., Briseño-Avena, C., Krause, J. W., Soto, I. M., Hernandez, F. J., … Graham, W. M. (2017). Estuarine influence on biogeochemical properties of the Alabama shelf during the fall season. *Continental Shelf Research*, *140*(May), 96–109. https://doi.org/10.1016/j.csr.2017.05.001

Dzwonkowski, B., Kohut, J. T., & Yan, X. H. (2009). Seasonal differences in wind-driven across-shelf forcing and response relationships in the shelf surface layer of the central Mid-Atlantic Bight. *Journal of Geophysical Research: Oceans*, *114*(8), 1–15. https://doi.org/10.1029/2008JC004888.

Dzwonkowski, B, & Park, K. (2010). Influence of wind stress and discharge on the mean and seasonal currents on the Alabama shelf of the northeastern Gulf of Mexico. *Journal of Geophysical Research: Oceans*, *115*(12), 1–11. https://doi.org/10.1029/2010JC006449

Dzwonkowski, B, & Park, K. (2012). Subtidal circulation on the Alabama shelf during the Deepwater Horizon oil spill. *Journal of Geophysical Research: Oceans*, *117*(3), 1–15. https://doi.org/10.1029/2011JC007664

Dzwonkowski, B, Park, K., & Collini, R. (2015). Journal of Geophysical Research : Oceans. *Journal of Geophysical Research: Oceans*, *132*(11), 1–17. https://doi.org/10.1002/2014JC010320.Received

Dzwonkowski, B, Park, K., Lee, J., Webb, B. M., & Valle-Levinson, A. (2014). Spatial variability of flow over a river-influenced inner shelf in coastal Alabama during spring. *Continental Shelf Research*, *74*(January 2013), 25–34. https://doi.org/10.1016/j.csr.2013.12.005

Ekman, V. W. (1905). *On the influence of the earth's rotation on ocean-currents.* Retrieved from jscholarship.library.jhu.edu

Finnegan, C. R. (2009). *Mid-Shelf Current Characterization in the Mississippi Bight: A Statistical Analysis and Case Study*. The University of Southern Mississippi.

Gouillon, F., Morey, S. L., Dukhovskoy, D. S., & O'Brien, J. J. (2010). Forced tidal response in the Gulf of Mexico. *Journal of Geophysical Research: Oceans*, *115*(10), 1–16. https://doi.org/10.1029/2010JC006122

Greer, A. T., Shiller, A. M., Hofmann, E. E., Wiggert, J. D., Warner, S. J., Parra, S. M., … Society, T. O. (2018). Oceanography 31(3):90–103,. *Oceanography*, *31*(3), 91–103. https://doi.org/10.5670/oceanog.2018.302

Hayes, M. O. (1979). *Barrier island morphology as a function of tidal and wave regime:*

In Leatherman, S.P., ed., Barrier Islands: From the Gulf of St. Lawrence to the Gulf of Mexico. New York, Academic Press.

He, R., & Weisberg, R. H. (2003a). A loop current intrusion case study on the West Florida shelf. *Journal of Physical Oceanography*, *33*(2), 465–477. https://doi.org/10.1175/1520-0485(2003)033<0465:ALCICS>2.0.CO;2

He, R., & Weisberg, R. H. (2003b). West Florida shelf circulation and temperature budget for the 1998 fall transition. *Continental Shelf Research*, *23*(8), 777–800. https://doi.org/10.1016/S0278-4343(03)00028-1

Hess, K., Milbert, D., Gill, S. & Roman, D. (2003). Vertical datum transformation for kinematic-GPS hydrographic surveying. In Proceedings of the US Hydro 2003 Conference, Biloxi, Mississippi, USA (pp. 24-27).

Hocker, B., & Wardwell, N. (2010). Tidal datum determination and VDatum evaluation with a GNSS Buoy. In Proceedings of the 23rd International Technical Meeting of The Satellite Division of the Institute of Navigation (ION GNSS 2010) (pp. 2076-2086).

Hode, L. (2019). *Establishing the role of the Mississippi-Alabama barrier islands in Mississippi Sound and Bight circulation using observational data analysis and a coastal model*. The University of Southern Mississippi.

Huh, O. K., Wiseman, W. J., & Rouse, L. J. (1981). Intrusion of loop current waters onto the West Florida continental shelf. *Journal of Geophysical Research*, *86*(C5), 4186. https://doi.org/10.1029/jc086ic05p04186

IHO STANDARDS FOR HYDROGRAPHIC SURVEYS (S-44) 5th Edition February 2008.

Jankowski, K., Törnqvist, T., & Fernandes, A. (2017). Vulnerability of Louisiana’s coastal wetlands to present-day rates of relative sea level rise. Nat Commun 8, 14792 (2017). https://doi.org/10.1038/ncomms14792

Jochens, A. E., & Nowlin, W. D. J. (1998). *Northeastern Gulf of Mexico Chemical Oceanography and Hydrography Study: Year 2 - Annual Report*. U.S . Dept. of the Interior, Minerals Management Service, Gulf ofMexico OCS Region, New Orleans, LA. 123 pp.

Johan, S. L. (2014). *Local Sea Level Observations Using Reflected GNSS Signals*. CHALMERS UNIVERSITY OF TECHNOLOGY.

Johnson, D. R. (2008). *Ocean Surface Current Climatology in the Northern Gulf of Mexico, Ocean Springs, Mississippi*.

Kelly, K. A., & Strub, P. T. (1992). Comparison of velocity estimates from advanced very high resolution radiometer in the coastal transition zone. *Journal of Geophysical Research: Oceans*, *97*(C6), 9653–9668. https://doi.org/10.1029/92JC00734

Kim, S. Y. (2010). Observations of submesoscale eddies using high-frequency radar-derived kinematic and dynamic quantities. *Continental Shelf Research*, *30*(15), 1639–1655. https://doi.org/10.1016/j.csr.2010.06.011

Kundu, P. K. (1976). Ekman veering observed near the ocean bottom. *J. of Phys Oceanography*, *6*(2), 238–242.

Large, W. G., & Pond, S. (1981). Open Ocean Momentum Flux Measurements in Moderate to Strong Winds. *Physical Oceanography*, *11*, 324–336.

Larson, K. M., Ray, R. D., Nievinski, F. G., & Freymueller, J. T. (2013). The accidental tide gauge: A GPS reflection case study from kachemak bay, Alaska. *IEEE Geoscience and Remote Sensing Letters*, *10*(5), 1200–1204. https://doi.org/10.1109/LGRS.2012.2236075

Leben, R. R., Born, G. H., & Engebreth, B. R. (2002). Operational altimeter data processing for mesoscale monitoring. *Marine Geodesy*, *25*, 3–18. https://doi.org/10.1080/014904102753516697

Leben, Robert R. (2005). Altimeter-Derived Loop Current Metrics. *Geophysical Monograph-American Geophysical Union*, *161*, 181–202.

Lentz, S. J., & Fewings, M. R. (2012). The Wind- and Wave-Driven Inner-Shelf Circulation. *Annual Review of Marine Science*, *4*(1), 317–343. https://doi.org/10.1146/annurev-marine-120709-142745

Li, J., & Clarke, A. J. (2005). Interannual flow along the northern coast of the Gulf of Mexico. *Journal of Geophysical Research: Oceans*, *110*(11), 1–11. https://doi.org/10.1029/2004JC002606

Liu, Y., & Weisberg, R. H. (2007). Ocean Currents and Sea Surface Heights Estimated across the West Florida Shelf. *Journal of Physical Oceanography*, *37*(6), 1697–1713. https://doi.org/10.1175/jpo3083.1

Liu, Y., Weisberg, R. H., Merz, C. R., Lichtenwalner, S., & Kirkpatrick, G. J. (2010). HF radar performance in a low-energy environment: CODAR seasonde experience on the West Florida shelf. *Journal of Atmospheric and Oceanic Technology*, 27(10), 1689–1710. https://doi.org/10.1175/2010JTECHO720.1

Liu, Y., Weisberg, R. H., Vignudelli, S., Roblou, L., & Merz, C. R. (2012). Comparison of the X-TRACK altimetry estimated currents with moored ADCP and HF radar observations on the West Florida Shelf. *Advances in Space Research*, 50(8), 1085–1098. https://doi.org/10.1016/j.asr.2011.09.012

Liu, Y., & Weisberg, R. H. (2005). Momentum balance diagnoses for the West Florida Shelf. *Continental Shelf Research*, *25*(17), 2054–2074. https://doi.org/10.1016/j.csr.2005.03.004

Liu, Y., Weisberg, R. H., Vignudelli, S., & Mitchum, G. T. (2016). Journal of Geophysical Research : Oceans. *Journal of Geophysical Research: Oceans*, *121*(9), 6762–6778. https://doi.org/10.1002/2016JC012132.Received

Madec, G., Delecluse, P., Imbard, M., & Levy, C. (1998). *Institut Pierre Simon Laplace Ocean General Circulation Model Reference Manual*.

Malys, S., R. Wong, and S. A. True. (2016). The WGS 84 Terrestrial Reference Frame in 2016. National Geospatial Intelligence Agency. Presented at ICG-11, Sochi Russia.

Maul, G. (1977). The annual cycle of the Gulf Loop Current, Part 1 : observations during a one-year time series. *Journal of Marine Research*, *35*(1), 29–47.

Menéndez, M., & Woodworth, P. L. (2010). Changes in extreme high water levels based on a quasi-global tide-gauge data set. *Journal of Geophysical Research: Oceans*, *115*(10), 1–15. https://doi.org/10.1029/2009JC005997

Mertz, F., Rosmorduc, V., Maheu, C., & Faugere, Y. (2017). For Sea Level SLA products. *Copernicus Marine Service*, (1.1), 1–51. Retrieved from https://resources.marine.copernicus.eu/documents/PUM/CMEMS-SL-PUM-008-032-062.pdf

Mitchum, G. T., & Clarke, A. J. (1986). The frictional nearshore response to forcing by synoptic scale winds. *Journal of the Physical Oceanography*, *16*, 934–946.

Modjeld, H. O., & Lavelle, J. W. (1984). Setting the Length Scale in a Second-Order Closure Model of the Unstratified Bottom Boundary Layer. *Journal of Physical Oceanography*, *14*, 833–839.

Morey, S. L., Martin, P. J., O'Brien, J. J., & Wallcraft, A. A. (2003a). Export pathways for river discharged fresh water in the northern Gulf of Mexico. *Journal of Geophysical Research*, *108*(C10), 3303. https://doi.org/10.1029/2002JC001674

Morey, S. L., & O'Brien, J. J. (2002). The spring transition from horizontal to vertical thermal stratification on a midlatitude continental shelf. *Journal of Geophysical*

Research: Oceans, *107*(C8), 12–1.

Morey, S. L., Schroeder, W. W., O’Brien, J. J., & Zavala-Hidalgo, J. (2003b). The annual cycle of riverine influence in the eastern Gulf of Mexico basin. *Geophysical Research Letters*, *30*(16), 1–4. https://doi.org/10.1029/2003GL017348

Moritz, H. (1988). Geodetic Reference System (1980). The International Union of Geodesy and Geophysics. The Geodesist Handbook 62: 348-58

NOAA CO-OPS, (2000). Tidal Datums and Their Applications, NOAA Special Publication CO-OPS 1, National Ocean Service, NOAA, U.S. Dept. of Commerce, Silver Spring.

NOAA CO-OPS, (2003). Computational Techniques for Tidal Datums Handbook, NOAA Special Publication NOS CO-OPS 2, Center for Operational Oceanographic Products and Services, National Ocean Service, NOAA, U.S. Dept. of Commerce, Silver Spring.

NOAA NOS, (2020). Hydrographic Surveys Specifications and Deliverables, National Ocean Service, NOAA, U.S. Dept. of Commerce, Silver Spring.

Nowlin, W. D., Jochens, A. E., Dimarco, S. F., Reid, R. O., & Howard, M. K. (2005). Low-frequency circulation over the Texas-Louisiana continental shelf. *Geophysical Monograph Series*, *161*(January), 219–240. https://doi.org/10.1029/161GM17

Nwankwo, U., Howden, S., Wells, D., Barbor, K., & Dave, D. (2017a). Ellipsoidal Referenced Tidal Datum at an Offshore Buoy in the Mississippi Bight Using PPK and PPP GPS Processing and Tidal Datum Transfer. *U.S. Hydrographic Conference 2017*. Galveston.

Nwankwo, U. C., Howden, S. D., Dodd, D., & Wells, D. E. (2017b). Assessment of the Sea levels and Currents at the Mississippi Bight During Hurricane Katrina. AGUFM. OS23B-1388. https://agu.confex.com/agu/fm17/mediafile/Handout/Paper224725/Uchenna_Nwank wo.pdf

Nwankwo, U. C., Howden, S., & Wells, D. (2019). Further Investigations of VDatum to NAD83 Vertical Separations Using United States Geological Service (USGS) Coastal Sea levels Gage and Hydrolevel Buoy. *U.S. Hydrographic Conference*, 1–12. Biloxi.

Nwankwo, U., Howden, S., Connon, B., Nechaev, D. and Wells, D. (2020a). The Importance of Data in Analyzing the Response of the Circulation and Sea Level on Continental Shelf from Louisiana to Alabama to Hurricane Nate and Tropical Storm Alberto. In Proceedings of the Canadian Hydro 2020 Conference, Quebec City, Quebec, Canada. https://hydrography.ca/wp-content/uploads/2020/04/23_Nwankwo_CHC_2020_Conference.pdf

Nwankwo, U. C., Howden, S., Wells, D., & Connon, B. (2021). Validation of VDatum in Southeastern Louisiana and Western Coastal Mississippi. *Marine Geodesy*, *44*(1), 1-25. https://doi.org/10.1080/01490419.2020.1846644

Oey, L., Ezer, T., & Lee, H. (2005). Loop Current, rings and related circulation in the Gulf of Mexico: A review of numerical …. *Geophysical Monograph-American …*, *161*, 31–56. Retrieved from http://scholar.google.com/scholar?cites=6420488778323234 20&hl=en#46

Oey, L. Y., & Zhang, H. C. (2004). A mechanism for the generation of subsurface cyclones and jets. *Cont. Shelf Res.*, *24*, 2109–2131.

Ohlmann, J. C., & Niiler, P. P. (2005). Circulation over the continental shelf in the northern Gulf of Mexico. *Progress in Oceanography*, *64*(1), 45–81. https://doi.org/10.1016/j.pocean.2005.02.001

Ohlmann, J. C., Niiler, P. P., Fox, C. A., & Leben, R. R. (2001). Eddy energy and shelf interactions in the Gulf of Mexico. *Journal of Geophysical Research: Oceans*, *106*(C2), 2605–2620. https://doi.org/10.1029/1999jc000162

Oyarzún, D., & Brierley, C. M. (2019). The future of coastal upwelling in the Humboldt current from model projections. *Climate Dynamics*, *52*(1–2), 599–615. https://doi.org/10.1007/s00382-018-4158-7

Parker, B. (2002). The integration of bathymetry, topography, and shoreline, and the vertical datum transformations behind it. *International Hydrographic Review*

Parker, B., Milbert, D., Hess, K., and Gill, S. (2003). National VDATUM – The Implementation of a national vertical datum transformation database. *International Hydrographic Review*.

Pereira, M. B., & Berre, L. (2006). The use of an ensemble approach to study the background error covariances in a global NWP model. *Monthly Weather Review*, *134*(9), 2466–2489. https://doi.org/10.1175/MWR3189.1

Prandle, D. (2012). Tidal and Wind-Driven Currents From OSCR. *Oceanography*, *10*(2), 57–59. https://doi.org/10.5670/oceanog.1997.23

Pugh, D., & Philip, W. (2014). *Sea level Science Understanding Tides, Surges, Tsunamis and Mean Sea level Changes*. https://doi.org/https://doi.org/10.1017/CBO9781139235778

Reid, R. O., & Whitaker, R. E. (1981). *Numerical model for astronomical tides in the Gulf of Mexico*. pp. 115, Texas A&M Univ. Report for U. S. Army Engineers Waterway Experiment Station, College Station, Tex.

Quartly, G. D., Srokosz, M. A., & Guymer, T. H. (1998). Understanding the effects of rain on radar altimeter waveforms. *Advances in Space Research*, *22*(11), 1567–1570. https://doi.org/10.1016/S0273-1177(99)00072-1

Roesler, C. J., Emery, W. J., & Kim, S. Y. (2013). *Evaluating the use of high-frequency radar coastal currents to correct satellite altimetry*. *118*(August 2012), 3240–3259. https://doi.org/10.1002/jgrc.20220

Rudnick, D. L., Gopalakrishnan, G., & Cornuelle, B. D. (2014). Cyclonic Eddies in the Gulf of Mexico: Observations by Underwater Gliders and Simulations by Numerical Model. *Journal of Physical Oceanography*, *45*(1), 313–326. https://doi.org/10.1175/jpo-d-14-0138.1

Sauer, V. B., & Turnipseed, D. P. (2010). Stage measurement at gaging stations (p. 45). US Department of the Interior, US Geological Survey.

Schaeffer, A., Gramoulle, A., Roughan, M., & Mantovanelli. (2017). Journal of Geophysical Research : Oceans. *Journal of Geophysical Research: Oceans*, *122*, 1–22. https://doi.org/10.1002/2016JC012264.Received

Schmitz, W. J., Biggs, D. C., Lugo-Fernandez, A., Oey, L. Y., & Sturges, W. (2005). *A Synopsis of the Circulation in the Gulf of Mexico and on its Continental Margins* (A. Lugo-Fernandez & W. Sturges, Eds.). https://doi.org/10.1029/161GM03

Schwarz, C.R. (1990). North American Datum of 1983. NOAA professional paper, NOS 2, *National Geodetic Survey*.

Shay, L. (2012). Internal Wave-Driven Surface Currents From HF Radar. *Oceanography, 10*(2), 60–63. https://doi.org/10.5670/oceanog.1997.24

Shinkle, R. K. & Dokka, K. D. (2004). Rates of vertical displacement at benchmarks in the lower Mississippi Valley and the northern Gulf Coast: NOAA Technical Report, 50. Pp 135.

Smith, R. W. (1987). Department of Defense World Geodetic System 1984: its definition and relationships with local geodetic systems. Defense Mapping Agency.

Stewart, R. H., & Joy, J. W. (1974). HF Radar Measurement of Surface Current. *Deep-Sea Research*, (21), 1039–1049.

Stigebbrandt, A. (1985). A Model for the Seasonal Pycnocline in Rotating Systems with Application to the Baltic Proper. *Journal of Physical Oceanography*, *15*, 1392–

1404.

Strauss, B. H., Ziemlinski, R., Weiss, J. L., & T. J. Overpeck. (2012). Tidally adjusted estimates of topographic vulnerability to sea level rise and flooding for the contiguous United States. *Environmental research letters*, 7: 1-122. doi:10.1088/1748-9326/7/1/014033

Sturges, W., & Evans, J. C. (1983). on the Variability of the Loop Current in the Gulf of Mexico. *Journal of Marine Research*, *41*(4), 639–653. https://doi.org/10.1357/002224083788520487

Sturges, W., & Leben, R. (2002). Frequency of Ring Separations from the Loop Current in the Gulf of Mexico: A Revised Estimate. *Journal of Physical Oceanography*, *30*(7), 1814–1819. https://doi.org/10.1175/1520-0485(2000)030<1814:forsft>2.0.co;2

Swanson, R. L. (1974). NOAA Technical Report NOS 64, Variability of Tidal Datums and Accuracy in Determining Datums from Short Series of Observations US Department of Commerce, NOAA, NOS, Rockville.

The Receiver Independent Exchange Format (RINEX) v 3.03. (2015). International GNSS Service (IGS), RINEX Working Group and Radio Technical Commission for Maritime Services Special Committee 104 (RTCM-SC104).

Teague, C. C., Vesecky, J. F., & Fernandez, D. M. (1997). HF RADAR INSTRUMENTS, PAST TO PRESENT. *Oceanography*, (10), 40–44.

Tournadre, J., Chapron, B., Reul, N., & Vandemark, D. C. (2006). A satellite altimeter model for ocean slick detection. *Journal of Geophysical Research: Oceans*, *111*(4). https://doi.org/10.1029/2005JC003109

Trimble NetRS^{TM} GPS Receiver User Guide. November (2004). Version 1.11, Revision A

Trimble NetR8 GNSS Reference Receiver. November (2008). Version 3.80, Revision A.

US Coast. (1965). Manual of Tide Observations (Vol. 30, No. 1). US Government Printing Office.

Walker, N. D., Pilley, C. T., Raghunathan, V. V., D'Sa, E. J., Leben, R., Hoffmann, N. G., … Turner, R. E. (2013). Impacts of Loop Current Frontal Cyclonic Eddies and Wind Forcing on the 2010 Gulf of Mexico Oil Spill. *Monitoring and Modeling the Deepwater Horizon Oil Spill: A Record Breaking Enterprise*, 103–116. https://doi.org/10.1029/2011GM001120

Wang, D.-P., Oey, L.-Y., Ezer, T., & Hamilton, P. (2003). Near-Surface Currents in DeSoto Canyon (1997–99): Comparison of Current Meters, Satellite Observation, and Model Simulation. *Journal of Physical Oceanography*, *33*(1), 313–326. https://doi.org/10.1175/1520-0485(2003)033<0313:nscidc>2.0.co;2

Waypoint Products Groups, (2016). A NovAtel Precise Positioning Product GrafNav/GrafNet 8.70 User manual v2 User Manual November 2016, NovAtel Inc.

Westerink, J.J., Luettich, R. A., & Scheffner, N. W. (1993). ADCIRC: An Advanced Three-Dimensional Circulation Model for Shelves, Coasts, and Estuaries, Report 3:Development of a Tidal Constituent Database for the Western North Atlantic and Gulf of Mexico, Technical Report DRP-92-6, U.S. ACE Waterways Experiment Station, Vicksburg, MS.

Weisberg, R., & He, R. (2003). Local and deep-ocean forcing contributions to anomalous water properties on the West Florida Shelf. *Journal of Geophysical Research*, *108*(C6). https://doi.org/10.1029/2002jc001407

Weisberg, Robert H., He, R., Liu, Y., & Virmani, J. I. (2005). West Florida shelf circulation on synoptic, seasonal, and interannual time scales. *Geophysical Monograph Series*, *161*, 325–347. https://doi.org/10.1029/161GM23

Woodworth, P. L., Melet, A., Marcos, M., Ray, R. D., Wöppelmann, G., Sasaki, Y. N.,

… Merrifield, M. A. (2019). Forcing Factors Affecting Sea Level Changes at the Coast. In *Surveys in Geophysics* (Vol. 40). https://doi.org/10.1007/s10712-019-09531-1

Yang, Z, Myers, E. P., & White, S. A. (2010). VDATUM for eastern Louisiana and Mississippi coastal waters: Tidal datums, marine grids, and sea surface topography. *NOAA Technical Memorandum NOS CS 19.*

Yankovsky, A. E. (2015). *The Cold-Water Pathway during an Upwelling Event on the New Jersey Shelf The Cold-Water Pathway during an Upwelling Event on the New Jersey Shelf*. *0485*(June). https://doi.org/10.1175/1520-0485(2003)033<1954

Yoshikawa, Y., Masuda, A., Marubayashi, K., Ishibashi, M., & Okuno, A. (2006). On the accuracy of HF radar measurement in the Tsushima Strait. *Journal of Geophysical Research: Oceans*, *111*(4), 2–11. https://doi.org/10.1029/2005JC003232

Yuley, C. O. (2013). *Copyright 2013 by James Marinchak*. Georgia Institute of Technology.

Zagar, N., Andersson, E., & Fisher, M. (2004). Based on a Study of Equatorial. *Weather*, (April).

Zavala-Hidalgo, J., Romero-Centeno, R., Mateos-Jasso, A., Morey, S. L., & Martínez-López, B. (2014). The response of the Gulf of Mexico to wind and heat flux forcing: What has been learned in recent years? *Atmosfera*, *27*(3), 317–334. https://doi.org/10.1016/S0187-6236(14)71119-1